

Thesis for the Degree of Doctor of Philosophy

Alloy Plasmonics
Fundamentals and Applications

Christopher Tiburski

Department of Physics
CHALMERS UNIVERSITY OF TECHNOLOGY
Göteborg, Sweden 2022

Alloy Plasmonics - Fundamentals and Applications

Christopher Tiburski

ISBN 978-91-7905-720-6

© Christopher Tiburski, 2022.

Doktorsavhandlingar vid Chalmers tekniska högskola

Ny serie nr 5186

ISSN 0346-718X

Department of Physics

Chalmers University of Technology

SE-412 96 Gothenburg

Sweden

Telephone + 46 (0)31-772 1000

Cover: Artistically modified and colored electron microscope images of metal nanoparticles to represent different alloys with different optical properties.

Printed at Chalmers Digitaltryck

Göteborg, Sweden 2022

Abstract

Alloys have for a long time been important in the development of our society; from the bronze age, where man learned how to alloy copper with tin, to today, where many products are made of steel and aluminum alloys. Similarly, but maybe not as generally well known, alloys have lately been proposed as a new paradigm in nanophotonics, to tailor optical properties of nanomaterials that find applications within telecommunication, sensing, or biotechnology. Furthermore, alloys are explored in heterogeneous catalysis to develop solutions to increase activity and selectivity of chemical processes. Nanophotonics and catalysis, separately and in combination, are the focus of this thesis. Specifically, we have compiled a library of alloy complex dielectric functions for the late transition metals by utilizing time-dependent density-functional theory. The calculated dielectric functions were benchmarked by (i) nanofabricating series of alloy nanoparticle arrays with systematically varying composition, (ii) measuring their plasmonic properties, and (iii) comparing these properties with electrodynamic simulations of alloy nanoparticles, using the dielectric function library as the input. These dielectric functions allowed us further to screen the absorption efficiency of nanoparticles of multiple combination of size and composition to show the superior performance of alloys compared to their neat constituents.

The second theme in this thesis is plasmon-enhanced catalysis. In this field there is a continuous discussion regarding the reaction enhancing mechanisms when noble metal catalyst nanoparticles are irradiated with visible light during a catalytic reaction. Here we investigated the role of photothermal enhancement of reactions by tailoring the catalytic activity of nanofabricated particles without radiation by means of alloying Pd with Au, while keeping the optical absorption cross section constant, as confirmed by electrodynamic simulations using our dielectric function library as the input. Temperature is a crucial parameter during catalysis in general and photocatalysis in specifically. However, it is intrinsically difficult to measure the temperature of nanoparticles with traditional methods. Therefore, we presented a hydrogen nanothermometry method that allows measuring nanoparticle temperature directly and noninvasively via the temperature dependent phase transition during Pd-hydride formation. We showed that the Pd particle temperature during light-induced heating can be measured with a resolution of 1 °C.

Keywords: nanoalloys, plasmonics, sensing, heterogeneous catalysis, dielectric function, photothermal, nanothermometry, CO oxidation, palladium-hydride, gold-palladium

*När lyktorna tänds*¹

List of appended papers

This thesis is based on the work presented in the following papers:

Paper I

A Library of Late Transition Metal Alloy Dielectric Functions for Nanophotonic Applications

J. M. Rahm*, C. Tiburski*, T. P. Rossi, F. A. A. Nugroho, S. Nilsson, C. Langhammer, P. Erhart.

Advanced Functional Materials **30 (35)**, 2002122 (2020).

* equal contribution

Paper II

Light-Off in Plasmon-Mediated Photocatalysis

C. Tiburski, A. Boje, S. Nilsson, Z. Say, J. Fritzsche, H. Ström, A. Hellman, C. Langhammer

ACS Nano **15 (7)**, 11535-11542 (2021)

Paper III

Optical Hydrogen Nanothermometry of Plasmonic Nanoparticles under Illumination

C. Tiburski, F. A. A. Nugroho, C. Langhammer

ACS Nano **16 (4)**, 6233-6243 (2022)

Paper IV

Engineering Optical Absorption in Late Transition Metal Nanoparticles by Alloying

C. Tiburski, C. Langhammer

Submitted manuscript

Paper V

A Microshutter for the Nanofabrication of Plasmonic Metal Alloys with Single Nanoparticle Composition Control

C. Andersson*, O. Serebrennikova*, C. Tiburski*, S. Alekseeva, J. Fritzsche, C. Langhammer

In manuscript

* equal contribution

My contribution to appended papers

Paper I: I fabricated the samples, performed the FDTD simulations, SEM, XPS, and optical extinction measurements with related analysis, and wrote the experimental part of the manuscript.

Paper II: I fabricated the samples, performed the FDTD simulations, SEM, XPS, and optical extinction measurements with related analysis, and wrote the first draft of the manuscript, except the “First-Principles Informed Microkinetic Modeling” part.

Paper III: I fabricated the samples, performed the FDTD and heat distribution simulations, performed all measurements with related analysis, and wrote the first draft of the manuscript.

Paper IV: I fabricated the samples, performed the FDTD simulations, SEM, and optical absorption measurements with related analysis, and wrote the first draft of the manuscript.

Paper V: I performed the SEM-EDS measurements, the FDTD simulations and the related analysis, and participated in the writing of the manuscript.

Related publication not included in the thesis

I. Catalytically Active and Thermally Stable Core–Shell Gold–Silica Nanorods for CO Oxidation

Y. Chen, S. Lerch, Z. Say, C. Tiburski, C. Langhammer, K. Moth-Poulsen
RSC Advances **11(19)**, 11642-11650 (2021).

II. Copper Catalysis at Operando Conditions — Bridging the Gap between Single Nanoparticle Probing and Catalyst-Bed-Averaging

D. Albinsson, A. Boje, S. Nilsson, C. Tiburski, A. Hellman, H. Ström, C. Langhammer
Nature Communications **11(1)**, 1-13 (2020).

III. Nanoplasmonic NO₂ Sensor with a Sub-10 Parts per Billion Limit of Detection in Urban Air

I. Tanyeli, I. Darmadi, M. Sech, C. Tiburski, J. Fritzsche, O. Andersson, C. Langhammer
ACS Sensors **7(4)**, 1008-1018 (2022).

IV. Plasma Cleaning of Surfactants on Pd Nanoparticle and its Implication for Hydrogen Sorption Kinetics

I. Darmadi, J. Piella, A. Stolaś, C. Tiburski, K. Moth-Poulsen, C. Langhammer
In manuscript

Contents

1	Introduction	1
1.1	Scope of this Thesis	3
2	Alloys	5
2.1	Phase Diagrams	5
2.2	Segregation	9
3	Palladium-Hydrides	11
3.1	Hydride Formation	11
3.2	Temperature Sensing using Palladium-Hydride	14
4	Dielectric Functions and Plasmonics	19
4.1	Free Electron Gas Model	19
4.2	Localized Surface Plasmon Resonance	22
4.3	Finite Difference Time Domain Electrodynamic Simulations	24
4.4	Dielectric Function of Selected Transition Metals and their Alloys . .	27
4.5	LSPR Sensing	36
5	Catalysis	39
5.1	Heterogeneous Catalysis	39
5.2	Plasmon Mediated Catalysis	42
5.3	CO Oxidation	46
6	Nanofabrication	51
6.1	Hole-Mask Colloidal Lithography	51
6.2	Material Deposition	53
6.3	Annealing	56

7	Setup/Characterization	59
7.1	Catalytic Flow Reactor Measurement Setup	59
7.2	X-ray Photoelectron Spectroscopy	61
7.3	Scanning Electron Microscopy	69
7.4	Energy-Dispersive X-Ray Spectroscopy	71
8	Summary and Outlook	75
8.1	Summary of the Appended Papers	75
8.2	Outlook	78
	Acknowledgement	81
	Bibliography	83

1 Introduction

The overarching topic of my thesis is late transition metal alloys in the context of plasmonics. Alloys are the combination of two or more components, where at least one is a metal, intermixed at the atomic level, that are produced with the goal to improve mechanical,^{2,3} electrical,⁴ thermal,⁵ or chemical properties.⁶ Historically, alloys have been used by mankind in the form of meteoric iron even before people knew the concept of an alloy.⁷ The most prominent example from history when alloys were deliberately created is probably the Bronze Age, where man started to alloy copper with tin, which provided tools with increased hardness, stiffness, or ductility, depending on the composition. Also today, we find alloys in almost every metal object. The most obvious example is probably steel, where the properties of iron are modified by mixing it with carbon.⁸ However, not only carbon is added to iron nowadays as the properties of steel are tailored further to our specific needs by, for example, mixing it with chromium to improve toughness, with manganese to increase wear resistance, or with titanium to improve corrosion resistance.⁹

Although alloying is an ancient technology, the concept of alloying is explored also in younger areas of science and technology, like in the field of nanophotonics and plasmonics.¹⁰ Plasmonics is, in short, the field of investigating the interaction of light with metal thin films and nanostructures.¹⁰ In the field of plasmonics, alloying has recently been proposed as a means to tailor optical properties of nanomaterials to achieve functionality and properties that are not accessible when using the pure elements - conceptually very similar as when making steel. However, the use of alloys in nanophotonic applications is still in its infancy, mostly limited to few alloy systems, and has only recently gained larger interest.¹⁰⁻¹⁴ This is mainly due to a lack of understanding of the fundamental optical properties of alloys in general, and a lack of complex dielectric functions of alloys that cover a wide spectral and compositional

1 Introduction

range. Dielectric functions are critical since projected onto nanophotonics, they are needed to predict the response of nanostructures to light by means of modeling or electrodynamic simulations. Such predictions, in turn, are important to both rationally design and fine-tune alloy nanostructures for their intended applications, such as waveguides, gratings or plasmonic nanoantennas.^{15–17}

The word nanophotonics gives the small but distinct hint that we are in the world of nanometer sized objects. In numbers, a nanometer corresponds to 1×10^{-9} m, which means a billionth of a meter. In other words, one nanometer compares to a meter like a euro coin to the size of our planet. To give another example, one nanometer is such a short distance that our fingernails grow on average every second around 1.3 nm.¹⁸ Nevertheless, structures in this size range are nowadays used in most electronic devices, for example as the components on microchips, such as transistors.¹⁹ However, not only in microelectronics but also in the chemical industry materials structured at the nanometer scale are widely applied. One example are catalysts, which play a key role in the quest to increase the yield and reduce the environmental impact of chemical processes. To highlight the importance of catalysts, we can note that ca. 90 % of the chemical industry uses a catalytic reaction somewhere along its value chain.²⁰

An interesting concept related to alloying is to use light and its interaction with solid state nanomaterials to increase catalyst activity or steer selectivity. This area of technology is commonly referred to as photocatalysis.²¹ In recent years, a sub-area of photocatalysis has developed rapidly, which proposes the use of localized surface plasmon resonances (LSPR) to enhance the cross section of photocatalytic reactions on metal nanoparticles.^{22–24} LSPRs are resonant collective free electron oscillations in metal nanoparticles excited by visible light. This branch of nanoscience at the interface between nanophotonics and heterogeneous catalysis is commonly referred to as plasmon-mediated catalysis.²⁵ Despite its rapid development with sometimes spectacular reports about rate and selectivity enhancements of plasmonic catalysts,^{26–28} there is an ongoing vivid discussion about the mechanistic origin of the observed effects, and in particular the distinction between photothermal and hot-carrier mediated reaction enhancement mechanisms.^{29–37} One of the key problems that makes it difficult to untangle these mechanisms is the fact that the actual temperature of the catalyst nanoparticles localized in an – often three-dimensional – catalyst bed is ex-

perimentally very difficult to determine accurately. Precise control of the temperature is essential as the catalytic rate scales exponentially with temperature. Conventional temperature measurements, like a thermocouple, are, however, not working properly at the small scales of nanoparticles and it is, for example, challenging to ensure good thermal contact between the temperature probe and the sample, or to take the big mismatch in thermal mass between particle(s) and probe into account. Due to these challenges, the search for the correct reaction enhancement mechanism in plasmon enhanced catalysis developed into a “holy grail” of the field.

1.1 Scope of this Thesis

In this thesis, I have investigated the use of alloy nanoparticles in the context of plasmonics to tackle some of the challenges mentioned above.

In **Paper I**, we responded to the lack of a complete and consistent set of dielectric functions for plasmonic materials and compiled a library of alloy dielectric functions for ten binary alloys based on the late transition metals gold (Au), silver (Ag), copper (Cu), palladium (Pd), and platinum (Pt), using time-dependent density-functional theory. A selection of these dielectric functions was benchmarked in experiments based on nanofabricated alloy nanoparticle arrays by measuring their plasmonic properties and comparing them with corresponding finite-difference time-domain simulations where we used the dielectric functions as input. A good agreement between experiments and simulations was obtained, which corroborates the physical relevance of the compiled alloy dielectric function library. Once established and experimentally benchmarked, these dielectric functions allowed us to investigate and screen the impact of alloying on the light absorption properties of late transition metal nanoparticles across a wide range of sizes, again using electromagnetic simulations in combination with experiments (**Paper IV**). Specifically, we first compared a selection of simulations for three alloy systems (AuPd, PdPt, AuCu) with experimentally measured optical absorption efficiencies and thereafter screened the full set of ten binary alloys of the late transition metals Au, Ag, Cu, Pd, and Pt. As the key result, we found that numerous alloys systems outperform their neat constituents in terms of light absorption efficiency, which advocates alloying as an interesting handle to tailor

1 Introduction

light absorption properties of metallic nanomaterials. Inspired by these results, we then set out to simplify the process of alloy particle nanofabrication and enabled its control down to the level of single nanoparticles in terms of composition and size by introducing a microshutter device in **Paper V**. The microshutter allows for precise fabrication of alloy nanoparticles with different and accurately controlled compositions next to each other in an array, as we verified by energy-dispersive X-ray spectroscopy and optical dark field scattering measurements of the single particles. As we also showed, this nanofabrication method allows for efficient experimental screening of alloy compositions in a single experiment, for example with respect to their hydrogen sorption properties, as exemplified on the AuPd alloy system, which is widely used as transducer material in plasmonic hydrogen sensors.

In **Paper II**, we studied photothermal effects that arise upon noble metal catalyst nanoparticle irradiation with visible light during a catalytic reaction. Specifically, we applied the concept of alloying by mixing Pd with Au in arrays of nanofabricated catalyst particles, to tailor the catalytic activity of a nanofabricated model catalyst in the absence of radiation, while, at the same time, maintaining a constant optical cross section upon illumination. This way, we could unambiguously show that the catalytic activity is not governed by the photon flux alone but also depends strongly on the temperature of the catalyst in the absence of illumination. As discussed in the introduction and shown explicitly in **Paper II**, the nanoparticle temperature is indeed a very important parameter one needs to accurately understand and control to be able to distinguish electronic and thermal effects during photocatalysis. To this end, the importance of accurate nanoscale temperature measurements and control is not limited to catalysis but also important in nanooptics, biology and nanosensors. Therefore, we developed in **Paper III** a non-invasive and direct way to measure nanoparticle temperature via the first-order phase transformation of Pd to Pd-hydride upon hydrogen absorption. Specifically, we demonstrated a direct and absolute temperature measurement of Pd nanoparticles with a resolution of 1 °C during light-absorption induced heating.

2 Alloys

Alloys are the combination of two or more components, intermixed at the atomic level, where at least one is a metal.³⁸ Alloys are widely used in different technologies to alter material properties, such as increasing strength and hardness.³⁹ They are furthermore explored in heterogeneous catalysis to optimize activity and selectivity, and predicted to find application in plasmon-mediated catalysis, as a means to tailor the light harvesting capabilities of metal nanoparticles.^{40–42} Overall, alloys provide ample opportunity to tailor functional material properties to achieve functions not obtainable by the constituent materials alone. This versatility is one of the reasons why alloys are the common ground of most of my work presented in this thesis.

2.1 Phase Diagrams

When designing alloys, the phase diagram for the constituent materials should be consulted. The phase diagram for a unary system shows the phase and phase changes of the system depending on temperature and pressure. In the case of binary alloys, the phase diagram usually shows the phase and phase changes depending on temperature and alloy composition at constant pressure, which is usually 1 atm. It is important to note that phase diagrams represent the system at equilibrium. Therefore, using high heating and cooling rates when driving the system along the temperature axis create systems that are not in equilibrium but instead determined by kinetics. Melting points will, for example, appear shifted, since the system will be kinetically trapped in a state different from the equilibrium one.

Focusing on metals only, which are the systems of relevance for my work, the most common phases of an alloy are a solid solution and an intermetallic phase. In a solid

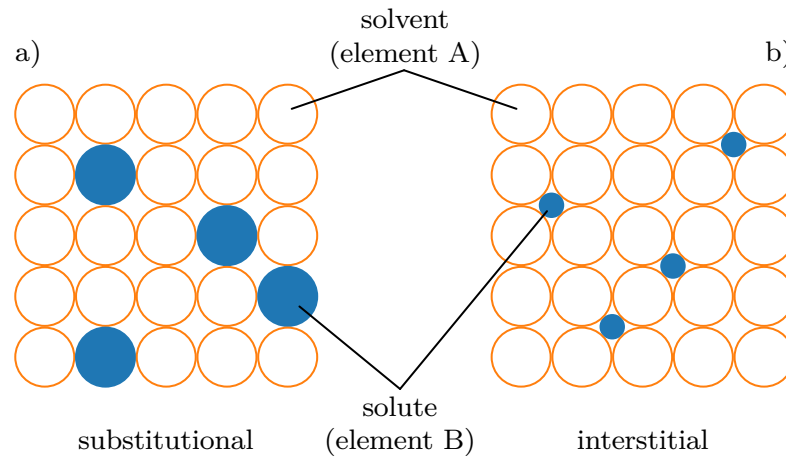


Figure 2.1: a) Schematic depiction of a substitutional alloy, where the solute substitutes a solvent atom. b) Schematic depiction of an interstitial alloy, where the solute atoms sit between the solvent atoms in interstitial lattice sites.

solution, element B, the *solute*, is dissolved in the crystal lattice of element A, the *solvent*. The phase structure of the solid solution is the same as the one of the solvent.⁴³ The limit of solid solubility depends on the similarity and difference between the atoms of solute and solvent.⁴³ If they have a similar size and the solute atoms replace the solvent atoms, the solid solution is called substitutional (Figure 2.1a). According to the *Hume-Rothery-rules*,⁴⁴ the atoms can deviate a maximum of 15% in size to form a substitutional solid solution. In addition to size requirements, the chemical affinity, relative valency and lattice type should be considered. If, for example, the elements have very different electronegativities, they tend to form a compound instead of an alloy, with polar covalent bonds between its constituents. Finally, it is important to mention that requirements on atom size and electronegativity are general rules with many exceptions. However, they give a qualitative estimate if two atoms would form a substitutional solid solution. If the difference in radius of the atoms is big enough, an interstitial solid solution will form instead, where the solute atoms occupy interstitial sites of the solvent (Figure 2.1b).

In phase diagrams, solid solutions are often denoted with a lowercase Greek letter. In Figure 2.2 that depicts the binary phase diagram for Ag and Cu, the solid solutions are denoted α and β . If it is not possible for a particular composition to form either

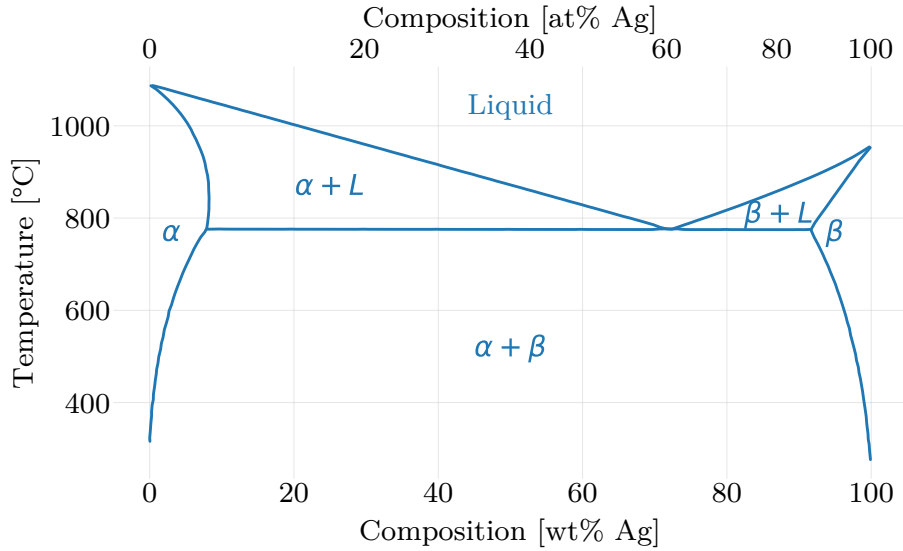


Figure 2.2: Phase diagram of AgCu. The α and β phases are at both sides of the diagram, at high Cu and Ag concentrations, respectively. The largest part of the phase diagram in the center corresponds to a two-phase coexistence region, where the α and β phase are present simultaneously. L denotes the liquid phase. In the regions $\alpha + L$ and $\beta + L$ coexist the solid with the liquid phase. The data are from Kawecki et al.⁴⁵

an α or β phase, a mixture of both is formed, as also indicated in Figure 2.2. This two-phase coexistence region is denoted as $\alpha + \beta$, where both phases are saturated at equilibrium. The amount of each phase in the mixed phase can be calculated using the *Lever rule*.³⁹ Finally, a region where an alloy does not fully mix is called a miscibility gap. If the crystal structure of an alloy differs from both constituents', it is called an intermetallic compound or intermetallic phase.

An example of a simple phase diagram is the one for AuAg (Figure 2.3). This system forms a random alloy throughout the whole composition range and has a small area between the liquidus and solidus lines, where liquid and solid phases coexist. In a random alloy the atomic site positions of one of the constituent elements are independent of the other constituents' lattice sites, or in other words, random alloys have no ordering in their structure.^{46,47}

There are several ways to create bulk alloys from their constituents. One way is to mix the elements in liquid form, which generally works well for metals. Once mixed,

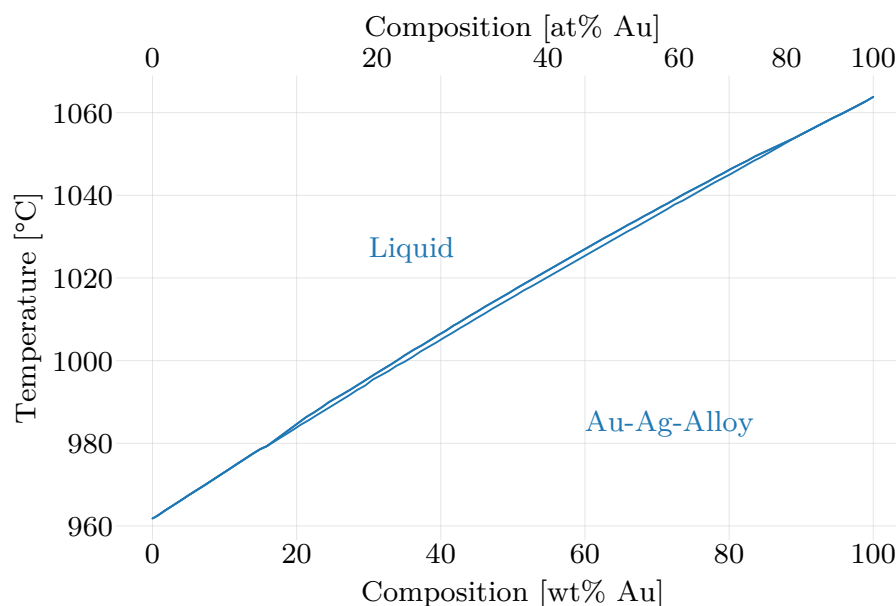


Figure 2.3: Phase diagram of AuAg. For the largest part of the diagram, it forms either a random alloy in the solid state (below the solidus line) or is mixed in the liquid phase. In the small area between the liquidus and solidus lines a liquid and solid phase exist simultaneously. The data are from Okamoto et al.⁴³

the liquid can be cooled and upon solidification the solid-state alloy is formed.⁴³ Alternative ways to make alloys include the use of solutions containing the components as salt,⁴⁸ electrolysis,⁴⁹ or simultaneous reduction of oxides of the components.⁵⁰

At the nanoscale, additional effective ways to make alloy nanoparticles are via colloidal synthesis or via thermal annealing of layered thin films.^{51,52} The route of thermal annealing was used in **Paper I, II, III, IV and V**, by nanofabricating layered nanoparticles comprised of two metals by means of nanolithography (see chapter 6).⁵³ During the high temperature treatment, the system reduces the Gibbs free energy by eliminating the concentration gradient of metal A and B via atomic diffusion in the solid state, resulting in a homogeneous concentration in the end of the process. This behavior can be described with *Fick's law of diffusion*.⁵⁴

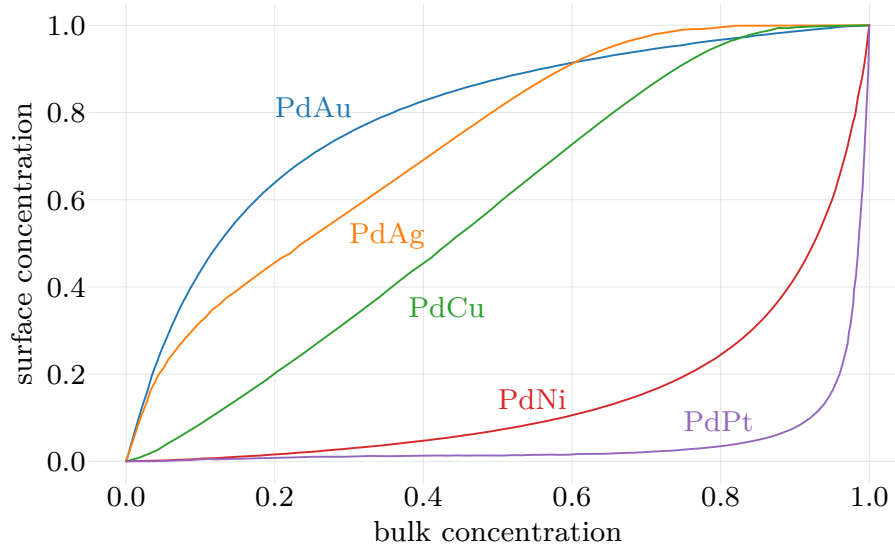


Figure 2.4: Calculated surface segregation for different Pd alloys for the (111) plane in vacuum at 600 K. Depending on the composition and the constituents, the surface concentration differs considerably from the bulk composition. Common reasons driving the segregation are the surface energy, size mismatch of the atoms, or the gas environment. The shown concentrations are with respect to the element alloyed with Pd. The data are from Zhao et al.⁵⁵

2.2 Segregation

Segregation describes a phase separation process in alloys driven by de-mixing, for instance at a surface, due to local energetics that are different than in the bulk of the crystal or the presence of surface species such as adsorbed oxygen.^{55,56} Such segregation can appear in different forms. For example, dendrites may form inside the material and thereby create regions in the bulk material with an altered composition.⁵⁷ Alternatively, one can get segregation due to an inhomogeneous freezing process upon solidification⁵⁷ and many more. For the work presented in this thesis, equilibrium segregation at the surface of an alloy is most important. To this end, theory predicts for noble/transition metal alloys that the surface composition is expected to – sometimes dramatically – differ from the bulk composition. This is exemplified for different Pd alloys in Figure 2.4. Common reasons driving the segregation are among others the surface energy, size mismatch of the atoms, or the gas

environment.⁵⁵

An estimate of which alloy that will exhibit significant surface segregation in vacuum or inert atmospheres can be obtained by looking at the surface energies of the constituents since the alloyed system tries to attain a state of lowest energy. Therefore, the element with a lower surface energy will segregate to the surface and the driving force for this process will be larger, the larger the difference in surface energy between the alloy constituents. For Pd the surface energy is 2.05 J/m^2 and for Au 1.5 J/m^2 .⁵⁸ Hence, as can be seen in Figure 2.4, Au is expected to segregate to the surface in vacuum. Nickel (Ni) on the other hand has a higher surface energy than Pd with 2.45 J/m^2 and therefore Pd is segregating to the surface in a PdNi alloy.⁵⁸ Importantly, however, most of the time these materials are not used in vacuum but at ambient or even high-pressure conditions, such as during a catalytic reaction. Under these conditions physisorption and chemisorption of atomic and molecular species on the surface play a significant role and will alter the segregation behavior.⁵⁹ In most cases, if one of the gas atoms or molecules interacts strongly with one of the alloy constituents, it will tend to enrich on the surface and create a surface composition not present in vacuum.⁶⁰ However, cases also have been reported where the less reactive constituent of the alloy is pulled to the surface.⁶¹

3 Palladium-Hydrides

Pd was discovered in 1803 by William Hyde Wollaston and already in 1866 Thomas Graham discovered that Pd can absorb large amounts of hydrogen gas.^{62,63} Nowadays, Pd is used in many catalytic applications, for example, in fuel cells or three-way catalysts.^{64,65} However, Pd is also used in dentistry, jewelry or for hydrogen sensing applications.^{66,67} In my work, I combined the hydrogen absorption abilities of Pd with its optical sensing capabilities, and I investigated its use for nanothermometry of nanoparticles interacting with light.

3.1 Hydride Formation

If Pd is exposed to hydrogen, it will absorb hydrogen and eventually phase-transform into Pd-hydride. As the first step during this entire process, the hydrogen molecule will get attracted to the Pd surface by van der Waals forces that can be described with a Lennard-Jones potential. Consequently, the hydrogen molecule will eventually physisorb on the Pd surface, as depicted in the corresponding energy landscape in Figure 3.1.⁶⁸ Subsequently, the hydrogen molecule, H_2 , will dissociate spontaneously since the energies for the system in molecular and atomic form cross below zero and the dissociative chemisorption therefore happens spontaneously, without any activation barrier. This barrierless dissociative chemisorption behavior of hydrogen can also be observed on metals like Pt or Ni.⁶⁹ Once hydrogen is dissociated, atomic hydrogen occupies three-fold hollow sites on the surface.⁷⁰ Hydrogen will diffuse into the bulk of the metal once a full coverage of hydrogen is obtained due to their favorable energetics of the subsurface sites compared to bulk sites (Figure 3.1). The subsurface interstitials will be occupied first and remain fully occupied even at low hydrogen pressures when bulk sites remain unoccupied. Upon further increasing the hydrogen partial

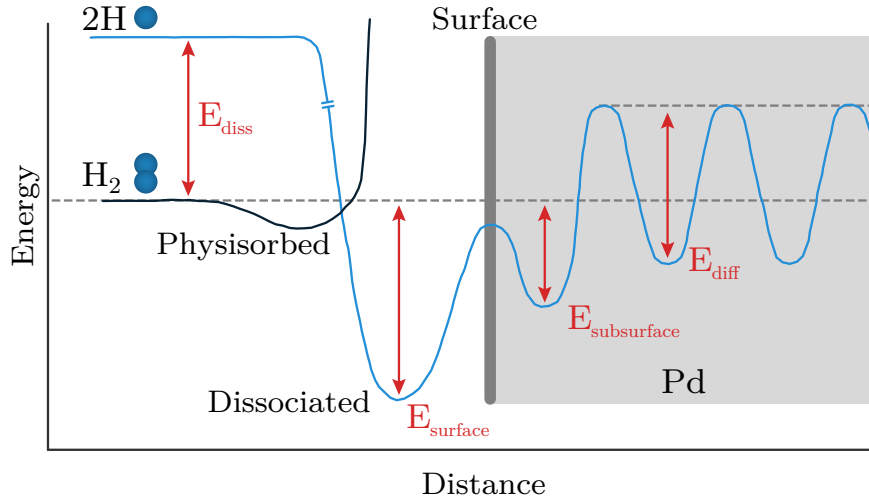


Figure 3.1: Potential energy diagram for the adsorption, dissociation, absorption, and ultimately diffusion of hydrogen into bulk Pd. The molecular hydrogen will dissociate on the surface and then absorb and dissociate into the lattice. The figure is adapted from Behm et al.⁶⁸

pressure around the system, the hydrogen atoms will start diffusing into the bulk of the Pd host lattice. At low hydrogen pressures the hydrogen atoms thus form a solid solution in the Pd lattice. This phase is called the α -phase in which the hydrogen atoms are sparsely distributed, and the H-H interactions therefore are weak. Accordingly, the dependence of the hydrogen content in the metal on the hydrogen pressure can be described by Sieverts' law, which states that the hydrogen content is proportional to the square-root of the hydrogen pressure.⁷¹

Upon further increasing hydrogen pressure, more and more hydrogen atoms enter the host lattice and the H-H interactions increase due to electronic effects induced by the electrons that “accompany” the hydrogen, and due to the local strain the hydrogen exerts onto the lattice. At a critical pressure, the combination of these two effects leads to the nucleation of a new phase – the hydride – which occurs all over the lattice and in which Sieverts' law does no longer apply.⁷² This hydride phase is also referred to as the β -phase. At the first-order phase transformation from the α -phase to the β -phase both phases co-exists and an incremental change in hydrogen pressure will lead to a dramatic increase in the amount of absorbed hydrogen until the stoichiometric hydrogen-Pd ratio of the hydride, which is $PdH_{\approx 0.7}$ for bulk systems at room temperature, is reached.⁷³ This hydride formation process is con-

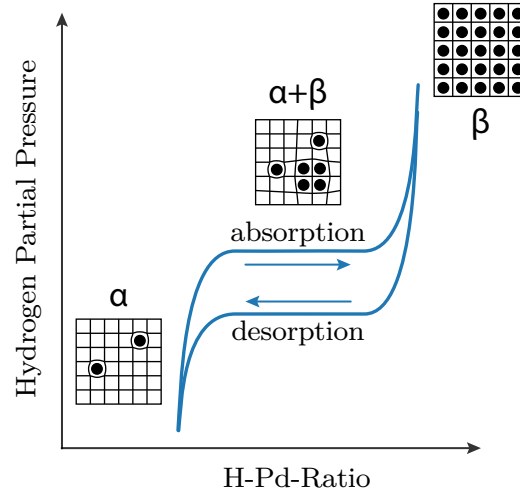


Figure 3.2: A pressure-composition isotherm shows the relation between external hydrogen pressure and the amount of hydrogen in the Pd lattice. In the α -phase at low hydrogen pressures, the hydrogen forms a solid solution with the Pd. With increasing H-H interactions, due to increasing hydrogen concentration in the solid solution induced by increasing hydrogen pressure, the hydride phase (β -phase) starts to nucleate and co-exists with the solid solution (α -phase) across the first order phase transformation characterized by the “plateau” in the isotherm. Once the phase transformation is complete, further increase of the hydrogen pressure leads to only a minor change in the Pd hydrogen ratio.

veniently depicted in a pressure-composition isotherm (from here forward just called “isotherm”), which plots the hydrogen (partial) pressure against the hydrogen content in the system expressed as metal/hydrogen ratio at constant temperature, and is characterized by the plateau region that depicts the first-order phase transformation from the solid solution (α -phase) to the hydride phase (β -phase), during which the two phases coexist (Figure 3.2). A first-order transition is here defined as a process that includes latent heat, which means that the system therefore is not changing its temperature in the process. Notably, the Pd-hydride first-order transformation exhibits hysteresis between hydride formation and decomposition, as a result of lattice strain.^{74,75}

During the hydride formation process several things change in the system. The most obvious change is that the hydrogen atoms that occupy the interstitial lattice positions strain the host Pd lattice, which increases the lattice constant from 3.890 Å

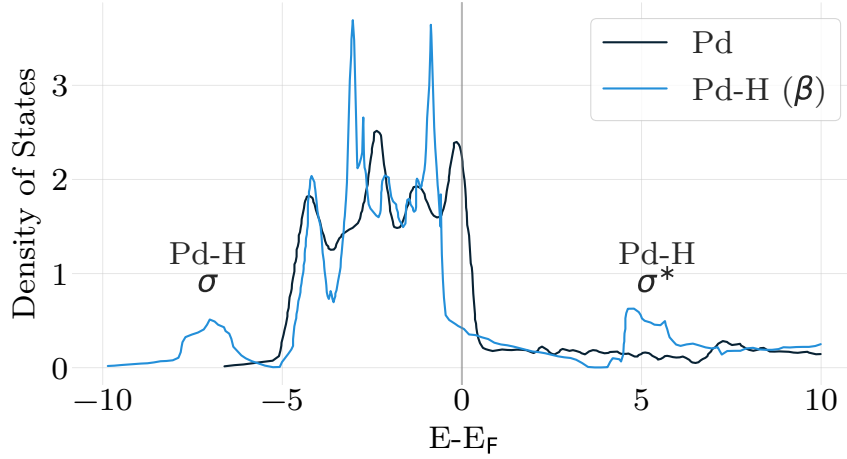


Figure 3.3: The density of states (DOS) for neat Pd and Pd-hydride (β -phase), in which the hydrogen electrons fill the Pd $4d$ band. This leads to a shift of the Fermi level. Furthermore, due to the formed Pd-H bonds, corresponding bonding, σ , and antibonding, σ^* , bands appear in the DOS of the hydride. The data are taken from Dekura et al.⁸⁰

up to 4.025 Å in the fully hydrided state. That increase in lattice constant results in a volume increase of about 10 %.^{76–78} Equally important are changes in the electronic structure induced by the phase transition. Specifically in neat Pd, the $4d$ band is only partially filled and intersects the Fermi level (see density of states (DOS) in Figure 3.3). In the α -phase, the H $1s$ electrons contribute mostly to the Pd-H bonds and changes to the overall DOS are minimal.⁷⁹ However, when the hydride is formed, distinct changes appear through which Pd-H interactions increase in the β -phase, and the bonding, σ , and antibonding, σ^* , bands are now visible in the DOS. As a consequence, the $4d$ band fills up at this stage, which leads to a shift of the Fermi level to the $5s$ band.^{79,80} Importantly, these changes to the electronic structure result in changes of the complex dielectric function of the system, as I will discuss in more detail in chapter 4.

3.2 Temperature Sensing using Palladium-Hydride

Metal nanoparticles and their ability to efficiently absorb light are utilized in many applications like microelectronics,^{81,82} photovoltaics,⁸³ photochemical reactions,²⁶ med-

icine,⁸⁴ optical metamaterials,⁸⁵ and more (see chapter 4).^{86–88} The absorbed light is converted into heat, as governed by the absorption cross section of the nanoparticle and the irradiated light intensity. This process of conversion of light into heat thus makes nanoparticles great heat sources at the nanoscale and they have been used, for example, in hyperthermia therapy to treat diseases with local heating or in photothermal chemistry to decrease overall energy consumption.^{86,89} Therefore, it is important to be able to accurately measure the temperature of nanoparticles in general and when they are heated via the absorption of light in particular. This is important information to understand experimental studies of plasmon driven catalysis (see section 5.2). Obtaining accurate and absolute temperature values of micro- and nanostructures is, however, not as straightforward as measuring temperature on the macro scale. For example, common macroscale temperature measurement techniques struggle to establish good thermal contact to the nanostructures at hand, they are invasive and thus alter the nanoparticle temperature due to a large mismatch in thermal mass, or they simply are not able to access the small area of interest and therefore lack the necessary spatial resolution.^{90–92}

Consequently, a variety of methods that enable nanoscale temperature measurements have been developed in the last decades. Famous examples are infrared thermography, Raman scattering, the various uses of luminescence, scanning thermal microscopy, and many more.^{91–93} Since every technique has its specific advantages and disadvantages, careful evaluation of the most suitable method should be done for a specific application, depending on if high spatial, temporal, or temperature resolution is needed. Since luminescence-based nanoscale temperature measurement techniques constitute a large subgroup of this field, I would like to give a brief overview over these techniques.

Luminescence is based on the transitions of electrons from their ground state to a higher energy state, which releases a photon upon relaxation.⁹⁴ Depending on how the electrons are excited in the first place, it is called photo-, electro-, chemi- (and more) luminescence. The different luminescence-based temperature measurement techniques utilize different probes like organic dyes or quantum dots and even measure different properties of the received photons, such as peak energy, intensity or life-time of the excited states.⁹¹ All these properties change with temperature because the non-radiative transition rate for the electrons is temperature depended.⁹⁴ One drawback

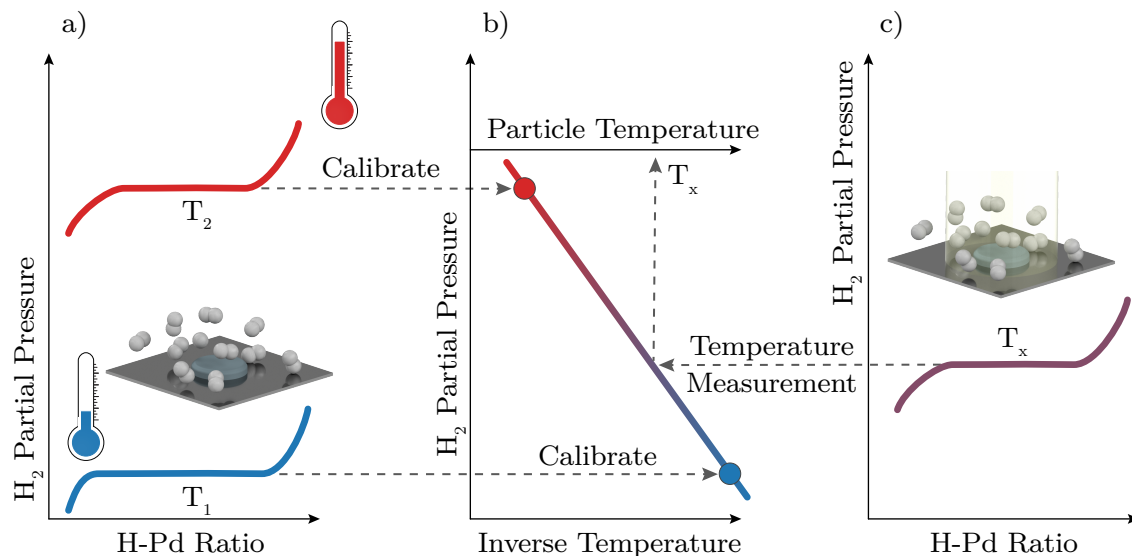


Figure 3.4: a) The plateau pressure depends strongly on temperature, where a higher temperature results in a phase transition at higher hydrogen pressure. b) The Van 't Hoff plot reveals a linear relation when plotting the hydrogen pressure on a semilogarithmic scale against the inverse temperature. c) By determining the phase transition pressure of a particle and correlating this pressure with a premeasured Van 't Hoff plot, one can determine an unknown temperature of a hydrogen absorbing particle, such as Pd.

of luminescence-based temperature probes, as well as of most other methods, is that they either measure the temperature indirectly, for example, via a molecular or quantum dot probe deployed close to the nanoparticles of interest, or require relatively complex instrumentation to gain direct access to the temperature, such as the use of Anti-Stokes thermometry, requiring at least a laser and a dark-field microscope.^{93,95,96} As a completely new approach to measure temperature at the nanoscale in a direct and reasonably simple way, I have explored the use of the Pd-hydride formation process, as described in **Paper III**.

Specifically, I utilized the phase transformation from the α - to the β -phase in Pd, which depends on temperature, where a higher temperature shifts the phase transition to higher hydrogen pressures (see Figure 3.4a). This intrinsic effect makes it a great candidate to measure the temperature of the Pd itself since the “probe” is

not adjacent to (as with e.g., luminescence) but “inside” the system of interest. This is particularly useful if the Pd consists of small nanoparticles where it otherwise is difficult to determine the correct temperature *in situ*, as discussed above. Specifically, this method works such that by determining the phase transition pressure for at least two temperatures, one can create the so-called Van ’t Hoff plot, which correlates the temperature with the hydride formation plateau pressure (see Figure 3.4b). The corresponding Van ’t Hoff equation is

$$\ln\left(\frac{P}{P_0}\right) = \frac{\Delta H}{RT} - \frac{\Delta S}{R}, \quad (3.1)$$

where P is the plateau pressure, P_0 the atmospheric pressure, ΔH and ΔS the change in enthalpy and entropy, R is the universal gas constant and T the temperature. Plotting the temperature as inverse and the hydrogen partial pressure on a logarithmic scale the resulting plot yields a linear correlation, where the change in enthalpy upon hydride formation corresponds to the slope and the corresponding change in entropy to the intersection with the y-axis.

The transformation of Pd nanoparticles into the hydride phase can be monitored by using visible light via localized surface plasmon resonance (more in section 4.5) measurements based on the systems’ optical extinction spectrum. Specifically, by tracking the extinction difference at two different wavelengths in the extinction spectrum one can construct an isotherm that depicts the hydrogen pressure versus the measured optical extinction difference, which is proportional to Pd-hydrogen atomic ratio, as shown by Langhammer et al.⁹⁷ Hence, an isotherm constructed from the extinction spectra measured during hydrogen absorption exhibits the characteristic α -phase, β -phase, and their coexistence region ($\alpha + \beta$) at the first-order phase transformation to the hydride.

With this information at hand, generating a Van ’t Hoff plot at known temperatures for a Pd nanoparticle sample can subsequently be used “in reverse” to obtain particle temperatures from the plateau pressure derived from an isotherm measurement at unknown temperature (see Figure 3.4c). Specifically, as I have shown in **Paper III**, it can be used to obtain absolute nanoparticle temperatures at various levels of illumination with a resolution of 1 °C. We used the optical hydrogen nanothermometry to quantify the heating effect induced by light absorption and compared

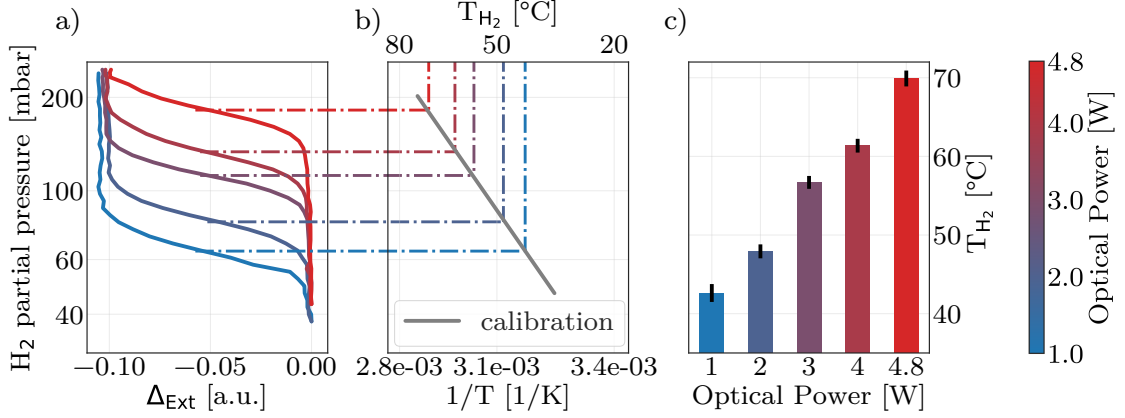


Figure 3.5: a) Isotherms measured at constant reactor temperature with irradiated optical powers ranging from 1 W to 4.9 W. A clear rise in plateau pressure indicates higher particle temperatures upon increasing optical power. b) The pre-recorded Van 't Hoff calibration is used to obtain the particle temperature, T_{H_2} from the measured plateau pressures. c) The extracted particle temperature shows a clear increasing trend with increasing optical power.

these to temperature measurements obtained by a thermocouple. As an example, an array of Pd nanodisks on glass illuminated with a varying optical power of a mercury xenon arc light source is shown in Figure 3.5. By illuminating the sample with increasing optical powers, a clear rise in plateau pressure can be observed as the particle temperature increases due to increasing irradiated light intensity and thus absorption (Figure 3.5a). The Van 't Hoff calibration has been measured beforehand by increasing the temperature of the reactor used for the experiments and by using a low-power light. This calibration can then be used to determine the particle temperatures under different levels of illumination by calculating the intersection with the pre-recorded Van 't Hoff plot (Figure 3.5b). In the depicted example, I measured the particle temperature from 1 W to 4.8 W optical power, revealing a distinctly and linearly increasing particle temperature with increasing optical power (Figure 3.5c).

4 Dielectric Functions and Plasmonics

The dielectric function of an element describes fundamental properties of the material and is used to predict the response to electromagnetic radiation. Such a response is for example the LSPR in metal nanoparticles that leads to optical cross sections of these particles that are larger than their geometrical one. The LSPR phenomenon is of wide interest as it can increase energy absorption in nanostructures,⁹⁸ influence chemical reactions,⁹⁹ increase photovoltaic output of solar cells¹⁰⁰ and be used for optical sensing.¹⁰¹

4.1 Free Electron Gas Model

To understand plasmons it is best to start by looking at the behavior of metals when they interact with electromagnetic radiation. One way to do this is by using the free-electron-gas model. It describes freely moving electrons in a fixed positive ion background. This model is sometimes also called the plasma model.¹⁰²

The driving force to excite plasmons is the external electric field, \mathbf{E} , which can be expressed as a harmonic wave $\mathbf{E}(t) = \mathbf{E}_0 e^{i\omega t}$. The resulting motion of the electrons is a classical harmonic oscillator and can therefore be written as¹⁰²

$$m\ddot{\mathbf{x}} + m\gamma\dot{\mathbf{x}} = -e\mathbf{E}. \quad (4.1)$$

Here γ is the characteristic collision frequency, $\gamma = 1/\tau$, and τ is the relaxation time. Further, we have the effective mass, m , of an electron and the elementary charge e .

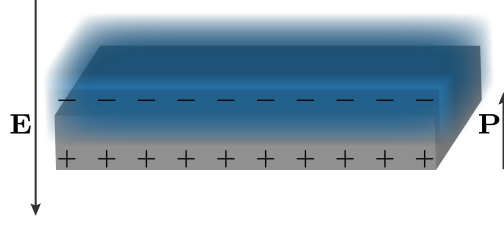


Figure 4.1: Volume plasmon in a slab of metal. The displacement of the electrons due to the electric field \mathbf{E} creates the polarization \mathbf{P} .

The solution to Equation 4.1 is¹⁰²

$$\mathbf{x}(t) = \frac{e}{m(\omega^2 + i\gamma\omega)} \mathbf{E}(t). \quad (4.2)$$

With the macroscopic polarization $\mathbf{P} = -nex$ this leads to

$$\mathbf{P} = \frac{-ne}{m(\omega^2 + i\gamma\omega)} \mathbf{E} \quad (4.3)$$

with n being the number density. The displacement of the electron cloud can be illustrated as shown in Figure 4.1.

The dielectric displacement, \mathbf{D} , from Maxwell's equations is defined as

$$\mathbf{D} = \epsilon_0 \mathbf{E} + \mathbf{P}, \quad (4.4)$$

with ϵ_0 being the vacuum permittivity, which gives us

$$\mathbf{D} = \epsilon_0 \mathbf{E} - \frac{-ne}{m(\omega^2 + i\gamma\omega)} \mathbf{E} \quad (4.5)$$

$$\mathbf{D} = \epsilon_0 \left(1 - \frac{\omega_P^2}{\omega^2 + i\gamma\omega} \right) \mathbf{E} = \epsilon_0 \epsilon \mathbf{E}. \quad (4.6)$$

ω_P is the plasma frequency with $\omega_P = \frac{ne^2}{\epsilon_0 m}$. One can also see that in Equation 4.6

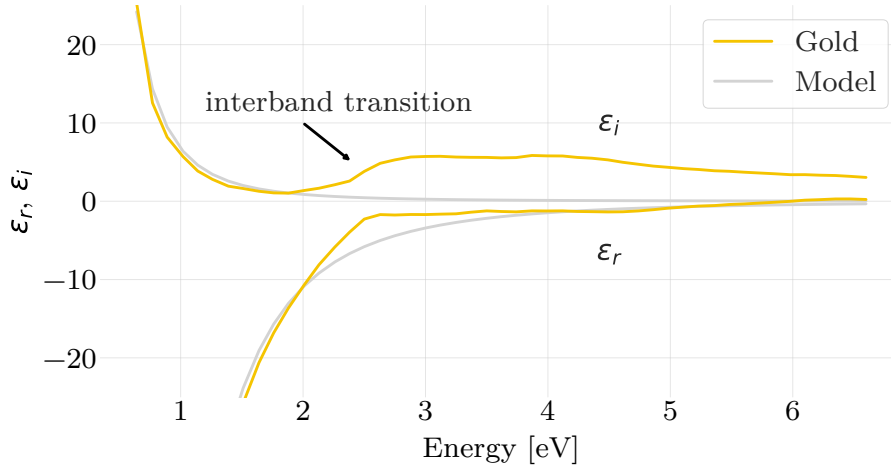


Figure 4.2: The dielectric function of Au from Johnson and Christy.¹⁰⁴ In grey the Drude model is fitted to the data. One can see that the overall agreement for the real part is good. However, the model description of the imaginary part works only until the onset of the interband transitions in Au. Adapted from Maier.¹⁰²

the complex dielectric function

$$\epsilon(\omega) = 1 - \frac{\omega_p^2}{\omega^2 + i\gamma\omega} \quad (4.7)$$

appears. This dielectric function is also known as the free-electron Drude-type.¹⁰³ The complex dielectric function can be written with its real and imaginary part separated as

$$\epsilon(\omega) = \epsilon_r(\omega) + i\epsilon_i(\omega) \quad (4.8)$$

where the parts are

$$\epsilon_r(\omega) = 1 - \frac{\omega_p^2\tau^2}{1 + \omega^2\tau^2} \quad (4.9)$$

$$\epsilon_i(\omega) = \frac{\omega_p^2}{\omega(1 + \omega^2\tau^2)} \quad (4.10)$$

Despite its ability to rationalize the core concept, a simple model as introduced above also comes with limitations, which can be seen in Figure 4.2. It shows the dielectric

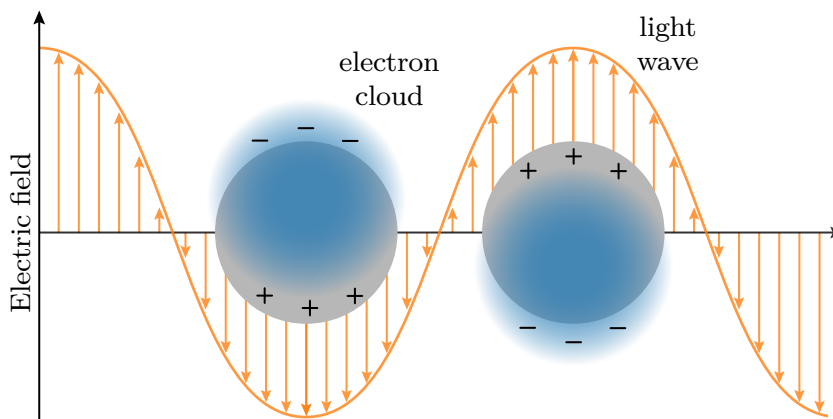


Figure 4.3: The free electrons of the nanoparticle are displaced by the electric field of the light and start oscillating. This is the classical picture of a localized surface plasmon resonance.

function of Au experimentally obtained by Johnson and Christy¹⁰⁴ and the dielectric function of Au obtained using the free-electron-gas model (Equation 4.7) fitted to the experimental data. At around 2.5 eV a strong deviation can be seen. At this point photons can excite interband transitions between the 5d and the 6sp-band above the Fermi level with a high efficiency.^{105,106} This is an effect that is not included in the free-electron-gas model, as it treats mainly the low frequency intraband contributions.¹⁰³ Better and more accurate ways to describe the dielectric function will be discussed in section 4.4.

4.2 Localized Surface Plasmon Resonance

In the section above, we have seen that metals can be described in a simplified way with the plasma model, which generates the dielectric function as an important descriptor of metal – electromagnetic radiation interactions. If electrons in metals are displaced by an external electric field the positively charged atom cores cause a restoring force. Due to these two counteracting forces, an oscillation of the electrons with respect to the atomic cores is excited. These oscillations do not only occur in bulk but can also be confined to a surface and either constitute a propagating or a

standing wave, which then are called surface plasmons or surface plasmon polaritons. If the plasmon is confined in a nanoparticle it is called localized surface plasmon (Figure 4.3).

LSPs are excited if the particle size is smaller than the wavelength, λ , of the external electric field and can conveniently be described by the *quasi-static approximation*.¹⁰² This model assumes that the particle can be treated as exposed to a static electric field because it is much smaller than the wavelength. Based on the Laplace equation $\nabla^2\Phi = 0$, which can be used to describe the electric field $\mathbf{E} = -\nabla\Phi$, one can introduce the dipole moment, \mathbf{p} , at the center of the particle (for a more detailed derivation see Maier¹⁰²), which reads as

$$\mathbf{p} = 4\pi\epsilon_0\epsilon_m a^3 \frac{\epsilon - \epsilon_m}{\epsilon + 2\epsilon_m} \mathbf{E}_0. \quad (4.11)$$

Here ϵ_m is the dielectric constant of the surrounding medium and a the radius of the particle. Like the dielectric function in the section above, one can then introduce a polarizability, α , via¹⁰²

$$\mathbf{p} = \epsilon_0\epsilon_m\alpha\mathbf{E}_0, \quad (4.12)$$

which gives us

$$\alpha = 4\pi a^3 \frac{\epsilon - \epsilon_m}{\epsilon + 2\epsilon_m}. \quad (4.13)$$

From this expression it is easy to see that the polarizability experiences a maximum if the denominator reaches zero.

$$\text{Re}\{\epsilon(\omega)\} = -2\epsilon_m \quad (4.14)$$

This is also called the *Fröhlich condition*.

From Equation 4.11 one can obtain the scattering, σ_{scat} , and absorption, σ_{abs} , cross sections as (see Bohren and Huffman¹⁰⁷ for details)

$$\sigma_{scat} = \frac{k^4}{6\pi} |\alpha|^2 = \frac{8\pi}{3} k^4 a^6 \left| \frac{\epsilon - \epsilon_m}{\epsilon + 2\epsilon_m} \right|^2 \quad (4.15)$$

$$\sigma_{abs} = k \text{Im}\{\alpha\} = 4\pi k a^3 \text{Im}\left\{ \frac{\epsilon - \epsilon_m}{\epsilon + 2\epsilon_m} \right\}. \quad (4.16)$$

For the sake of completeness and because it is the value most often measured experimentally, also the extinction cross section shall be mentioned here. It is obtained by the combination of Equation 4.15 and 4.16 according to the optical theorem.

$$\sigma_{ext} = \sigma_{abs} + \sigma_{scat} \quad (4.17)$$

$$\sigma_{ext} = 9 \frac{\omega}{c} \epsilon_m^{3/2} V \frac{\epsilon_i}{[\epsilon_r + 2\epsilon_m]^2 + \epsilon_i^2}. \quad (4.18)$$

Here we can see again that the cross sections are maximized when the Fröhlich condition is met. At this point, I also note that the particles have a larger optical cross section than their geometrical cross section, which means they interact a lot more strongly with light than just casting a shadow.¹⁰²

It is further interesting to notice that scattering and absorption scale differently with nanoparticle size. Absorption dominates due to the a^3 scaling (Equation 4.16) in the small particle regime ($a \ll \lambda$)¹⁰², while scattering dominates for larger particles due to the a^6 scaling (Equation 4.15).

4.3 Finite Difference Time Domain Electrodynamic Simulations

The Finite Difference Time Domain (FDTD) method is a numerical computational technique to simulate electrodynamics and calculate, for example, the LSPR of nanoparticles and nanostructures. In contrast to analytical theories, like *Mie* or *Gans*,^{102,107} FDTD is not limited to idealized shapes like spheres and spheroids. FDTD works by solving Maxwell's equations. They are solved in the time domain, which has the advantage that with a single run one gets a broadband result and not just one frequency. The finite difference in FDTD comes from the finite-difference approximation for the derivative¹⁰⁸

$$\frac{df_{1.5}}{dx} = \frac{f_2 - f_1}{\Delta x}, \quad (4.19)$$

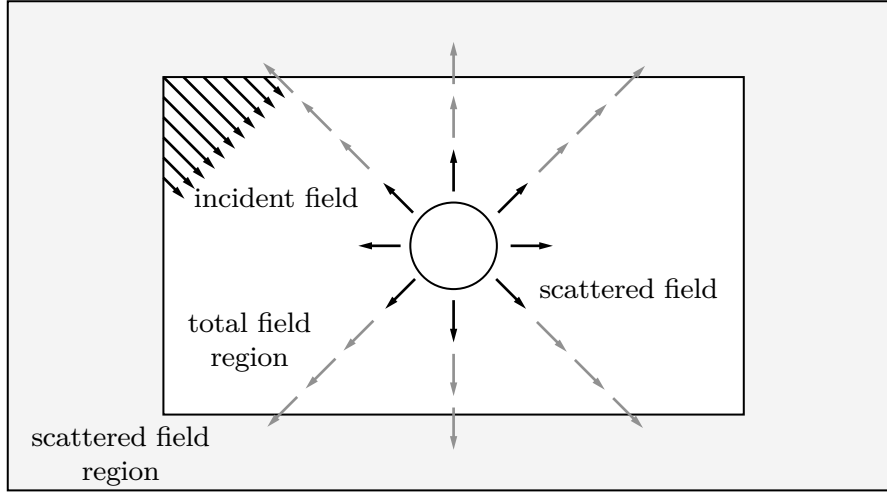


Figure 4.4: An example of a total field scattered field light source typically used in FDTD. In the total field region (black) both an incident and scattered (grey) field exist. In the scattered region, only scattered light is present. This eliminates backwards propagating energy and therefore 100 % of the injected energy is incident on the simulated object.

which means that finite steps in time are used. However, not only time is in finite steps, also the space is divided into finite steps, the so-called grid. If one looks at Maxwell's differential equation, one can see that the electric field depends on the change in the magnetic field (the curl) and vice versa. Calculating this curl in multiple dimensions becomes complex. To avert this, the electric and magnetic field components are staggered in space. Each electric field component ends up between magnetic field components in the grid and vice versa. For each grid space Maxwell's equations can now be solved. This concept was introduced in 1966 by Kane Yee¹⁰⁹ and is therefore called Yee grid.

FDTD has the advantage that it is an accurate, robust, and mature method, which has been used very successfully for decades. The numerical complexity further scales just linearly with the problem size¹⁰⁸ and it is easy to parallelize, and therefore take advantage of modern computers CPU architecture.¹¹⁰

To simulate an incoming plane wave, a source that is often used in FDTD is the total-field scattered-field source (Figure 4.4). With this source, the simulation is divided into different regions. The total field includes the incident and scattered

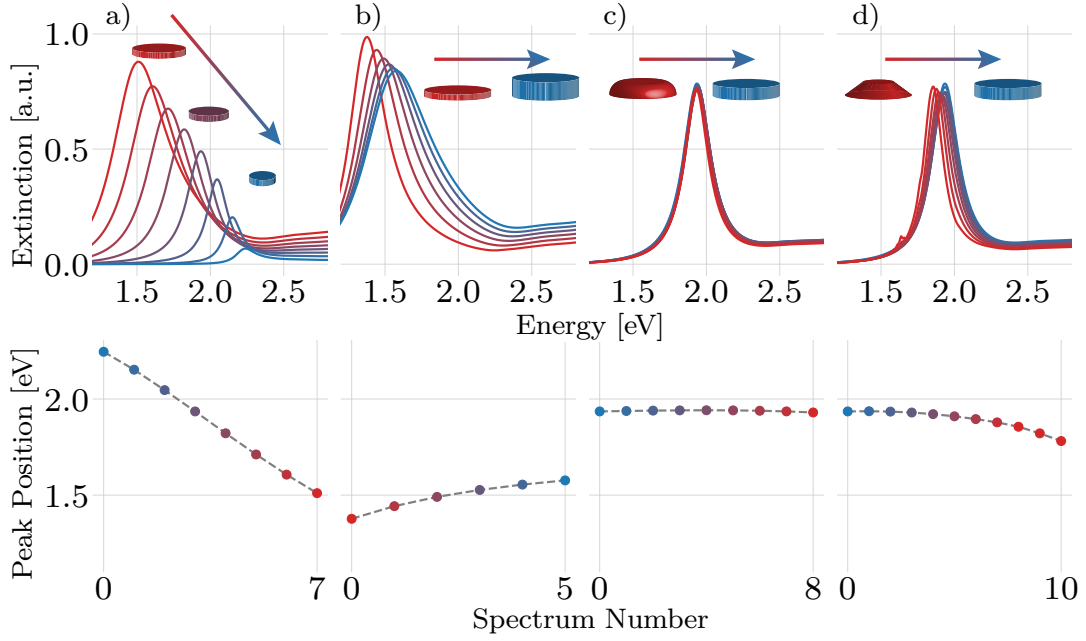


Figure 4.5: An overview of how different geometric features influence the LSPR of metal nanoparticles. The changes in disk a) diameter, b) height, c) top rounding radius, and d) tapering result in a different LSPR response. The bottom panels present the peak position as a function of the magnitude in geometric change, which demonstrates their different impact on the peak position. The calculation was done on a SiO_2 substrate with a refractive index of 1.46^{111} and the dielectric function for Au from Rahm et al.¹¹² (**Paper I**).

fields together and then there are regions which only include the scattered field. This eliminates backwards propagating energy and therefore 100 % of the injected energy is incident on the simulated object.¹⁰⁸

In this work, a single nanodisk was used in my simulations of the plasmonic response of alloy and neat metal nanoparticles investigated in the experiments. However, I want to stress that, in most experiments, the optical properties of the nanoparticles were measured from an array of nanodisks rather than from a single one. This may be problematic since, a priori, the optical response from an array is not identical to that of a single disk due to, for example, both near- and far-field coupling within the array.¹¹³ However, since simulating arrays of nanoparticles is computationally more demanding, it is a commonly used approximation. In my case, where the

experimentally studied arrays were made by Hole-Mask Colloidal Lithography (see chapter 6), they lack long-range order, and the average particle-particle distance is about 2 - 3 particle diameters. For such arrays, it has been shown by Antosiewicz et al. that the spectral position and full-width-at-half-maximum of the LSPR peak oscillates around the value of a single particle, with the specific values depending on the center-to-center distance of the particles in the array.¹¹⁴

As mentioned above, it is not only the nature of an array that is important for the optical response of plasmonic metal nanoparticles, but also the geometry of the individual nanostructures. To study individual nanostructures, FDTD is very suitable since it essentially enables the simulation of any shape. Therefore, I show some examples in Figure 4.5 to give an overview of how different geometric features influence the LSPR of metal nanoparticles, and I use the same geometrical features of a nanodisk that I used in the model in **Paper I, II, III, IV, and V**. Specifically, by reducing the diameter, the resonance frequency blueshifts, as can be seen in Figure 4.5a. This is exactly the behavior we expect by comparing it to spheres (see Equation 4.16). Also shown in Figure 4.5 is the influence of changing the nanodisk height b), the top rounding c) and the angle of the tapering d). One can see by looking at the lower half of the figure, where I plot the spectral position of the peak maximum as a function of geometry change (expressed as spectrum number), that changing the diameter of the disk yields the largest spectral shift in resonance frequency.

4.4 Dielectric Function of Selected Transition Metals and their Alloys

As discussed in the previous chapter, when computing the plasmonic properties of metal nanoparticles using electrodynamics simulations, such as FDTD, the complex dielectric function of the metal is a required input and simple descriptions, like we have seen above, lack the needed accuracy. For pure metals the dielectric functions are readily available from the literature, both derived in experiments and by first principles calculations.^{104,111,115–117}

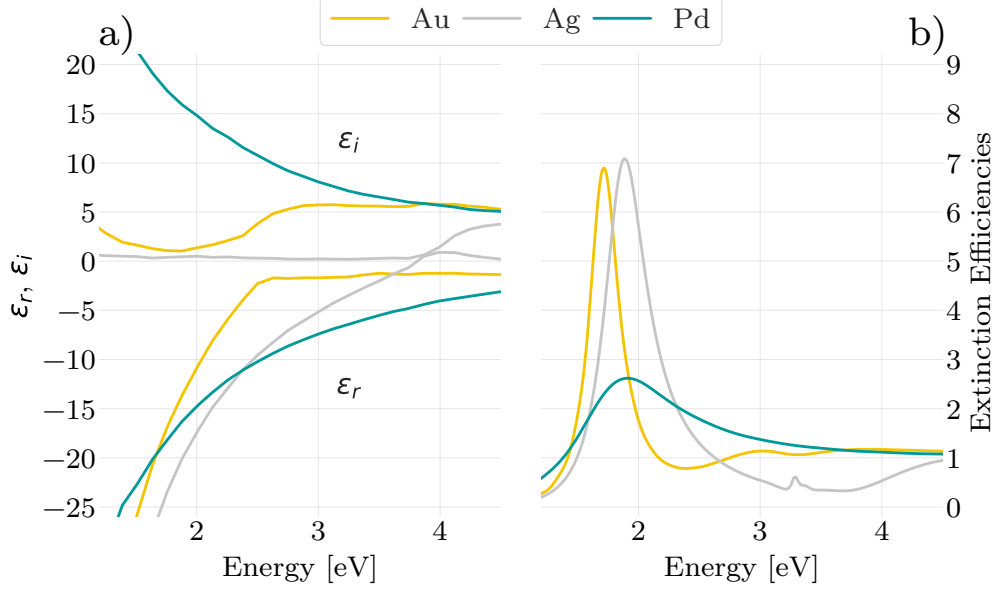


Figure 4.6: a) The dielectric functions of Au,¹⁰⁴ Ag,¹⁰⁴ and Pd.¹¹¹ The imaginary part of Au and Ag features a sudden rise at around 2.5 eV and 4 eV, respectively, where photons can excite interband transitions with a high efficiency. In the case of Pd, the d-band is only partially filled and intersects the Fermi level. Therefore, interband transitions dominate over the whole energy range and lead to a higher imaginary part than Au and Ag. b) The corresponding LSPR response calculated by FDTD using the dielectric functions above as input. Ag and Au feature a narrow and clear peak, whereas the Pd peak is not as strong and broader. The calculated response corresponds to a single nanodisk comprised of Au, Ag and Pd with a diameter of 140 nm and a height of 25 nm on a fused silica support.

Figure 4.6 depicts the dielectric functions of Au,¹⁰⁴ Ag,¹⁰⁴ and Pd¹¹¹ and the corresponding LSPR calculated by FDTD for a single disk. Ag exhibits a peak at higher energies because the real part of the dielectric function is lower and shifted to higher energies compared to Au. Comparing Ag with Pd, it is clear that the extinction spectrum does not have a peak as distinct as Au or Ag. This is because the d-band for Pd is partially filled and intersects the Fermi level, whereas Ag and Au have completely filled d-bands. The character of the electronic structure of Pd differs therefore compared to Au and Ag, which can also be seen in the LSPR peak that is not as strong and broader compared to Au and Ag. The width of the peak contains further

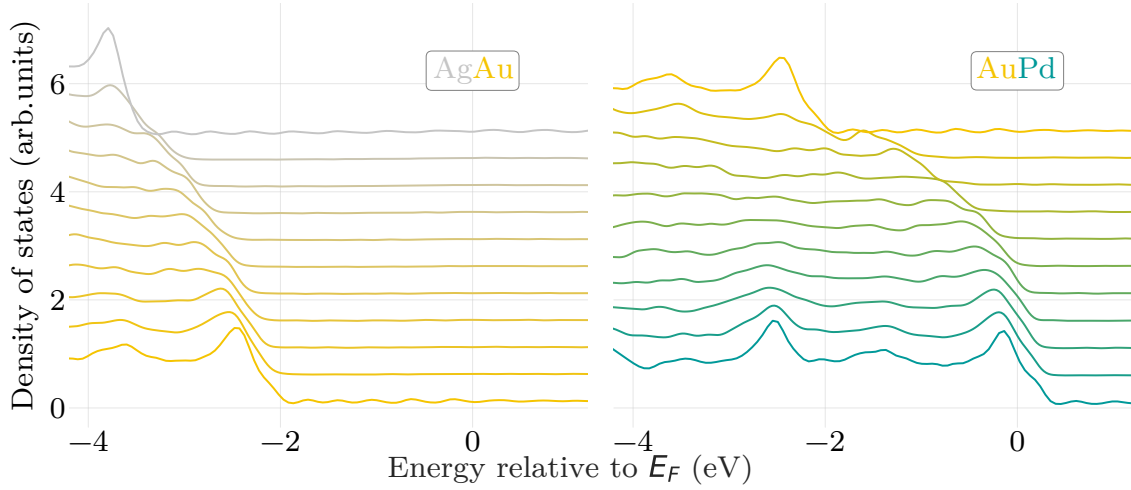


Figure 4.7: The electronic density of states of AuAg and AuPd alloys with the mixing ratio changing in 10 at.% steps, as calculated by DFT with van der Waals correlation.¹¹² In the case of AuAg, which both have filled d-bands, an almost linear shift of the d-band center becomes apparent, and it stays well under the Fermi level. In the case of AuPd, one combines two elements with open and closed d-bands, which already at low concentrations of Pd induces a strong nonlinear shift of the d-band center.

information on the lifetime of the plasmon. A short plasmon lifetime is the result of a high damping factor, as reflected by the imaginary part of the dielectric function. A large contribution to the damping factor for 140 nm nanoparticles of Ag, Au, and Pd in the shown energy range is damping due to interband transitions.¹¹⁸ Ag and Au both have a filled d-band well below the Fermi level (Figure 4.7), which leads to interband damping above a certain threshold, as can be seen in Figure 4.6a, whereas interband transitions across the whole shown energy range dominate for Pd. In this case, it can be concluded, that the plasmon lifetime for Ag and Au is longer than for Pd.

The dielectric function turns out to be experimentally challenging to accurately measure since features like surface roughness, morphology, surface oxidation, impurities and material thickness can dramatically affect the result.^{116,123,125} Additionally, even processing parameters during film growth, and the used measurement technique have an influence on the outcome.¹²³ Figure 4.8 illustrates the effect of processing param-

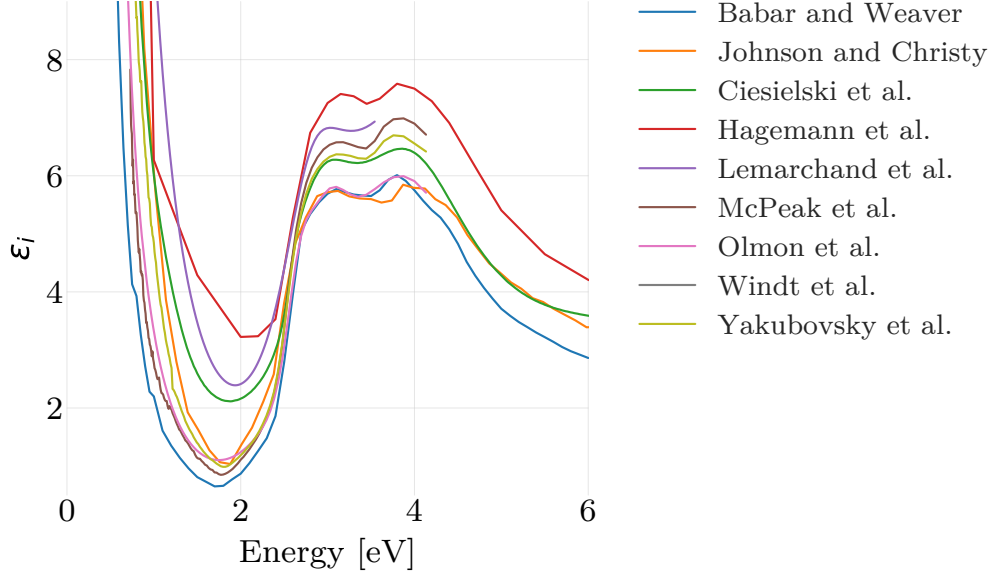


Figure 4.8: Experimentally measured imaginary parts of the dielectric function for Au collected from the literature. The overall shape of the curves is the same, but they are all different when comparing them in detail. The data are taken from Babar and Weaver,¹¹⁹ Johnson and Christy,¹⁰⁴ Ciesielski et al.,¹²⁰ Hagemann et al.,¹²¹ Lemarchand et al.,¹²² McPeak et al.,¹²³ Olmon et al.,¹¹⁶ Windt et al.,¹²⁴ and Yakubovsky et al.¹²⁵

eters and sample condition for pure Au. The overall trend is similar for all measured dielectric functions, but they differ in absolute values, especially in the region of the Drude peak, which ranges from almost 0 to around 2 eV. When it comes to alloys, the situation is no different and surface segregation and potential material inhomogeneities add further difficulties. Therefore, reliable dielectric functions for alloy materials are very scarce in the literature.

A common and better way than was shown before to describe the dielectric function of pure metals is with a model describing the Drude part of the dielectric function, ϵ^{free} , but also the interband transition part ϵ^{ib} . The Drude part describes the free electron low energy intraband contribution and a combination of step-like function and Lorentzian profile is used to describe the interband transition from the valence d-band to the conduction sp-band.^{103,126} Resulting in the frequency dependent dielectric function

$$\epsilon(\omega) = \epsilon^{free}(\omega) + \epsilon^{ib}(\omega). \quad (4.20)$$

Different electronic structure of the different metals makes it, however, difficult to derive or predict the dielectric function for alloys from, for example, simple linear interpolation schemes. For systems where the electronic structure is similar, like AuAg, or even ternary alloys like AuAgCu, one can use the Drude-Lorentz model.^{13,126} In the case of AuAg, we can see an almost linear shift of the d-band center (see Figure 4.7). If one, however, wants to generate a dielectric function for an alloy system where the constituent materials are of significantly different character in terms of their electronic structure, like, for example, AuPd, this simpler model is not applicable anymore. Specifically, in the case of AuPd, already a small amount of Pd shifts the d-band center closer to the Fermi level in a non-linear fashion (see Figure 4.7). This is the consequence of a hybridization of the Au $5d_{5/2}$ states and the Pd $4d$ states and leads to a smearing of the Au $5d_{5/2}$ states.¹²⁷

For AuAg alloys several attempts have been made to calculate, rather than measure, the dielectric function. The easiest way to do so is a weighted average of the dielectric functions of the component's Au and Ag. However, the corresponding results are questionable¹³ since the model does not take into account that there is only one onset of the d-band. A more sophisticated approach was used by Gaudry et al. in which a weighted average for the interband transition was used.¹²⁸ But even this approach neglects important physical change in the rest of the electronic structure and is not accurate enough. To increase the accuracy, a more complex analytical model was developed by Rioux et al. and fitted to experimental data.¹³ The key point of this approach is that the actual joined density-of-states is modelled and forms the basis of the analytical model. This was the first time a model for calculating the dielectric function for AuAg was based on the actual band structure.

From the above discussion, it is clear that it is not trivial to obtain dielectric functions of alloys, even for the “easy” case of AuAg, where the constituents have similar electronic structure, lattice constant, crystal structure and valences.¹³ For more complex systems more advanced first principles calculations like time-dependent density-functional theory has therefore to be used. A second consequence of the above analysis of methods is that, if one is interested in the optical properties of different and/or more complex alloys, complete and consistent data sets for dielectric functions do not exist to date. One must use either different experimental data sets,

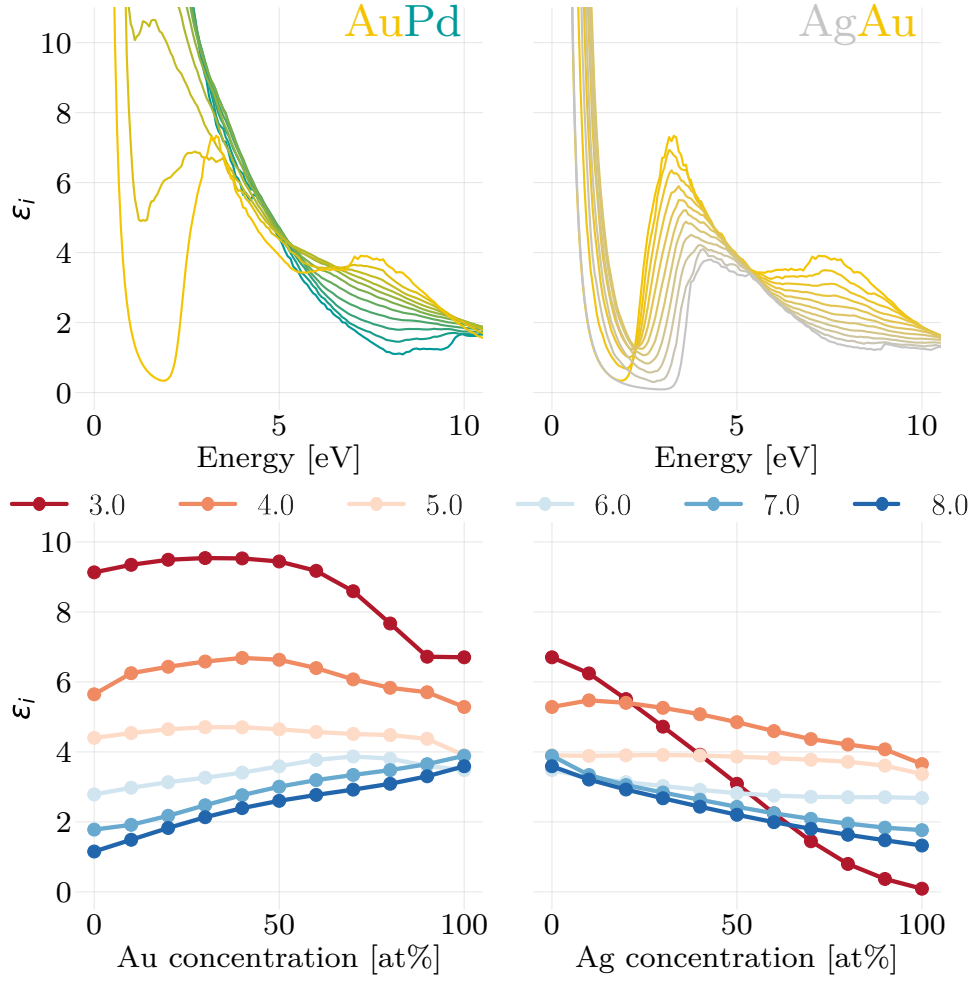


Figure 4.9: The dielectric functions of AuAg and AuPd alloys obtained by linear response time-dependent density function theory by Rahm et al. (**Paper I**) are an example for isovalent and non-isovalent alloys. The imaginary part is plotted versus the energy and versus the alloy composition for discrete energies, resulting in an energy cross section. The results show that the energy cross section in the low-energy region for the non-isovalent alloys exhibits a non-linear behavior.

which are often small in terms of the range of studied compositions and were only measured for a narrow spectral range, or one must work with models that are (too) simplistic. This situation motivated the work presented in **Paper I**, where we introduce a library of transition metal alloy dielectric functions for the binary alloys of Ag, Au, Cu, Pd, and Pt. To calculate the dielectric functions, we used linear

response time-dependent density function theory (LR-TDDFT) with special quasi-random structures, which can reproduce random alloys on a much smaller unit cell. This makes them an excellent choice for computational expensive techniques like LR-TDDFT.¹²⁹ The obtained dielectric functions are now freely available via a web application located at https://sharc.materialsmodeling.org/alloy_dielectric_functions/.

From a physics perspective, the different alloys considered in **Paper I** can be divided into isovalent and non-isovalent systems, i.e., AuAg (isovalent) and AuPd (non-isovalent), as depicted in Figure 4.9. As the key point, one can see that for the isovalent case the dielectric function changes linearly for all energies upon changing alloy composition, whereas for the non-isovalent case, especially in the low energy region up to around 4 eV, the dielectric function experiences a strong non-linear change. This clearly highlights that elements with different electronic structure show interesting non-linear behavior in their optical response upon alloying. An effect not captured by more simple analytical models.

The dielectric functions developed in **Paper I** created the opportunity to explore the light absorption abilities of different alloy nanoparticles by corresponding simulations. As we have discussed above, strong light absorption via LSPR turns nanoparticles into nanosized heat sources which, depending on the application, can be a wanted or unwanted effect.^{98,130–132} Specifically, I used the calculated alloy dielectric functions to investigate the effect of alloying and size on light absorption in **Paper IV**. In the paper we screened ten different alloys combined from the five late transition metals, Au, Ag, Cu, Pd, and Pt, whereas we benchmarked three alloy systems with nanofabricated samples. A section of the screening results can be seen in Figure 4.10, where the integrated absorption efficiency of AuAg, PtPd, and AuPd single particles in the range from 40 nm to 400 nm is shown. The figure shows clearly that the sizes below 100 nm perform best in terms of integrated absorption efficiency in all three systems (Figure 4.10a). To quantify the integrated absorption enhancement an alloy provides compared to both its neat constituents we introduced an enhancement factor, EF (Figure 4.10b). Here we can see that in AuAg and AuPd alloys for almost all particle sizes an alloy performs better than the neat metals. However, in case of PtPd, for particle sizes larger than 80 nm, Pd always exhibits the largest absorption, albeit, only for a few percent. For convenience I plot the EF referenced with each

of the two alloy constituents, respectively, since this representation reveals which of the constituent metals “benefits” more upon alloying in terms of increasing the absorption efficiency. In the case of AuPd it becomes obvious that the absorption of Au is enhanced much more upon alloying with Pd than the absorption of Pd upon alloying with Au. To summarize the shown behavior, where an alloy in most cases outperforms its pure constituents, I plotted the alloy with the highest integrated absorption efficiency for each particle size (Figure 4.10c). Here it becomes clear which alloy composition is needed for each size to maximize the absorption of light or even which alloy that should be chosen to minimize absorption and thus maximize scattering.

In future studies the microshutter device developed in **Paper V** (see section 6.2) can be used to conveniently fabricate nanostructured alloy surfaces that enable the efficient screening of alloys experimentally and, for example, correlate their absorption properties with their activity in different catalytic reactions. Specifically, the microshutter can be used in combination with physical vapor deposition to create thin films of precise thickness and with locally varying composition. By further combining it with electron beam lithography one can therefore fabricate alloy nanoparticles of different composition next to each other by subsequently evaporating multiple metal thin films which upon thermal annealing form alloy nanoparticles. We demonstrated the capabilities of the device by creating arrays with a composition gradient for three different alloys, namely AuAg, AuPd and AgPd, which we validated by energy-dispersive X-ray spectroscopy measurements in which we found excellent agreement between designed and measured composition.

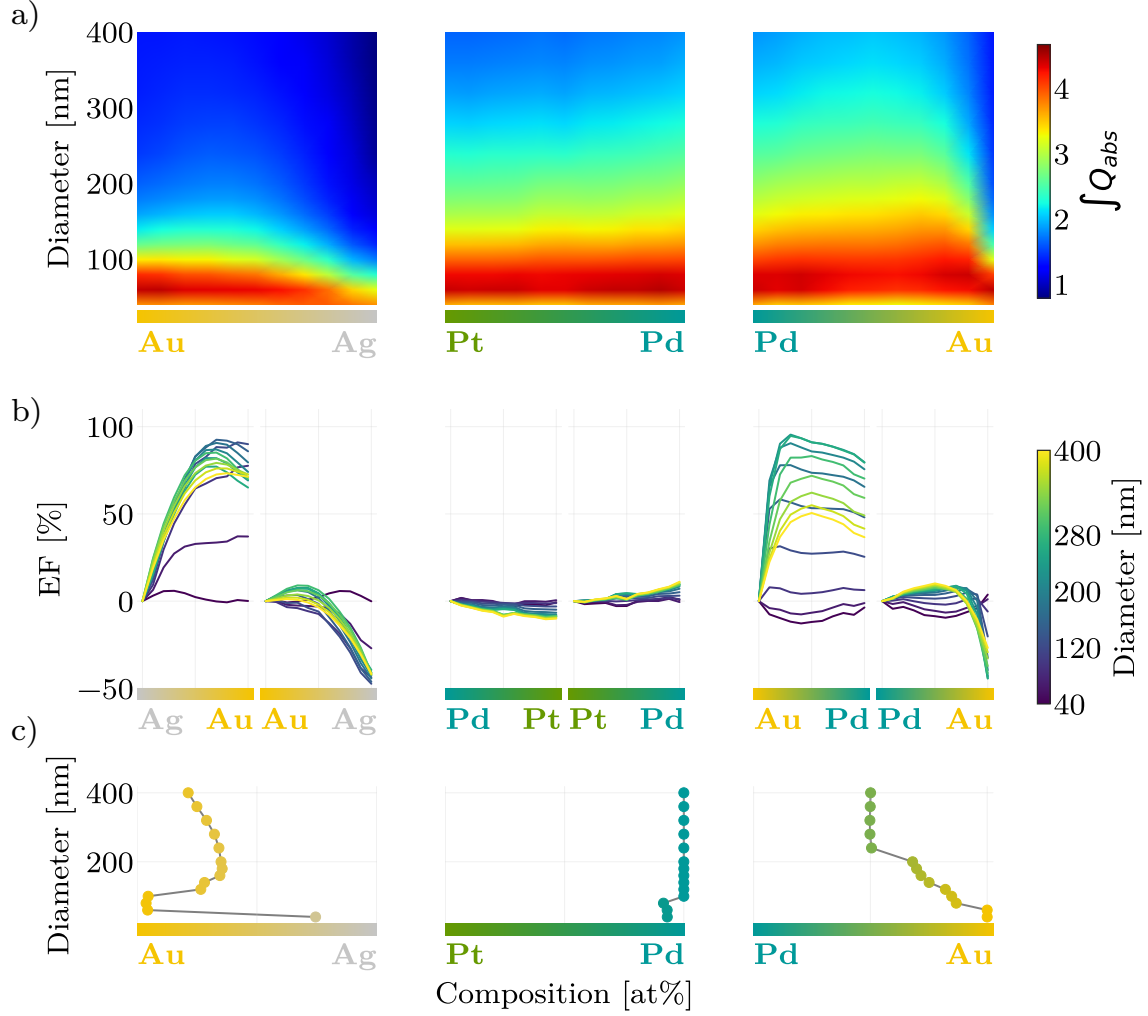


Figure 4.10: a) The calculated interpolated integrated absorption efficiency, Q_{abs} , for a single nanoparticle composed of the three different alloys AuAg, PtPd, and AuPd in the size range from 40 nm to 400 nm and across the entire compositional range in 10 at.% increments. The figure shows that the best performing sizes in terms of integrated absorption efficiency are below 100 nm for all three systems. b) The enhancement factor, EF, shows in percentage how much the integrated absorption efficiency increases, or decreases, compared to the two neat alloy constituents. It is calculated for all considered particle sizes. In the case of AgAu and AuPd a clear benefit of alloying is seen, whereas the change is negligible in the case of PtPd. For convenience, I plotted the EF referenced with each of the two constituents, respectively, since this representation reveals which of the constituent metals “benefits” more upon alloying in terms of increasing the absorption efficiency. c) Summary of the data shown in a) and b) that reveals which alloy composition that maximized integrated absorption for all calculated particle sizes.

4.5 LSPR Sensing

So far, I have discussed the origin of plasmon resonance, which effect it has on the light extinction and absorption properties of spherical and disk-shaped particles and how the dielectric function affects it. All these results already implicitly pointed at that the LSPR can be used for sensing purposes. For example, the extinction cross section is sensitive to the dielectric function of the particle itself, as can be seen in Equation 4.18. Hence, changes in the dielectric function due to change in the electronic structure of the material will be reflected in the extinction cross section of the particle, such as a shift in LSPR peak position, width, and intensity. A further obvious parameter that influences the optical cross section is the size of the particle. However, what cannot be seen in Equation 4.18 is the sensitivity of LSPR for the shape of the particle since the simple model we looked at earlier assumes spherical nanoparticles. To take shape into account, one either chooses analytical theories, such as *Gans Theory* that generalizes the Mie theory and applies also for spheroidal particles.¹³³ Specifically, the Gans theory includes the particle aspect ratio and therefore a direct dependency of the optical properties of nanoparticles on particle geometry. To investigate more complex shapes than spheroids numerical method's like FDTD must be used, as shown above.

All these mechanisms mentioned above that can be predicted with, for example, Gans theory, where a direct change of the plasmonic particle results in a change of its LSPR, can be summarized as belonging to “direct sensing schemes”. However, the resonance is also sensitive to the surrounding of a particle, which can be seen in Equation 4.18 that also includes the dielectric constant of the surrounding medium ϵ_m . Therefore, changes in the dielectric function of that medium will be reflected in the LSPR of the particle. The condition $\epsilon_r = -2\epsilon_m$ to maximize the extinction also implies that the sensitivity for sensing purpose depends on the slope of ϵ_r . If it is high, also the extinction changes upon slight changes of ϵ_m will be high. Because of all these different mechanisms that can form the basis for optical sensing, LSPR is used for molecular sensing¹³⁵, hydrogen sensing¹³⁶, pH sensing¹³⁷, biological sensing¹³⁸, to just name a few, as discussed by Mayer and Hafner.¹³³

In my work, in **Paper III**, I used the hydrogen sensing capabilities of Pd nanoparticles to measure light-absorption induced heating of such particles. As described in

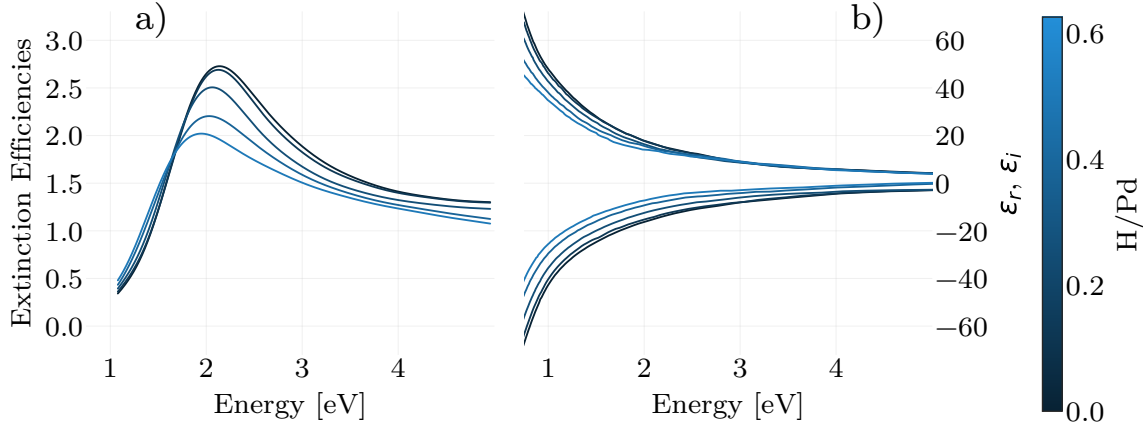


Figure 4.11: a) The extinction efficiency for Pd and Pd-hydride nanodisks with increasing hydrogen content calculated with FDTD. The LSPR peak experiences a clear shift and change in the extinction intensity. These changes are caused by the change in the dielectric function upon hydrogenation b). The dielectric function of Pd shifts closer to the x-axis for the real as well as the imaginary part with increasing hydrogen content. The dielectric functions are from Palm et al.¹³⁴

section 3.1, the hydride phase transformation of Pd leads to volume change of the Pd nanoparticles and consequent changes in their electronic structure. Hence, these changes make it possible to track the amount of absorbed hydrogen in Pd via changes of the LSPR. Specifically, the more hydrogen that is absorbed, the more the LSPR peak shifts to lower energies and the extinction efficiency decreases (Figure 4.11a). The reason is mainly that the absorbed hydrogen leads to a filling of the d-band of the Pd, as discussed in section 3.1. This leads to fewer intraband transitions, as can be seen in the narrower Drude peak of the dielectric function (Figure 4.11b). As was shown by Langhammer et al., the corresponding changes of the LSPR correlate linearly with the hydrogen content in the Pd lattice.⁹⁷ This mechanism thus forms the basis for the hydrogen nanothermometry concept I have discussed in section 3.2 and that I have used to measure absolute nanoparticle temperature upon illumination in **Paper III**.

5 Catalysis

Catalysis is one of the cornerstones of modern society. In this context, many people might only think of the three-way-catalytic converter in cars, however the technical relevance of catalysis goes far beyond this application. For instance, nowadays around 90 % of the chemical industry uses a catalytic reaction somewhere in their processes.²⁰ Examples include refining of crude oil and the production of bulk and fine chemicals.^{139–142} Among other things, the produced chemicals are used in agriculture, polymers, pigments, pharmaceuticals, and consumer products.

5.1 Heterogeneous Catalysis

Mechanistically, catalysis is the change of rates of a chemical reaction with the help of a catalyst, which itself is not consumed by the process. The two main technical reasons why catalysts are particularly important are that catalysts can increase the reaction rate towards the desired product (activity) and/or decrease the reaction rate towards an unwanted product (selectivity) of a reaction. One way of schematically depicting a catalytic reaction is with a catalytic cycle (Figure 5.1). It shows the reaction pathway including a catalyst with multiple elementary steps. It also shows that the catalyst itself is not consumed during the reaction.

In catalysis, one normally differentiates between homogeneous and heterogeneous catalysis. In homogeneous catalysis the catalyst is in the same phase as the reactants. A famous example is the creation of the *ozone hole* in the 80s.²⁰ Here chlorine functioned as catalyst and increased the rate of



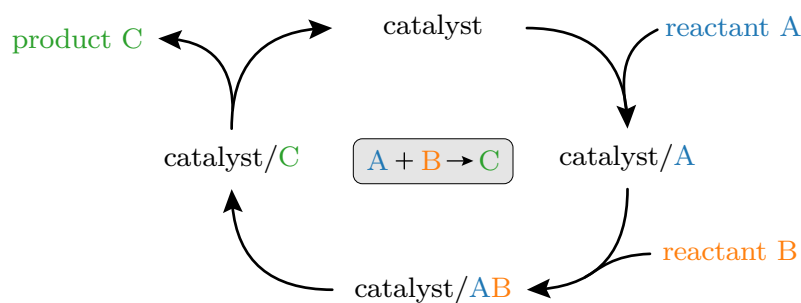


Figure 5.1: Schematic of a catalytic cycle forming the product C out of reactants A and B with help of a catalyst. The reaction occurs via multiple elementary steps and the catalyst itself will not be consumed during the reaction.

In this thesis, heterogeneous catalysis, where the catalyst is in a different phase (typically in the solid state) than the reactants and products, has been used. This means that the reactions occur on a surface. Heterogeneous catalysis is considered the workhorse of the chemical and petrochemical industry.²⁰ One famous example is the catalytic ammonia synthesis over iron-based catalyst. Another example for heterogeneous catalysis is the catalytic oxidation of carbon monoxide over noble metals like Pd, Pt, or rhodium (Rh). This reaction is, for example, used in car exhaust catalysts and will be discussed in more detail in section 5.3.

To illustrate how a catalyst works in general, it is useful to have a look at the potential energy diagram of a reaction. In Figure 5.2 this is shown for the arbitrary reaction $A + B \rightarrow C$. It illustrates that the catalyst offers an alternative reaction pathway, normally with several steps that are energetically favorable compared to the uncatalyzed reaction. To this end, it is also important to note that a catalyst only changes the kinetics of a reaction and not the thermodynamics.²⁰

A guiding principle in catalysis is the *Sabatier's principle*.¹⁴³ It relates to the fact that if the interaction between catalyst and reactants is too weak, they will not bind to the catalyst and the catalytic reaction cannot happen. On the other hand, upon too strong reactant-catalyst interaction, the entire surface will be covered at all times, not leaving any free sites for the other reactant to bind and react. This phenomenon is known as poisoning. The same problem applies to the product. If it binds too strongly on the surface it will not desorb and not free active sites for the reaction to

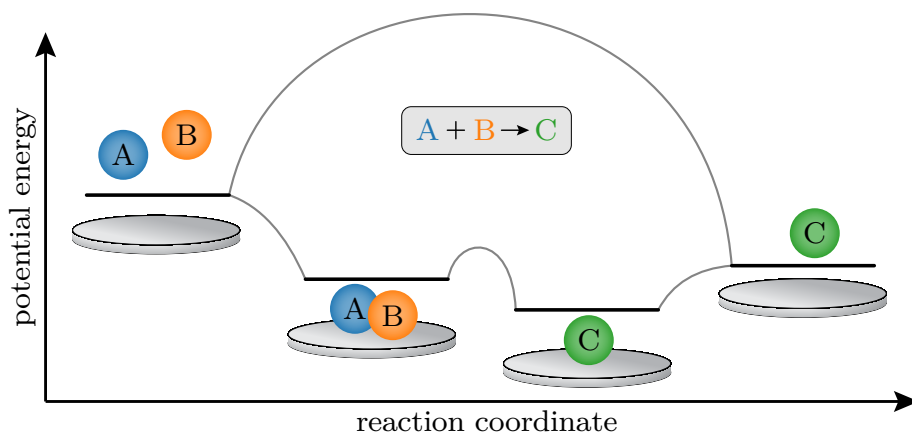


Figure 5.2: The potential energy diagram of a chemical reaction $A + B \rightarrow C$ in the presence and absence of a heterogeneous catalyst. By adding a catalyst, the potential energy landscape changes and allows for a different reaction pathway. Adapted from Chorkendorff and Niemantsverdriet.²⁰

continue. This balance, and on which side a catalyst is located for a specific reaction, can be depicted as a *volcano plot* as shown in Figure 5.3, where the ideal catalyst would be located at the top.

When it comes to catalyst materials, it is not just single elements that are used but also alloys are becoming increasingly important, as they become more and more available in nanoparticle form.^{145–147} In catalysis, alloying can be regarded as an additional handle for tailoring activity or selectivity of the catalyst. To give one example, AuPd alloys are used for the vinyl acetate synthesis, since they show superior activity compared to the classic monometallic catalyst Pd.¹⁴⁸

Mechanistically, there are two kinds of effects that alloying can impose on catalyst function.⁶⁰ The first is that due to the alloying the electronic structure of the catalyst changes. This means that chemical properties of the material and bond strengths of the adsorbates will change, and therefore the overall reactivity.¹⁴⁹ This effect is usually referred to as *ligand effect*.

The second effect is the *ensemble* or *geometric effect*. Due to the alloying the amount of identical multiple surface absorption sites decreases and single-atom site abundance increases, which in turn modifies chemisorption and therefore the reaction properties

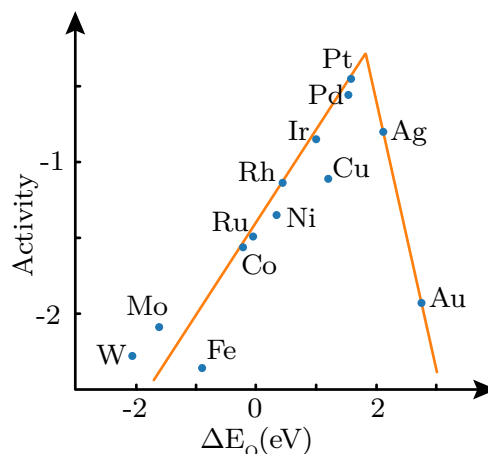


Figure 5.3: A classic volcano plot showing the activity of the oxygen reduction reaction depending on the oxygen binding energy for different metal catalyst materials. To increase the oxygen reduction rate is a crucial step to improve low temperature fuel cells. Adapted from Nørskov et al.¹⁴⁴

of the adsorbates.⁶⁰ For example, catalytic reactions that require large assemblies of active sites will be effectively suppressed.¹⁴⁹

It should be highlighted that the composition on the surface of an alloy catalyst is seldomly equal to the bulk composition and may dynamically change during the reaction (see section 2.2). Due to such effects, surface alloys can emerge that would not exist in bulk.¹⁵⁰ Because catalysis normally happens at elevated pressures other parameters than surface energy can be the controlling factor. If, for example, one of the components interacts strongly with one of the reactants, it could influence the surface composition of the alloy severely.⁵⁵

5.2 Plasmon Mediated Catalysis

Plasmon mediated catalysis is a sub-area of photocatalysis, where metal plasmonic nanostructures are employed to capture light and concentrate the corresponding energy at the nanoscale, where it is anticipated to impact catalytic reactions.^{151,152}

For simplicity, I use the term “photocatalysis” below as a general term for plasmon mediated catalysis.

The field is divided into two sub-areas, namely direct and indirect photocatalysis.¹⁵¹ The indirect route refers to systems that combine plasmonic nanostructures with semiconductors. In this scheme, the LSPR captures energy from the light, which is then transferred to the semiconductor where the catalytic process occurs. A famous example is the plasmon-enhanced water splitting reaction on TiO_2 using plasmonic Au nanoparticles to produce hydrogen.¹⁵³ In contrast, in the direct scheme, the plasmonically active material acts as energy capturer and catalyst at the same time, as demonstrated in the seminal work by Christopher et al. for the ethylene epoxidation reaction over Ag nanocrystals.²⁶ As the direct scheme is a promising route in catalysis, I investigated the light absorption behavior for ten different late transition metal alloys in **Paper IV**, with the aim to investigate whether alloying may constitute a new route to increase the amount of absorbed energy by the nanoparticles upon illumination.

To provide some understanding for the energy flow in a plasmonic nanostructure after excitation of the LSPR, it is useful to discuss the involved processes. The first step is to excite the LSPR by irradiating light at the resonance frequency of the nanostructure at hand (Figure 5.4a). Once excited, the plasmon has two ways to decay, either radiatively by re-emitting a photon or nonradiatively by Landau damping.¹⁵¹ Landau damping creates hot charge carriers (Figure 5.4b). The term “hot” indicates that the excitation energies are higher than the thermally excited equivalent at room temperature. The resulting energy distribution depends on particle size,¹⁵⁴ plasmon energy, and material (electronic structure).¹⁵⁵ The time scale for Landau damping is below 100 fs.¹⁵⁶ After the hot carriers are created, they will relax and redistribute their energy via electron-electron scattering (Figure 5.4c). This happens at a time scale of around 0.1 ps to 1 ps.¹⁵² These lower energy electrons, sometimes called warm electrons, can now interact with phonons and lead to increased particle temperatures, which will also dissipate to the surroundings, such as the support (Figure 5.4d). This happens in a range of 100 ps to 10 ns.

In principle, all these effects can contribute to catalysis by either increasing the rate or changing the selectivity of a reaction. The hot charge carriers can, for example, excite

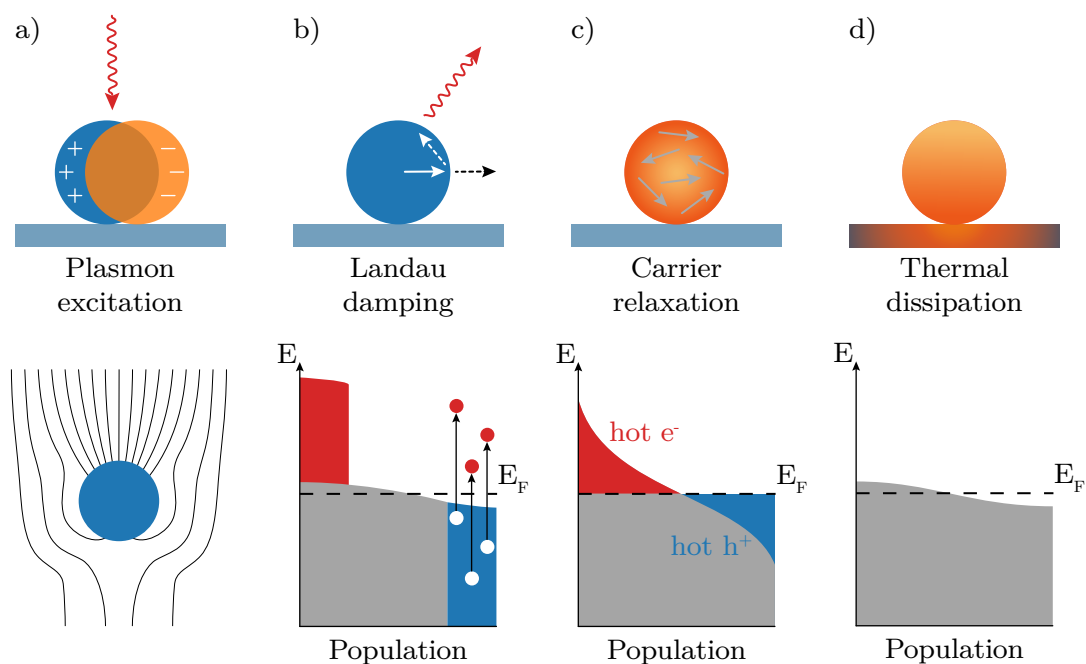


Figure 5.4: a) Initially, the LSPR is excited in a nanostructure by irradiating light at the resonance frequency. b) The plasmon can decay either radiatively by re-emitting a photon or non-radiatively by Landau damping, which creates hot charge carriers. c) The hot carriers will relax and redistribute their energy via electron-electron scattering. d) The lower energy charge carriers can now interact with phonons and lead to increased temperature, which will also dissipate to the surroundings, such as the support. Adapted from Brongersma et al.¹⁵²

electronic or vibrational transitions in adsorbed molecules or can occupy a specific molecular orbital and induce desorption, dissociation, or translational motion.¹⁵² Mukherjee et al.²⁷ showed for example the dissociation of H_2 at room temperature over Au particles using a laser in the visible range. Here, the hot electron transfer from the Au nanoparticle into an antibonding orbital of the H_2 molecule is believed to trigger the dissociation.

Alternatively, it has also been reported that the plasmonic field enhancement or the localized heating effect can help to drive the reaction.¹⁵¹ In the field-enhancement mechanism, a plasmonic particle acts as an optical antenna that captures the light and creates an enhanced near-field and a catalytic particle that is placed inside that

near-field experiences more photons per volume, which may lead to increased activity of the catalyst due to, for example, increased photoexcitation.^{157,158} A photochemical rate enhancement due to near-field enhancement is expected to be proportional to the rate of incident photons.³⁷ Temperature induced reaction rate enhancement on the other hand works because chemical reactions, to be exact the rate constant, k , typically obey the Arrhenius equation

$$k = A \exp\left(\frac{-E_a}{RT}\right). \quad (5.2)$$

T is the temperature, E_a is the activation energy, R is the gas constant, and A is the pre-exponential factor. Important to note is that this equation only works in the kinetically limited regime and not if the reaction is limited by mass transport.

Despite almost a decade since the first papers in the field were published, there is (still – or maybe even more of) a controversy about the dominant reaction enhancing mechanism in plasmon mediated catalysis.¹⁵⁹ This important discussion is essentially centered on the problem that it is very difficult to unambiguously distinguish between direct influence of the energetic charge carriers²⁷ and pure thermal effects.²⁹ In some cases, the findings can be explained either way, as was shown by Sivan et al.²⁹ and even more recently by Baffou et al.³⁷

One of the core problems is that the *exact* temperature of the small catalyst nanoparticles is very hard to determine (see section 3.2). In fact, in catalysis the catalyst temperature is either not known or largely underestimated, as discussed by Sivan et al.²⁹ This arises from the difficulty to precisely measure the temperature of the small catalyst particles or even active sites since most techniques measure the *average* temperature of the sample or require an elaborated experimental setup. Another argument why direct hot-charge-carrier effects are probably less common than claimed is the very short lifetime of these carriers. It makes the probability of interaction with the surroundings very low.³⁷ To help disentangle these effects, we introduced the optical hydrogen nanothermometry method to measure nanoparticle temperature in **Paper III**, as already discussed in section 3.2.

5.3 CO Oxidation

Carbon monoxide is a toxic gas at concentrations above 200 ppm.¹⁶⁰ At the same time, it is not possible for humans to detect it because it is colorless, tasteless, and odorless. The toxicity for humans and animals is based on CO's ability to bind to hemoglobin. This reduces the ability of the blood to carry oxygen.¹⁶¹ Depending on the concentrations and time of exposure it leads to headache, vomiting, dizziness, chest pain, passing out and death.¹⁶² Due to the high toxicity of CO, the abatement and reduction of it is used in car-catalysts but also in respirators, for, for example, firefighters.¹⁶³

The main source of CO is the partial combustion of fuels. One to two percent of a car's exhaust is carbon monoxide. Because we have a lot of cars in our society, they are the biggest producers of CO. In cities, transport is responsible for up to 90 %¹⁶⁴ of the CO emissions. To reduce the emission, today, three-way catalytic converters are found in essentially all gasoline vehicles.

Another area where CO removal is important is in proton exchange membrane fuel cells.¹⁶⁵ Specifically, it is critical to reduce the CO content of the hydrogen fuel to less than 50 ppm since CO poisoning of the Pt catalyst otherwise dramatically reduces the fuel cell efficiency.¹⁶⁴

To this end, there are three ways to remove CO from a gas stream: (i) absorption, (ii) methanation and (iii) catalytic oxidation.¹⁶⁴ Since catalytic oxidation of carbon monoxide to carbon dioxide is the most effective one, we will have a closer look at that. For catalytic CO oxidation, different catalysts are used and the noble metals like Pd, Pt, or Rh, which have high activity and have been used for a long time.¹⁶⁶ Due to the limited availability and the cost of noble metals, however, oxides of less scarce metals are of high interest, such as for instance Fe, Cu, Ni, Co.^{164,167,168} Also explored are Au nanoparticles for low temperature CO oxidation.¹⁶⁹ Due to the low temperature capability they are often used in breathing apparatus and air purification.¹⁶⁴ The focus in this thesis is, however, CO oxidation on noble metals like Pd.

The catalytic CO oxidation on noble metals, such as Pt and Pd, is a classical example of *Langmuir–Hinshelwood* kinetics.²⁰ Here, all reactants first adsorb on the surface,

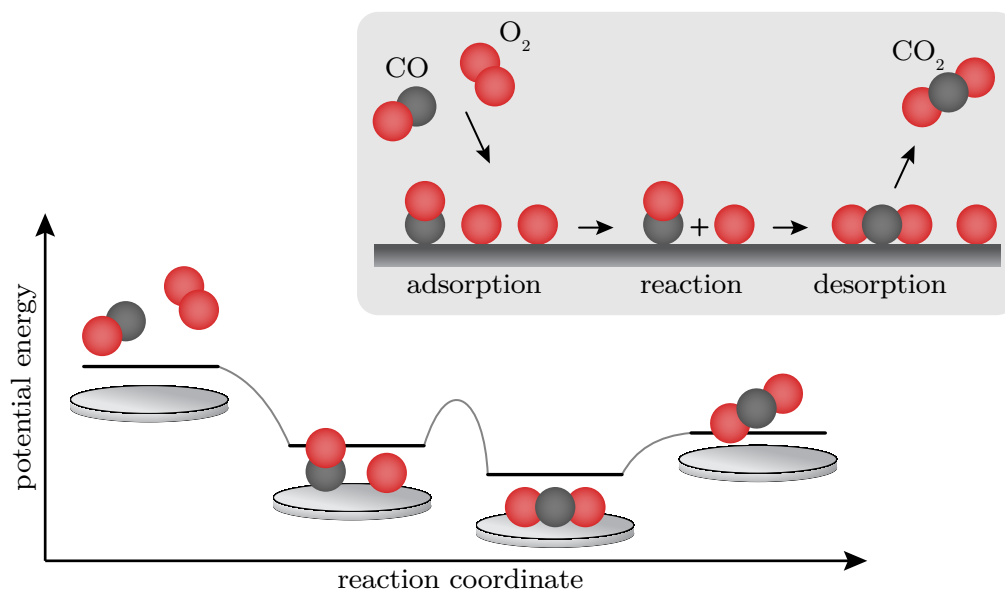


Figure 5.5: The reaction cycle and the potential energy diagram of CO oxidation. At first, CO and O₂ are adsorbed on the catalyst surface and O₂ will be dissociated in the process. A single oxygen atom and a CO molecule will then form a CO₂ molecule on the surface. The last step is for the CO₂ molecule to desorb. Adapted from Chorkendorff and Niemantsverdriet.²⁰

then undergo reaction and finally desorb from the surface (Figure 5.5), as was first proposed for Pt by Langmuir and later confirmed for Pd.^{170,171} The corresponding elementary steps can be written as follows.¹⁷²



The * symbolizes free sites and $k^{+/-}$ represent the forward and backward rate constants, respectively. Step 5.5 is often considered to be the rate determining step

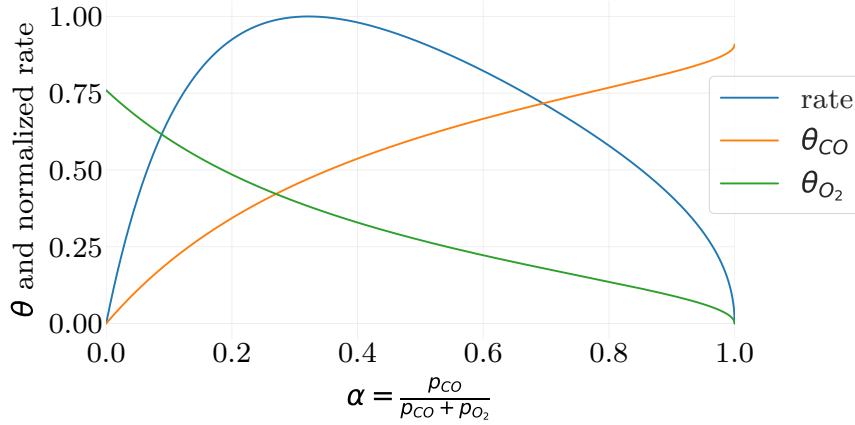


Figure 5.6: The calculated rate and surface coverage, θ , of CO and O₂ on a surface during CO oxidation for different CO and O₂ mixing ratios α_{CO} . The rate constants for CO and O₂ ad- and desorption and CO₂ formation are chosen arbitrarily to be ten and only serve the purpose to illustrate the behavior of a reaction following Langmuir-Hinshelwood kinetics. It can clearly be seen that the rate reaches a maximum and is reduced to the sides, where high relative concentrations of CO or O₂, respectively, cover the surface and poison it. The coverage and rate were calculated using arbitrary rate constant values representing a Langmuir-Hinshelwood reaction.²⁰

(RDS).²⁰ This is also depicted in Figure 5.5 because the energy barrier for this step is the highest among the forward reactions. Considering the RDS, the rate for the reaction follows as

$$r = k_3^+ \theta_{\text{CO}} \theta_{\text{O}} . \quad (5.7)$$

Here θ_x describes the coverage of CO and O₂ on the surface. The reaction rate can be plotted depending on the relative partial pressure, α , of CO and O₂ for constant temperature (Figure 5.6). At high O₂ pressure the surface is mostly covered with oxygen and only few CO molecules can adsorb and react, resulting in a low reaction rate. The surface is oxygen poisoned. Similarly, at high CO concentrations, the reaction rate is low due to CO poisoning.²⁰ In the range in-between, the coverage of O and CO is more balanced and therefore reaction between them can occur. In this

range, the rate reaches its maximum. The shape of the rate curve is governed by the rate constants for CO and O₂ ad- and desorption and the formation of CO₂. Thus, depending on total pressure, temperature, catalyst material and state, the shape of the rate curve will change.

As already mentioned, classical catalysts with high activity for CO oxidation are the noble metals Pt, Pd, and Rh.^{164,173} More recently, also small Au nanoparticles were discovered to work for CO oxidation at low temperatures.¹⁶⁹ Therefore, the step to investigate AuPd alloys appears natural. However, even though AuPd alloys are an excellent catalyst for, for example, the hydrodesulfurization reaction¹⁷⁴ or the direct synthesis of hydrogen peroxide from H₂ and O₂,¹⁷⁵ they are not very efficient for the conventional catalytic CO oxidation reaction.¹⁷⁶

The to date unexplored route of alloying plasmonically active Au with Pd in the context of plasmon-mediated catalysis is explored in **Paper II**. It is used to shine light on the discussion of the reaction enhancing mechanism when noble metal catalyst nanoparticles are irradiated with visible light during a catalytic reaction. By alloying Pd with Au, we tailor the catalytic activity in the dark (i.e., without light irradiation), while, at the same time, maintaining a more-or less constant optical cross section. By comparing the neat Pd and alloy systems in terms of their activities under illumination, we highlight the fact that the catalytic activity is not solely governed by the photon flux but also depends heavily on the temperature in the dark, as expected in the kinetically limited regime (see Equation 5.2). A fact that – unfortunately – commonly plays a minor role in the debate about enhancing mechanisms in plasmon-mediated catalysis.

6 Nanofabrication

Our modern life depends more and more on technology on the nanoscale, where not just our computers and mobile phones are in the need of nanoscale transistors but almost every electronic device has some components which are scaled down to the nanoscale regime. Likewise in medicine,¹⁷⁷ the food industry,¹⁷⁸ water treatment,¹⁷⁹ biotechnology,¹⁸⁰ solar energy conversion¹⁸¹ nanosized systems become increasingly important, and, as we already have seen, in the chemical industry nanoparticles are widely used as catalysts. Hence, methods to produce such nanomaterials and systems are increasingly more important and, in my work, I have used simple but effective nanolithography-based methods to produce large arrays of metal and alloy nanoparticles that I will summarize in this chapter.

6.1 Hole–Mask Colloidal Lithography

Most of my samples were nanofabricated with a technique called *Hole–Mask Colloidal Lithography* (HCL).¹⁸² This technique offers the opportunity to make large area arrays of nano-objects like disks and dimers, as well as layered structures in terms of their composition. Furthermore, samples can be fabricated on a variety of surfaces, like fused silica, silicon, or sapphire. The technique falls into the area of self-assembled nanofabrication, which has the advantage that it easily can produce nanostructures in the sub-100-nanometer range. At the same time, the technique is scalable to large areas and comparably cost-effective.¹⁸³

The process for HCL is shown in Figure 6.1 and works as follows. After choosing a substrate (Figure 6.1a) it needs to be cleaned thoroughly. This is done by sonication in acetone and IPA (isopropyl alcohol). After cleaning, a thin PMMA (polymethyl methacrylate) sacrificial layer is spin-coated onto the substrate (Figure 6.1b). After

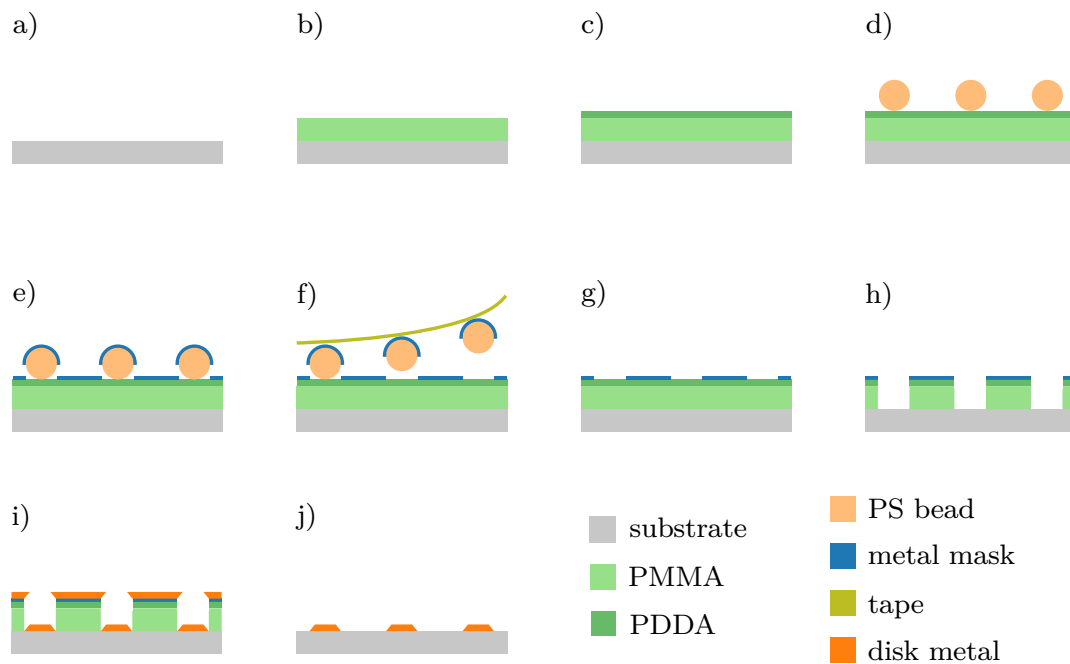


Figure 6.1: The process of creating a nanodisk array on a surface with hole-mask colloidal lithography. Using a) cleaned substrate, b) spin-coat PMMA, c) disperse PDDA, d) disperse PS, e) evaporate mask, f) tape-strip, g) holes in mask, h) plasma etching PMMA, i) evaporate metal, j) lift-off.

the spincoating the sample is plasma treated to increase the hydrophilicity of the PMMA. This makes it possible in the next step to dispense a polyelectrolyte solution of PDDA (Polydiallyldimethylammonium chloride) on the surface (Figure 6.1c). This creates a positively charged layer on top of the PMMA. Subsequently, a solution with negatively charged polystyrene (PS) beads is dispersed on the sample (Figure 6.1d). The PS beads, due to electrostatic interactions, are thereby assembling themselves on the surface in a quasi-random array without long-range order. The average center-to-center distance between particles can be tuned by screening the charge of the PS beads by adding tiny amounts of salt to the solution. After removing the excess beads by extensive rinsing in water and subsequent blow-drying a layer of chromium is evaporated onto the self-assembled PS beads (Figure 6.1e). After evaporation, the PS beads are removed by tape stripping (Figure 6.1f), which leaves holes with the diameter dictated by the PS beads in the Cr mask (Figure 6.1g). Then, by applying an oxygen plasma etch, the PMMA layer exposed through the holes can be etched

away, leaving deep holes in the PMMA layer that extend all the way to the substrate (Figure 6.1h). After this step, the mask is ready to be used for evaporation of the metal (or other material) of choice. Depending on how the metal is deposited, one can create different nanostructures by using tilting and rotation of the substrate during evaporation.¹⁸⁴ To create nanodisks, as I have used in my work, the metal must be deposited at normal incidence (Figure 6.1i). Different ways to deposit material through the mask will be discussed in the next section. The last step is the lift-off process (Figure 6.1j). Here acetone is used to dissolve the underlying PMMA layer to remove the mask. As the last step, the sample is rinsed with IPA and blow-dried with N₂.

The until now described HCL method results in a mask which easily fabricates large area samples with quasi-random structures of the same size and geometry that are of great use in ensemble measurements. However, to be able to observe nanoparticles on the single particle level, as we have done on **Paper V**, these sample are not optimal since the particle density is too high. Furthermore, in single particle experiments, one often desires to study particles with varied sizes and geometries at the same time, to create correlation between their optical response and their individual properties. Therefore, such samples require particles with different sizes and geometries placed next to each other and separated at an appropriate distance. To create such samples electron beam lithography (EBL) is the method of choice.¹⁸³ This technique allows creating samples with, for example, rows of particles with increasing sizes or changing geometry.

6.2 Material Deposition

The mask can be used to create single-material or alloy nanostructures of different type. For alloys, the alloy constituents are consecutively evaporated through the mask. Technically, there are many ways to grow a thin film on a surface. In general, thin film deposition methods can be divided into two categories, physical and chemical deposition. Chemical processes include for example wet-chemical methods or chemical vapor deposition, like atomic layer deposition. Physical processes on the other hand do not rely on a chemical reaction to form the thin solid film. Instead,

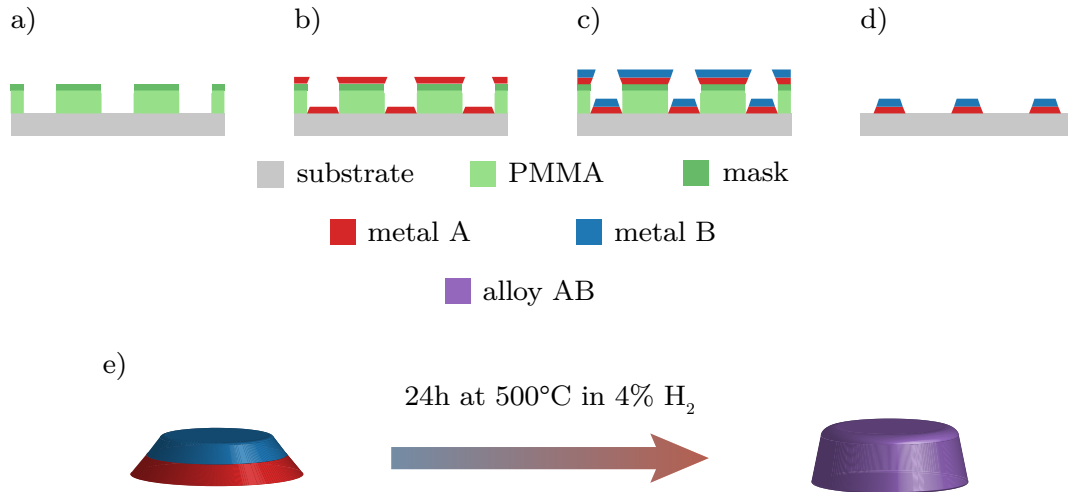


Figure 6.2: The process of creating an alloy nanodisk array on a surface. The method uses a) a HCL-created mask. b) Through the mask metal A is evaporated and c) subsequently the second metal B. d) During the lift-off the mask is removed and leaves behind the bare layered metal particles on the substrate. e) To create the alloy, the layered structures will be annealed at 500°C to provide the atomic mobility necessary to induce alloy formation in the solid state. During this process, the nanoparticles will slightly change their dimensions and shape, with the specifics depending on the metal-substrate interaction.

they use means like thermal evaporation or sputtering. Evaporation methods rely on the concept of evaporating a solid material by heating it to very high temperature and the vapor then condensing on the substrate, where it nucleates and grows into a thin film. For these techniques, ultra-high vacuum (UHV) is needed to enable the necessary long mean free path for the vapor to reach the substrate. The evaporation itself can be induced by various means. The target material can, for example, be heated with a high-voltage electron beam that is rastered over a source material (electron beam evaporation) or lasers can be used to heat the material (laser beam evaporation).

The process of nanofabricating alloy nanodisks uses a mask created either by HCL (Figure 6.2a) or EBL. Through the mask, the first metal is evaporated (Figure 6.2b) and subsequently the second metal (Figure 6.2c), where the respective thickness of

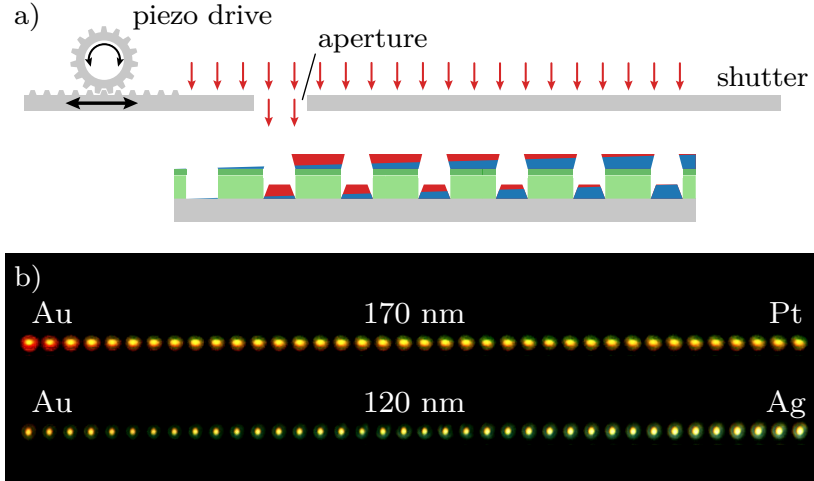


Figure 6.3: a) The microshutter allows evaporation of different metals with different thicknesses next to each other to ultimately form different alloys. This is achieved by moving a micro-aperture with a piezo drive across the surface during the evaporation, with different speeds resulting in different thicknesses. This ultimately results in a row of alloy nanoparticles with different composition if the shutter is moved across a pre-defined evaporation mask defining the particles. b) Two rows of particles obtained in this way after thermal annealing viewed in a dark field microscope and revealing beautifully the different compositions of the alloys reflected in their different colors (scattering). The upper row are disks with a diameter of 170 nm ranging from pure Au (left, red/orange) to pure Pt (right, yellow). The lower row are disks with a diameter of only 120 nm ranging from pure Au (left, orange/yellow) to pure Ag (right, green).

these two layers dictates the final composition of the alloy. For all alloy nanofabrication in **Paper I, II, and IV**, I used electron-beam evaporation of the constituent metals. The last step is the lift-off process (Figure 6.2d), which then yields layered nanodisks on the substrate. To create an alloy from this layered structure, one needs to anneal the system to induce the necessary atomic mobility in the solid state, which was done at 500 °C for 24 h in 4 % H₂.

Together with the microshutter introduced above (Figure 6.3) and discussed in **Paper V**, using EBL not only enables the nanofabrication of samples with systematically varied sizes and geometries next to each other but also to accurately control alloy com-

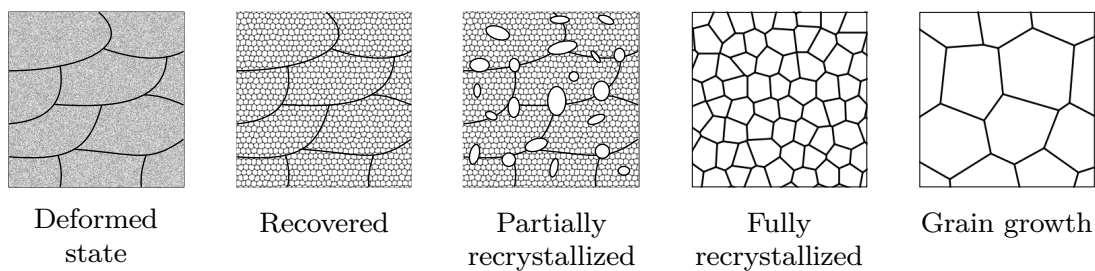


Figure 6.4: Schematic illustration of the recovery, recrystallization and grain growth steps during annealing. Adopted from Raabe.⁵⁷

position with single nanoparticle resolution. Specifically, by moving a shutter with a $20\text{ }\mu\text{m}$ small aperture with a piezo drive over a mask with a row of EBL-defined holes, one can evaporate different thickness of multiple materials and ultimately create nanoparticles comprised of different alloys next to each other (Figure 6.3a). Under a dark field microscope one can then nicely see that alloy particles with different compositions scatter light in different colors (Figure 6.3b). In the longer term, I hope that this technique can be used to, for example, efficiently screen different alloy compositions for application in sensors or as catalysts in different chemical reactions.^{185,186}

6.3 Annealing

The last step in the nanofabrication of alloy nanoparticles is annealing. In fact, this can be an important step not only when nanofabricating alloys but also when targeting single element nanoparticles to, for example, control their morphology.¹⁸⁷ In case of the alloy nanostructures at hand, it is necessary to provide the required atomic mobility to induce alloy formation from the layered constituents in the solid state (Figure 6.2).

From a classical metallurgy perspective, the annealing process can be divided into three major steps: (i) recovery, (ii) recrystallization and (iii) grain growth (Figure 6.4).⁵⁷ During the first recovery step, dislocations and other defects show minor movement and rearrangement. This slightly decreases their density and more importantly it reduces the associated stress in the material.⁵⁷ Recrystallization happens if

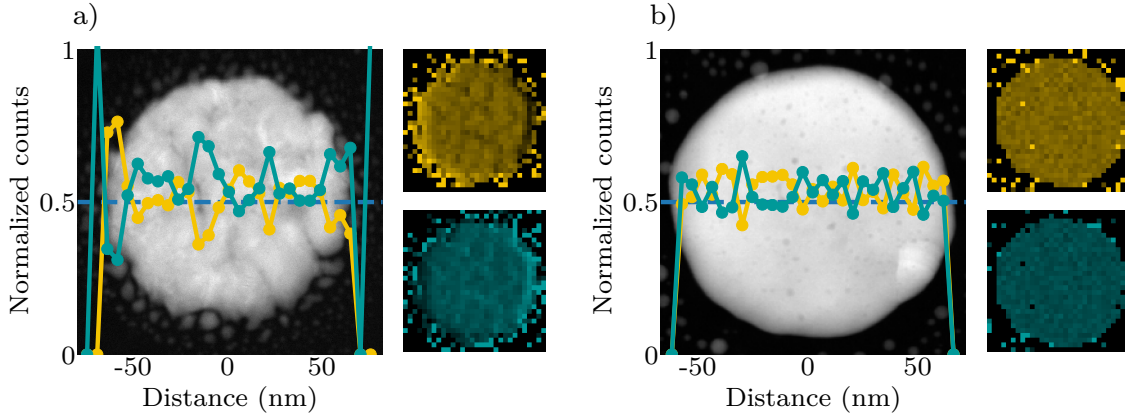


Figure 6.5: A high-angle annular dark field scanning transmission electron microscopy (HAADF-STEM) image of an a) unannealed and an b) annealed AuPd particle. The corresponding energy dispersive X-ray spectroscopy (EDX) images show the lateral distribution of Au (yellow) and Pd (green). The HAADF-STEM images reveal a strong reduction of grains during the annealing process. The line scan further confirms the homogeneous distribution of both elements across the particle after annealing. Data of the annealed particle taken from Rahm et al.¹¹²

the temperature reaches around $1/3$ to $1/2$ of the melting point of the material.⁵⁷ During this phase, new and strain free grain boundaries are formed, and high angle grain boundaries are reduced. Also, the defect density reduces drastically. The last stage is the grain growth, where the new grains with low angle grain boundaries that formed during the recrystallization step continue to grow, thereby reducing the overall grain boundary length and thus the free energy of the system.⁵⁷ Projected onto my nanodisk structures, given enough time and high enough temperature, they will transform into a single crystal (Figure 6.5).

7 Setup/Characterization

In this chapter, I will describe the setup I used for the catalysis measurements included in **Paper II** and the hydrogen nanothermometry in **Paper III**. Furthermore, I will explain the different material characterization techniques that were used to characterize the samples of all papers.

7.1 Catalytic Flow Reactor Measurement Setup

The setup for the catalysis and hydrogen nanothermometry experiments is a plug-flow type reactor with a custom-made pocket reactor inserted in the large quartz tube (Figure 7.1). The gas inlet is connected to ten mass flow controllers with a range of 10 mL/min to 1500 mL/min that can individually be combined to provide the desired gas mixtures and flow rates. The flow reactor can be heated with a heating coil to around 600 °C.

The sample itself is placed inside a “pocket reactor” (inset Figure 7.1). It consists of a rectangular glass pocket with optically flat “windows” (10 mm x 23 mm) connected to a round glass capillary with an inner diameter of 1 mm. The pocket reactor ensures that dilution of reaction products is minimized and enables in this way the use of small amounts of catalyst material in combination with mass spectrometry in general, and the use of nanofabricated samples as described in chapter 6. The pocket reactor itself is positioned in the down-stream-end of the flow reactor tube, such that the incoming gas mixture can be preheated. The quadrupole mass spectrometer (QMS) is a differentially pumped system with a measurement range of 1 u to 200 u.

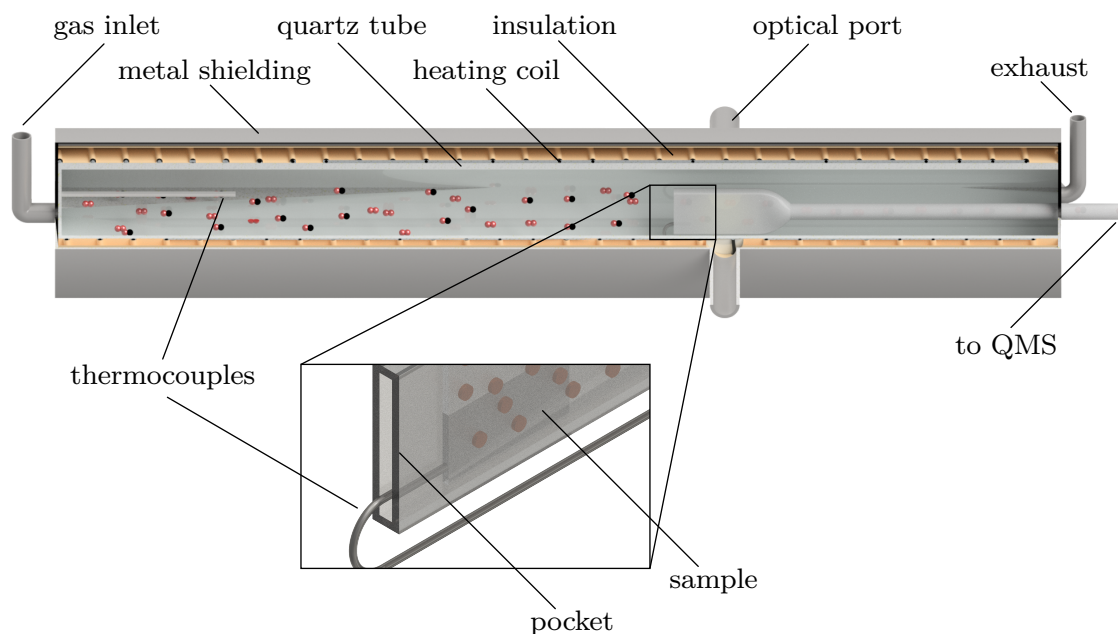


Figure 7.1: The plug flow reactor is an insulated quartz tube that can be heated via a resistive heating coil. It has an optical port that enables illumination for photocatalysis and optical transmittance spectroscopy measurements on each side. The gas inlet is controlled by an array of mass-flow controllers, which can be used to control the desired gas mixture and flow rate. A glass pocket reactor is mounted inside the quartz tube, which hosts the sample. The outlet of the pocket is directly connected to a QMS system. To mount the sample this way ensures that dilution of reaction products is minimized. To control and monitor the temperature of the system, two insulated thermocouples are placed inside the reactor, one to monitor the reactor and the other one to monitor the sample temperature.

Two K-type thermocouples are inserted in the reactor. One is positioned 10 cm downstream of the gas inlet and the other one is located at the entry of the pocket reactor, where it touches the sample inside the pocket from the side, to accurately measure sample temperature.

The flow reactor itself has an optical port perpendicular to the flow direction, which can be used for optical transmission measurements via a fiber coupled spectrometer with 200 nm to 1100 nm spectral range, as well as for illumination in photocatalysis

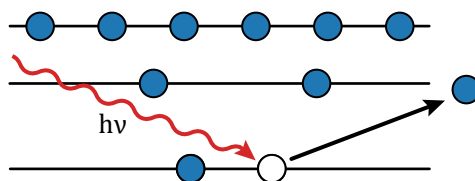


Figure 7.2: The principle of X-ray photoelectron spectroscopy: an incoming X-ray photon kicks out an electron from an inner shell, which is measured by an electron detector. This electron carries information about the elemental composition of the probed surface, as well as about the chemical state of the surface atoms.

experiments by a high-power light source. To this end, the first option is a 250 W quartz tungsten halogen lamp with a high irradiance in the visible and near-infrared spectral range (Osram 64657 HLX lamp in a Newport 67011 housing) and the second option is a 1000 W mercury xenon arc light source that has high irradiance from the middle-ultraviolet to the near-infrared (Newport 6295NS in a 66921 housing). This mercury xenon arc lamp is also equipped with a liquid IR filter that features high transmission in the 250 nm to 950 nm range.¹⁸⁸ Both lamps are further equipped with a condenser lens to ensure a homogeneous illumination of the sample. In **Paper II** and **III**, I have used the mercury xenon arc light.

7.2 X-ray Photoelectron Spectroscopy

X-ray Photoelectron Spectroscopy (XPS) is a surface sensitive technique that provides information about the chemical state of the surface and enables semi-quantitative analysis of the composition of the sample.¹⁸⁹ Because it gives information about the chemical state of a material it is also called *electron spectroscopy for chemical analysis* (ESCA).¹⁹⁰ The basic principle of XPS is that the energetic X-rays kick out core electrons of an atom (Figure 7.2), which then can be measured in an electron energy analyzer to draw conclusions about the sample by using a reference library of XPS spectra. The surface sensitivity of XPS arises from the fact that only electrons

ejected in the first nanometers from the surface can be measured because that is the mean free path of low energy electrons in matter.¹⁹¹

Specifically, what is measured in an XPS experiment is the kinetic energy of the electron emitted by the material. To then derive the binding energy of the electron one must consider which pathway the electron takes energetically. The electron gets kicked out by a photon with energy, $h\nu$. It must overcome the binding energy, E_B , and the work function of the sample, Φ_S . This can be written as

$$h\nu = E_B + \Phi_S + E_{kin,S} . \quad (7.1)$$

In Figure 7.3 it can be seen that the equilibrium of the Fermi levels leads to a situation where

$$E_{kin,S} + \Phi_S = E_{kin,XPS} + \Phi_{XPS} . \quad (7.2)$$

Therefore, Equation 7.1 can be written as

$$h\nu = E_B + \Phi_{XPS} + E_{kin,XPS} . \quad (7.3)$$

This in turn leads to the well-known equation for the binding energy

$$E_B = h\nu - \Phi_{XPS} - E_{kin,XPS} . \quad (7.4)$$

The instrument itself is composed of an X-ray source, a monochromator, a sample holder and the electron energy analyzer. The whole system is under UHV to ensure a long mean free path for the electrons on the way from the sample surface to the analyzer.

The X-rays are in most cases generated by accelerating electrons onto a metal target. This leads among others to Bremsstrahlung and characteristic emission lines like the K_α -line.¹⁹² These lines are generated by the incoming electron knocking out an electron from an inner shell that gets filled by an electron from an outer shell, thereby emitting a photon. The K_α -line owes its name to the fact that the cor-

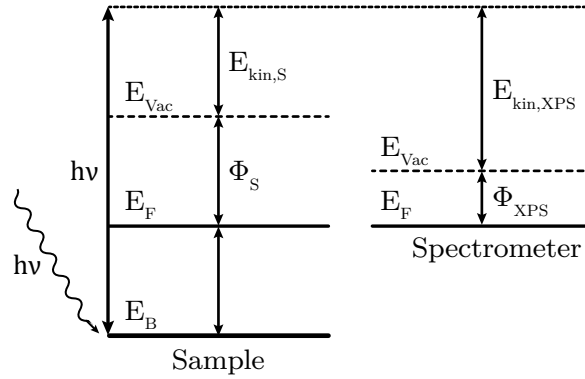


Figure 7.3: A core electron gets kicked out by an irradiated photon with the energy, $h\nu$. It has to overcome the binding energy, E_B , and the work function of the sample, Φ_S . Upon ejection, it carries the kinetic energy, $E_{kin,S}$.

responding knocked-out core electron is located in a K-shell. Most commonly the used targets are magnesium and aluminum due to their narrow full width at half maximum (fwhm) (0.75 eV and 0.85 eV, respectively)¹⁹³, relatively high energy, and intensity of the K_α -line. In cases where higher K_α -energies are needed also silicon, zirconium, silver, titanium or chromium are used but with the drawback of a wider peak. A narrow line width of the X-ray source is important because this is the most important contribution to the energy resolution of the whole system. Next in line is the energy resolution of the energy analyzer and the intrinsic width of photoemission.

The next step after creating the X-rays is the monochromatization, which filters out unnecessary parts of the radiation, like bremsstrahlung, and ensures that only the K_α -line remains. This not only maximizes the resolution of the instrument, due to the narrow fwhm of the remaining K_α -line, but it also removes unnecessary radiation that can degrade the sample. Furthermore, the monochromator also increases the photon flux because, in most cases, it also focuses the beam onto the sample. The monochromator is a concave single crystal that works according to Bragg's law as

$$n\lambda = 2d \sin \varphi. \quad (7.5)$$

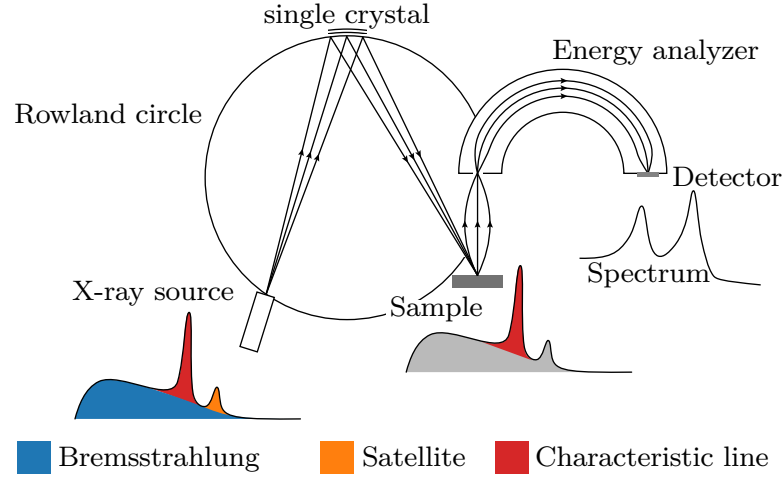


Figure 7.4: The radiation emitted by the X-ray source includes Bremsstrahlung, lower intensity characteristic lines (also known as satellites), and the wanted characteristic lines. To filter out the bremsstrahlung and the satellites (monochromatize) a single crystal mirror is used. To focus the X-rays onto the sample, the source, the crystal mirror, and the sample must be positioned on the so-called Rowland circle. The ejected photoelectrons are measured by an energy analyzer. Adapted from Greczynski and Hultman.¹⁹²

Where n is Bragg's reflection order, λ the wavelength of the radiation, d the lattice distance and φ the reflection angle. To reflect the $Al - K_{\alpha}$ energy, quartz crystal $\langle 10\bar{1}0 \rangle$ planes are usually used. However, I want to note that this effect alone only filters the radiation but does not focus it. To focus the X-rays the crystal must be slightly concave, and the source and the sample must be in the correct angle and distance. Specifically, they must lie on the same imaginary circle, the so-called Rowland circle. The whole process is shown in Figure 7.4.

After the X-rays have kicked out an electron from the sample this electron needs to be analyzed in terms of its kinetic energy, in order to derive the binding energy of the electron according to Equation 7.4. There are various kinds of electron energy analyzers, but the most used ones are of the concentric hemispherical type. Such analyzers consist of two concentric hemispherical electrodes. The electrons are then accelerated to a certain energy, the pass energy, and enter the analyzer through a slit to then traverse it on a semicircle trajectory, where they are detected at the

end (see right side of Figure 7.4). Depending on the specific energy the electrons have, they will have different trajectories and are only detected with the correct energy. This energy filter is used to scan through the whole energy range of interest.

For all this to work, vacuum is needed in the system to ensure that the photoelectrons can travel from the sample to the detector without significant scattering. Another reason why vacuum is important is a clean sample surface since, even if only monolayers of hydrocarbons or water are adsorbed, the measured XPS signal would predominantly stem from this contamination, rather than from the sample itself.

A typical XPS notation for spectral lines gives the element, the principal quantum number, n , the angular quantum number, l , as letter (s,p,d,f), and finally the total angular momentum quantum number, $j = l \pm s$, where s is the spin.

The raw data from an XPS experiment are counts of photoelectrons (intensity) as a function of energy. To translate this into elemental information one can start from theory and the equation that describes the intensity from a core sub-shell, i , for an element, A , with its density, N_A , in small angle $\Delta\Omega$ (typically set by the electron energy analyzers acceptance angle)¹⁹⁴

$$I_{A,i} = \frac{\Delta\Omega}{4\pi} \int_0^\infty I_{h\nu}(\alpha, z) \sigma_{A,i} W_{A,i}(\beta_{A,i}, \Psi) N_A(z) \exp\left(-\frac{z}{\lambda_{m,E(A,i)} \cos \theta}\right) dz. \quad (7.6)$$

Here z is the in-depth distance from the surface, α the incident angle of the X-ray beam with intensity $I_{h\nu}$, $W_{A,i}(\beta_{A,i}, \Psi)$ the angular asymmetry factor at angle Ψ between X-ray and analyzer, $\sigma_{A,i}$ the total ionization cross section, $\lambda_{m,E(A,i)}$ the effective attenuation length and θ the emission angle of the photoelectrons.

This approach requires in-depth knowledge about the sample and system. Therefore, often a simpler approach is used, invoking the sensitivity factors, S . For an atom, A , the sensitivity factor, S_A , corrects the measured intensity, I_A , to enable extraction of the molar fraction, X_A , via

$$\frac{X_A}{X_B} = \frac{\frac{I_A}{S_A}}{\frac{I_B}{S_B}}. \quad (7.7)$$

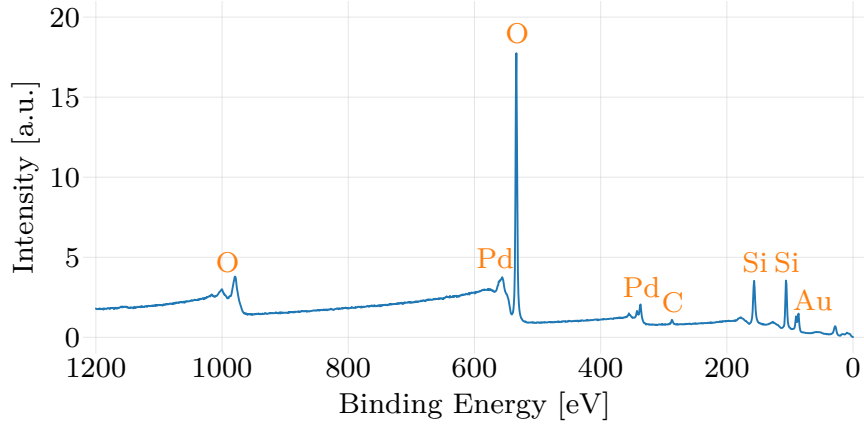


Figure 7.5: A typical XPS-scan of one of my sample surfaces decorated with an array of nanofabricated AuPd alloy nanodisks. One can clearly see the respective peaks for Au and Pd. The silicon and oxygen peaks stem from the support material which is oxidized silicon, and the carbon peak is due to a thin layer of adventitious carbon.

If one considers a sample composed of N different materials this leads to

$$X_i = \frac{\frac{I_i}{S_i}}{\sum_{j=1}^N \frac{I_j}{S_j}} \quad (7.8)$$

$$\sum X_j = 1. \quad (7.9)$$

The way the sensitivity factors are derived for different materials can vary. Most commonly, they are obtained by measuring pure reference elements or by deriving the Scofield cross sections, which consider the energy dependent transmission and attenuation lengths.¹⁹⁴

A typical XPS spectrum obtained by sweeping over the whole energy range is called a survey spectrum and an example of a sample with AuPd nanodisks is shown in Figure 7.5. One can clearly see the respective peaks for Au and Pd. The silicon and oxygen peaks stem from the support material of oxidized silicon and the carbon peak is due to a thin layer of adventitious carbon, which is often comprised of polymeric hydrocarbons.¹⁹⁵ This is usually present on any sample that has been exposed to air. Because of its omnipresence it is quite often used as an internal

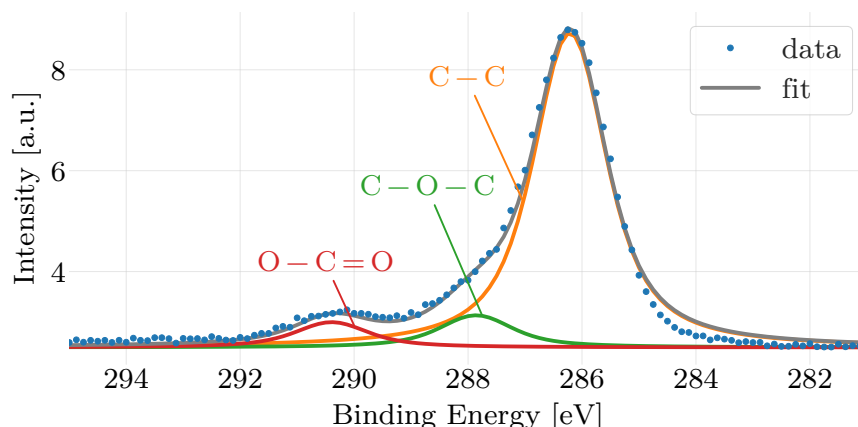


Figure 7.6: The C1s spectrum of adventitious carbon. One can clearly see three different peaks, which provide information about the binding state of the carbon via the chemical shift. Here the strongest peak corresponds to the C–C bond. The secondary peaks correspond to the C–O–C and the O–C=O bonds.

reference for the energy axis of the spectrum. However, this widespread practice is unfortunately not as reliable as widely assumed, as very recently shown by Greczynski and Hultman.¹⁹² Therefore, referencing of the energy scale needs more careful handling.

The survey-type XPS spectrum typically has a lower energy resolution (lower pass energy and energy steps) and is normally used to get a quick overview of what elements are present in the sample, and a rough estimate of the composition. Especially if all materials are present in a larger quantity this gives already satisfactory results. Subsequently, if more detailed information is required, a closer look with higher energy resolution will provide a more detailed view of sample composition and their chemical state, via so-called chemical shifts. In Figure 7.6 this is shown for the C1s peak, where the strongest peak corresponds to the C–C bond. The secondary peaks correspond to the C–O–C and the O–C=O bonds.

Similarly, looking at a Pd 3d peak, one can see that it is split into two parts (Figure 7.7), due to the spin-orbit-splitting for orbits with an angular momentum $l \neq 0$. Additionally, one can in this example see the contribution of PdO and PdO₂. Finally, it is important to note that it is key for the deconvolution of the raw spectrum into

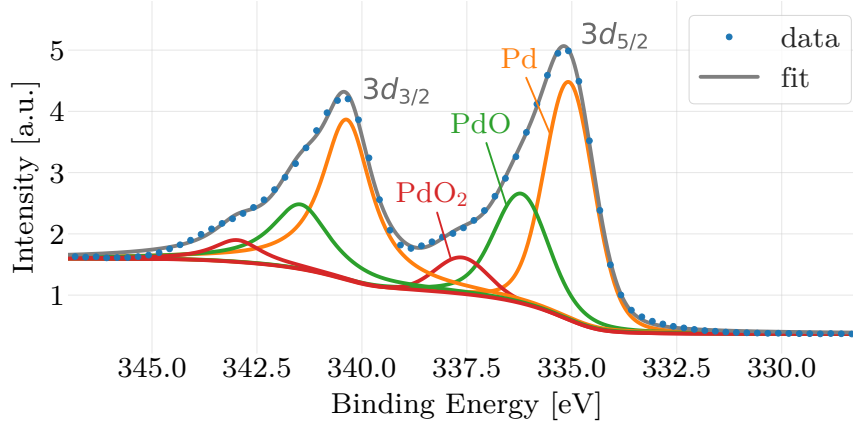


Figure 7.7: The Pd 3d peak is due to spin-orbit splitting divided into $3d_{3/2}$ and $3d_{5/2}$. Additionally, one can see a contribution from PdO and PdO₂ on this sample. Further it should be noticed that for this kind of analysis the background from inelastically scattered electrons need to be removed, in this case this was done using the Shirley background.

constituent peaks to remove the underlying background from the inelastically scattered electrons. The three most common background types are a simple linear approximation, the Shirley background (used in Figure 7.7) and the Tougaard-background. The Shirley background assumes that the background intensity is proportional to the binding energy and the Tougaard background uses the quantitative description of inelastic scattered electrons and is therefore the only background which has a real physical meaning, i.e., is not purely empirical. Tougaard and Jansson¹⁹⁶ found that using the Tougaard background offers the highest consistency and validity of the above-mentioned background types.

XPS, in **Paper I** and **II**, was utilized to analyze oxidation states of single metal nanoparticles and alloy constituents, and to confirm alloy formation after annealing.

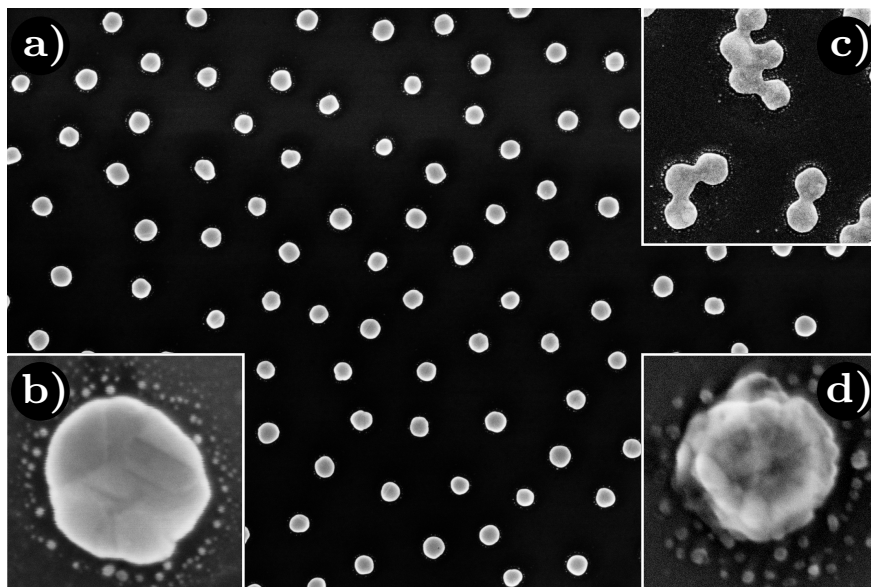


Figure 7.8: SEM images of (an array of) nanofabricated AuPd alloy nanodisks as a) an overview of, b) a zoom-in on a single disk, and c) a region with aggregated particles. d) A single Cu disk with signs of significant oxidation, as indicated by the rough surface.

7.3 Scanning Electron Microscopy

A scanning electron microscope (SEM) is a setup that can be used to examine the geometry and topography of a sample. The typical spatial resolution is around 1 nm for a conducting specimen but can nowadays easily reach the sub-nanometer limit.¹⁹⁷ SEM is a very popular technique since it is easy to obtain images of good quality and with nanometer resolution. The main purpose of SEM in **Paper I, II, III, IV** and **V** was to determine the exact geometry and/or surface coverage of the nanofabricated nanodisks and their arrays, respectively, after annealing (Figure 7.8 a/b). Furthermore, it was also very valuable for the assessment of the condition of the sample in terms of aggregate formation (Figure 7.8c) and oxidation (Figure 7.8d) for all appended papers.

A schematic of the electron optics of a SEM is shown in Figure 7.9a. They are comprised of an electron source that provides electrons, with energy up to 30 keV, required for the imaging. Quite often it is a field-emission gun due to the small spot

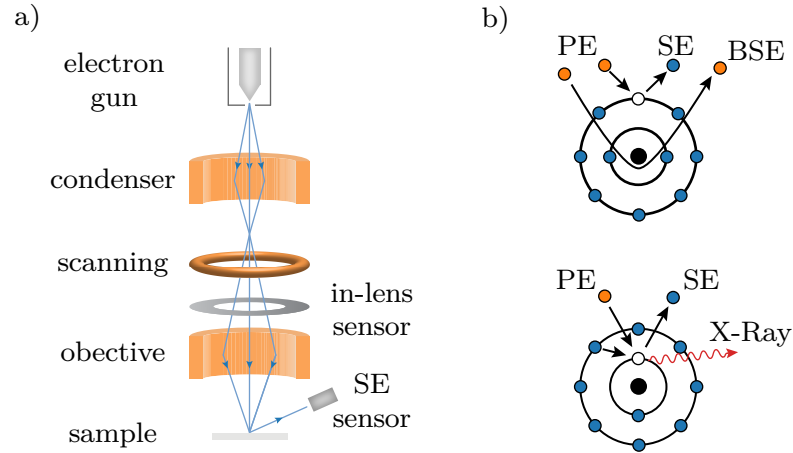


Figure 7.9: a) Schematic of the electron optics in a SEM. It is comprised of an electron gun, condenser and objective lenses to control density and focus of the electron beam, a scanning coil to be able to scan the beam over the sample, and two sensors to detect the electrons. b) The three possible scenarios of interaction of the primary electron (PE) beam with the sample surface. Either secondary electrons (SE) are emitted, the PE electrons are back scattered (BSE), or X-rays are produced. The latter can be analyzed in so-called energy-dispersive X-ray analysis (EDX), providing information about the elemental composition of the sample.

size and high current density it can produce. A system of lenses (condenser and objective lenses) is subsequently used to control the beam density and the focus. A third type of lenses are the scan coils. Their task is to raster the beam over the sample to obtain an image of a specific sample area.

The irradiated beam of primary electrons (PE) creates several signals upon interaction with the imaged surface: (i) back scattered electrons (BSE); (ii) secondary electrons (SE); (iii) Auger electrons; and (iv) X-rays (Figure 7.9b).¹⁹⁸

BSE create an image mainly due to any material contrast in the sample since the backscattering coefficient depends on the element. The heavier the atom is the more it backscatters.¹⁹⁸ Therefore, lighter elements appear darker in the BSE-image and heavier elements brighter.

SE are electrons created by ionization of the atoms via the PE beam (Figure 7.9b).

They have an energy between a few electron volts to around 50 eV. The SE do not yield much information about the chemical composition of the sample but instead reveal its topography. Due to their relatively low energy, they origin from within only a few nanometers from the sample surface.¹⁹⁸ For **Paper I, II, III, IV**, and **V** only secondary electron images were collected.

The created X-rays and Auger electrons can be used for analyzing the chemical elements present in the sample. In case of X-rays, this technique is called energy-dispersive X-ray spectroscopy which is explained in more detail below.

7.4 Energy-Dispersive X-Ray Spectroscopy

Energy-Dispersive X-ray Spectroscopy (EDS or EDX) analyses the characteristic X-rays that are created when a sample is irradiated with high energy electrons as, for example, in SEM or transmission electron microscopy (TEM), to investigate the elemental composition and by rastering the PE-beam even create elemental maps. To excite most elements, characteristic X-rays of up to 20 keV are needed.¹⁹⁹ The silicon drift detector is nowadays most common to detect the radiation.²⁰⁰ In simplified terms, the detector works by converting the characteristic X-rays inside a silicon crystal into an electron cloud whose charge is proportional to the X-ray energy. The induced conversions are counted and plotted as a histogram with counts against energy which can be compared to known reference spectra to gain knowledge about the elemental composition of the sample (Figure 7.10a). These spectra contain not only qualitative but also quantitative information by considering the individual fluorescence yield and X-ray absorption properties of the elements.²⁰⁰

EDS is most used in TEM and SEM setups. TEM is similar to SEM, but the electrons are passing through the sample and are analyzed behind it. This requires usually higher electron beam energies, typically 50 keV to 300 keV, and thin sample thickness of 10 nm to 100 nm.¹⁹⁸ Because typical nanostructure thicknesses in **Paper I** and **II** are already 25 nm special substrates are needed for TEM-based analysis. Therefore, we used so-called TEM-windows as first introduced by Grant et al.²⁰¹ with a substrate thickness of only 25 nm. In **Paper I** and **II**, we used TEM in

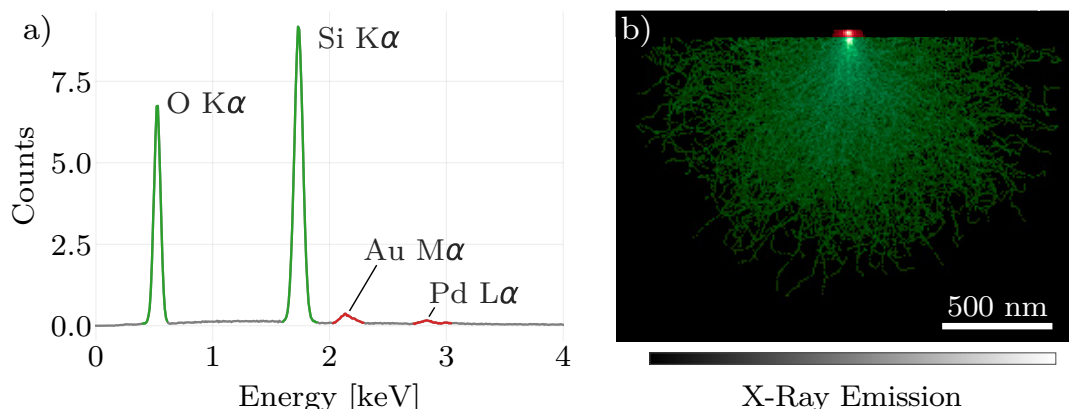


Figure 7.10: a) Monte Carlo simulation of an EDS spectrum of an Au-Pd alloy (50 at.%) disk with a diameter of 140 nm and a thickness of 25 nm on a SiO₂ substrate excited with a 10 keV primary electron beam. The spectrum shows the elemental composition of the simulated geometry via the peaks of Au, Pd, Si, and O. The simulation was done with the built-in Monte Carlo simulation tool in the NIST DTSA-II software tool.²⁰² b) The simulation shows also where the X-Ray production is located. Most X-Rays are created in the large volume underneath the Au-Pd disk in the SiO₂ substrate (green) and not in the system of interest, the disk itself (red), resulting in the low intensity of the respective Au and Pd peaks in the spectrum compared to the Si and O peaks.

combination with EDS to map the elemental composition of my alloy nanostructures with high spatial resolution.

To confirm the capabilities of the microshutter presented in **Paper V** to create alloys with the desired composition the high spatial resolution of TEM is not necessary, and I performed SEM-EDS to correlate how exact we fabricated the alloys. SEM-EDS has the advantage that it can be performed on standard substrates without the need to be electron transparent. It comes, however, with the drawback that for thin objects most of the signal stems from the underlying substrate due to the relatively long penetration depth of the elastically scattered primary electrons. This leads to a lot of X-ray creation in the substrate and therefore relatively small signals from the nanoparticles of interest (Figure 7.10a). This can nicely be illustrated by a Monte Carlo simulation of the X-ray creation (Figure 7.10b). One way to increase

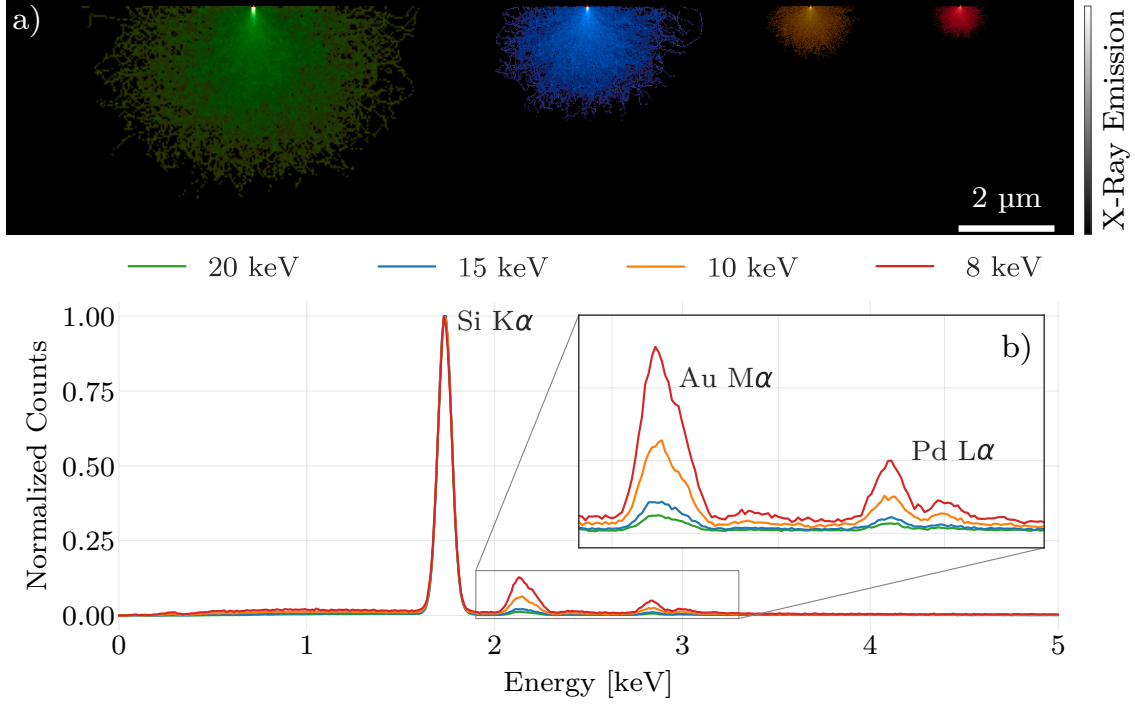


Figure 7.11: a) Monte Carlo Simulation of X-ray creation in an Au-Pd (50 at.%) disk with a diameter of 140 nm and a height of 25 nm on a Si substrate excited with PE-beam energies of 8, 10, 15 and 20 keV, respectively. With lower electron energy the probed volume is reduced significantly. b) Due to the small volume of the sample of interest in my work, i.e., arrays of nanodisks, only the probed substrate volume is affected and the relative peak intensity of the disk elements Au and Pd rises compared to the contribution from the support.

the signal of the nanoparticles compared to the substrate is lowering the primary electron beam acceleration voltage to reduce the penetration depth of the beam. However, it is important to always keep in mind that the energy still needs to be enough to excite the to-be-investigated elements. By, for example, lowering the acceleration voltage from 20 keV to 8 keV, the volume of substrate that contributes to the EDS spectrum can be reduced significantly (Figure 7.11a), leading to a relative peak increase of the nanoparticle elements compared of the substrate elements (Figure 7.11b).

8 Summary and Outlook

8.1 Summary of the Appended Papers

In **Paper I**, we compiled a library of alloy dielectric functions for ten binary alloys based on the late transition metals Pd, Pt, Cu, Au, and Ag by utilizing time-dependent density-functional theory. We benchmarked the calculated dielectric functions by fabricating series of alloy nanoparticle arrays, measuring their plasmonic properties and comparing these properties with electrodynamic simulations using the derived dielectric functions as the input. As the key result, we found very good agreement between experimentally measured and simulated plasmonic response, and thus corroborated the accuracy and relevance of the calculated library of complex dielectric functions. Seen in a wider context, this provides the community with a uniform and consistent set of dielectric functions of the late transition metal alloys, which are receiving increasing attention in the nanophotonics community. In this context, we predict that they, for example, will make it possible to efficiently screen different alloy compositions and materials without the need of producing a large number of samples.

In **Paper II**, we investigated photothermal effects as the reaction enhancing mechanism when noble metal catalyst nanoparticles are irradiated with visible light during a catalytic reaction. Specifically, we investigated the significance of the catalytic light-off curve as a crucial factor to understand reaction rate enhancing mechanisms upon illumination. For this purpose, we alloyed Pd with Au to tailor the catalytic activity in the dark, while, at the same time, maintaining a constant optical cross section. This way, we showed that the catalytic activity is not governed by the photon flux alone but also depends strongly on the catalyst temperature in the dark. Furthermore, we showed, that alloying can be utilized to tailor the light-off curve of

a catalyst to both enhance or suppress the photothermal enhancement channel. Surprisingly, in the field of plasmon mediated catalysis the demonstrated effects are very rarely explicitly considered in the assessment discussion of potential reaction rate enhancing mechanisms upon plasmonic catalyst illumination. Therefore, we anticipate that our explicit demonstration of up to three orders of magnitude different photothermal rate enhancement for constant photon flux when moving a catalyst along its light-off curve will raise the necessary awareness in the field of plasmon mediated catalysis and provide novel concepts for the assessment of light-induced catalytic reaction enhancement on plasmonic nanoparticles.

In **Paper III**, we developed a method to accurately, non-invasively, and directly determine the absolute temperature of nanoparticles by utilizing the phase transformation of Pd to Pd-hydride. Specifically, we showed that the temperature depended first-order phase transformation from Pd to Pd-hydride can be used to measure temperatures at the nanoscale using a reversed Van ‘t Hoff analysis by heating Pd nanoparticles on a glass substrate with varying irradiation powers. This revealed a distinct temperature increase of the nanoparticles with increasing illumination. Further, we showed that a temperature resolution of just under 1 °C can be reached and traded, if necessary, for measurement speed. In a next step, we compared the temperatures obtained by the hydrogen nanothermometry method with temperature measured by a thermocouple touching the sample and were able to reveal a small difference. This temperature difference stems from the fact that the collective heating of the nanoparticles by light absorption results in higher temperature in the middle of the sample and lower temperatures at the edge where the thermocouple is mounted. Weak thermal contact between the thermocouple and the sample further increased this difference, as we were able to corroborate with heat transfer simulations. As the last step, we put the method to an additional test by increasing the nanoparticle density on the surface, which indeed resulted in higher nanoparticle temperatures due to increased collective heating, as confirmed by an analytical model.

In **Paper IV**, we systematically screened the non-radiative LSPR decay of ten binary late transition metal alloys as a function of their composition and also nanoparticle size, to study the impact of alloying on light absorption. As a first step, we fabricated quasi-random arrays of three alloy system in 10 at.% composition steps,

where we compared their experimentally obtained optical absorption efficiencies with FDTD simulations to validate the entire approach, using the complex dielectric functions from **Paper I** as input. After finding good agreement, we extended the calculation of the absorption efficiency to 14 different particle sizes and in total ten binary alloys composed of Au, Ag, Cu, Pt and Pd. The analysis of these calculations showed nicely how for most sizes and alloy systems, an alloy shows the highest absorption in the visible range. As the key result of this paper, this finding thus demonstrates that alloying is an interesting and widely unexplored handle to maximize light absorption in metal nanostructures. Therefore, we predict that this work puts alloying as means to tailor light absorption further into the spotlight and that it will find application in areas like plasmon-enhanced catalysis, photovoltaics and nanomedicine.

In **Paper V**, we developed a microshutter device, which in combination with physical vapor deposition, can be used to evaporate metal thin films of precise thickness and with very high spatial resolution of down to $0.4\text{ }\mu\text{m}$ and $20\text{ }\mu\text{m}$ in x and y direction, respectively, in terms of local composition. In combination with other nanolithography techniques like electron beam evaporation this device enables the precise fabrication of samples comprised of alloy nanoparticles with different composition next to each other by subsequently evaporating multiple metal thin films that upon thermal annealing form alloy nanoparticles. To demonstrate the microshutter, we fabricated arrays of the three binary alloys AuAg, AuPd and AgPd, where each array features a composition gradient from one metal to the other, and in which each nanoparticle has its own distinct alloy composition. Further, we validated the composition of the single particles by energy-dispersive X-ray spectroscopy measurements and found excellent agreement between designed and measured composition. As a second validation method and a first showcase of how samples made using the microshutter can be used to screen a large number of alloy nanoparticle compositions at the same time, we measured the alloy scattering spectra in a single particle plasmonic nanospectroscopy setup and compared these to FDTD calculations, finding good agreement. Finally, we applied the same nanospectroscopy method to demonstrate how easily different compositions of AuPd nanoparticles can be screened at the same time for their response to hydrogen gas. This kind of measurement is, for example, useful to further improve the performance of plasmonic hydrogen sensors. However, it is not

only relevant for sensing applications but also to, for example, screen different alloys in catalysis applications.

8.2 Outlook

Beyond this thesis work, I hope to see mainly two tracks pursued in the future, to which my work has laid the foundation. The first track is to see the dielectric functions for late transition metal alloys being used in all kinds of projects to explore different alloy combinations with respect to both mixed materials and number of constituents in the context of fundamental nanomaterials science and (photo)catalysis, like the optimization of nanophotonic devices and the improvement of plasmonic sensors. An interesting route would for example be the topic of ordered intermetallic phases and their optical response, as we touched upon in **Paper I**. It would be interesting to utilize the theoretical knowledge acquired and apply it to alloy samples by using them, as in situ optical sensors for monitoring annealing processes or chemical reactions that alter an ordered phase. An interesting candidate in this respect is AuCu alloys, since this system exhibits several different ordered phases. Furthermore, it is an interesting system for the catalysis of propene epoxidation²⁰³ and benzyl alcohol oxidation.²⁰⁴ Thankfully, experimental screening of multiple alloy compositions and nanoparticle sizes is now much easier thanks to the introduction of the microshutter device, which makes it possible to monitor the response of multiple different particles at the same time. To summarize this part, I hope that my work has made a contribution to putting alloys into even stronger focus in the plasmonic and nanophotonic communities as they are an excellent setscrew to tailor the optical behavior of nanostructured materials beyond the traditionally used handles of particle shape and size.

The second track is the entanglement of the enhancement mechanics in plasmon-enhanced catalysis. Firstly, I hope to see a further increased awareness of the importance of the light-off curve when discussing enhancement effects in the kinetically limited regime of a chemical reaction. But not only awareness, the light-off curve can deliberately be used to design the plasmon-enhanced catalysis experiments to suppress or enhance the photothermal channel, depending on the temperature. In

combination with such an approach, the hydrogen nanothermometry method I have developed then could provide a way to determine the correct absolute nanoparticle temperatures during reaction, especially under illumination. In this context it is important to note that the hydrogen nanothermometry method is not restricted to only Pd, since other materials also form hydrides and exhibit LSPR. Niobium could, for example, be an interesting candidate as niobium oxides also act as photocatalysts for water splitting.²⁰⁵ Further, I want to highlight that hydrogen nanothermometry can be used in harmony with other applications that utilize plasmonic nanoparticles and where it is important to accurately measure temperature changes induced by illumination such as in optoelectronics or the development of photothermal medicine.^{206,207} Additionally, I propose to use the method in combination with nanoimaging to create thermal images of surfaces with a spatial resolution down to the micrometer. Finally, it would also be interesting to further develop the hydrogen nanothermometry method itself, for example, by increasing the temperature resolution or the measurement speed. The latter could be achieved by, firstly, utilizing an experimental setup with low thermal mass and low volume, therefore enabling a fast gas exchange and, secondly, by using Pd alloy nanoparticles to speed up the kinetics of the hydride formation, and thus the time resolution of the temperature measurement.

Acknowledgments

First of all, I want to acknowledge the financial support to my project of the Knut and Alice Wallenberg Foundation project 2016.0210, to the MC2 cleanroom and CMAL facilities at Chalmers.

First and foremost, I want to thank my supervisor Christoph for the opportunity to do this journey, his guidance and all the help I got. I admire your optimism, your enthusiasm and your ability to spark fascination, even for the more boring topics!

I also want to thank my co-supervisor Paul for the discussions and my examiner Henrik for his input on this thesis and making Chemical Physics the nice work place it is.

Thanks to all my colleagues at Chemical Physics for a great time at work, outside of Chalmers, at conferences and let's not forget during fika.

Thanks to all members of the Langhammer group for making it just a really nice work place. And let's not forget the past members Stephan, Irem and Arturo for providing a smooth entry into the world of a PhD student and Zafer and Ferry, which kept up the help even after leaving the group.

Thanks to David and Sara, for all kinds of discussions, help around FDTD and teaching, and all the other things.

Thanks to the big lab crew Iwan (still counting you as current member), David and Carl (I know you are technically not counting) making the lab the perfect place for getting even the most annoying experiment done but also to vent all non science related things if needed :)

Thanks to my past office mates Johan and Olga to create the best office at Chalmers. And of course thanks to my current office mates. I couldn't have done this without my buddy and spiritual guide Henrik Klein Moberg ;)

Thanks also to Lars, Lasse, Eric and Henrik for the more technical support, always helping, patiently answering my question and getting done what was needed.

Thanks to all my collaborators Astrid and the folks at Condensed Matter and Materials Theory, especially Magnus and Tuomas for not getting tired of my questions.

And also a big thanks to everyone I (most probably) forgot to mention (and sorry about that)!

A big thanks also to my family and my friends for always supporting me, make life a nice place to be and helping me to endure the more stressful times at work.

And finally, a huge thank you to my wife Kristina and my son Villem (even if he technically was not around most of the time) for always standing by my side and enjoying the journey with me. I love you!

Bibliography

- ¹H. Hellström, *När lyktorna tänds*, Det kommer aldrig va över för mig, Universal Music AB, 2013.
- ²E. Starke and J. Staley, “Application of modern aluminum alloys to aircraft”, *Progress in Aerospace Sciences* **32**, 131–172 (1996).
- ³G. Butterworth and C. Forty, “A survey of the properties of copper alloys for use as fusion reactor materials”, *Journal of Nuclear Materials* **189**, 237–276 (1992).
- ⁴H. Yang, Z. Ma, C. Lei, L. Meng, Y. Fang, J. Liu, and H. Wang, “High strength and high conductivity Cu alloys: a review”, *Science China Technological Sciences* **63**, 2505–2517 (2020).
- ⁵S. Li, X. Yang, J. Hou, and W. Du, “A review on thermal conductivity of magnesium and its alloys”, *Journal of Magnesium and Alloys* **8**, 78–90 (2020).
- ⁶C. Veiga, J. Davim, and A. Loureiro, “Properties and applications of titanium alloys: a brief review”, *Rev. Adv. Mater. Sci* **32**, 133–148 (2012).
- ⁷T. A. Rickard, “The use of meteoric iron”, *The Journal of the Royal Anthropological Institute of Great Britain and Ireland* **71**, 55 (1941).
- ⁸E. P. DeGarmo, J. T. Black, R. A. Kohser, and B. E. Klamecki, *Materials and processes in manufacturing*. (Wiley, 2003), ISBN: 0471033065.
- ⁹T. Bell, *Top steel alloying agents*, <https://www.thoughtco.com/common-steel-alloying-agents-properties-and-effects-2340004>, (accessed: 16.03.2022).
- ¹⁰M. Rebello Sousa Dias and M. S. Leite, “Alloying: a platform for metallic materials with on-demand optical response”, *Accounts of chemical research* **52**, 2881–2891 (2019).
- ¹¹C. Gong and M. S. Leite, “Noble metal alloys for plasmonics”, *ACS Photonics* **3**, 507–513 (2016).

- ¹²H. Fukutani, “Optical constants of silver-gold alloys”, *Journal of the Physical Society of Japan* **30**, 399–403 (1971).
- ¹³D. Rioux, S. Vallières, S. Besner, P. Muñoz, E. Mazur, and M. Meunier, “An analytic model for the dielectric function of Au, Ag, and their alloys”, *Advanced Optical Materials* **2**, 176–182 (2014).
- ¹⁴J. Rivory, “Optical properties of ordered and disordered Au-Cu alloys”, *Le Journal de Physique Colloques* **35**, C4–51–C4–56 (1974).
- ¹⁵D. Lioubtchenko, S. Tretyakov, and S. Dudorov, *Millimeter-wave waveguides* (Springer New York, 2004), ISBN: 1-4020-7531-6.
- ¹⁶K. Han and C.-H. Chang, “Numerical modeling of sub-wavelength anti-reflective structures for solar module applications”, *Nanomaterials* **4**, 87–128 (2014).
- ¹⁷T. Shegai, P. Johansson, C. Langhammer, and M. Käll, “Directional scattering and hydrogen sensing by bimetallic Pd–Au nanoantennas”, *Nano Letters* **12**, 2464–2469 (2012).
- ¹⁸S. Yaemsiri, N. Hou, M. M. Slining, and K. He, “Growth rate of human fingernails and toenails in healthy american young adults”, *Journal of the European Academy of Dermatology and Venereology* **24**, 420–423 (2010).
- ¹⁹T. S. M. Company, *5 nm technology*, https://www.tsmc.com/english/dedicatedFoundry/technology/logic/1_5nm, (accessed: 09.08.2022).
- ²⁰I. Chorkendorff and J. W. Niemantsverdriet, *Concepts of modern catalysis and kinetics* (John Wiley & Sons, 2017), ISBN: 9783527305742.
- ²¹J. Zhang, B. Tian, L. Wang, M. Xing, and J. Lei, *Photocatalysis: fundamentals, materials and applications*, Vol. 100 (Springer, 2018), ISBN: 978-981-13-2113-9.
- ²²P. Christopher, H. Xin, and S. Linic, “Visible-light-enhanced catalytic oxidation reactions on plasmonic silver nanostructures”, *Nature Chemistry* **3**, 467–472 (2011).
- ²³S. Linic, U. Aslam, C. Boerigter, and M. Morabito, “Photochemical transformations on plasmonic metal nanoparticles”, *Nature Materials* **14**, 567–576 (2015).
- ²⁴W. Hou and S. B. Cronin, “A review of surface plasmon resonance-enhanced photocatalysis”, *Advanced Functional Materials* **23**, 1612–1619 (2013).
- ²⁵J. R. Adleman, D. A. Boyd, D. G. Goodwin, and D. Psaltis, “Heterogenous catalysis mediated by plasmon heating”, *Nano Letters* **9**, 4417–4423 (2009).

- ²⁶P. Christopher, H. Xin, and S. Linic, "Visible-light-enhanced catalytic oxidation reactions on plasmonic silver nanostructures", *Nature chemistry* **3**, 467–472 (2011).
- ²⁷S. Mukherjee, F. Libisch, N. Large, O. Neumann, L. V. Brown, J. Cheng, J. B. Lassiter, E. A. Carter, P. Nordlander, and N. J. Halas, "Hot electrons do the impossible: Plasmon-induced dissociation of H₂ on Au", *Nano Letters* **13**, 240–247 (2013).
- ²⁸S. Linic, U. Aslam, C. Boerigter, and M. Morabito, "Photochemical transformations on plasmonic metal nanoparticles", *Nature materials* **14**, 567–576 (2015).
- ²⁹Y. Sivan, I. W. Un, and Y. Dubi, "Assistance of metal nanoparticles in photocatalysis—nothing more than a classical heat source", *Faraday discussions* **214**, 215–233 (2019).
- ³⁰Y. Dubi and Y. Sivan, "Hot electrons in metallic nanostructures—non-thermal carriers or heating?", *Light: Science & Applications* **8**, 89 (2019).
- ³¹P. K. Jain, "Comment on "thermal effects-an alternative mechanism for plasmon-assisted photocatalysis" by y. dubi, i. w. un and y. sivan,; chem. sci., 2020, 11, 5017", *Chemical Science* **11**, 9022–9023 (2020).
- ³²Y. Dubi, I. W. Un, and Y. Sivan, "Reply to the 'comment on "thermal effects-an alternative mechanism for plasmon-assisted photocatalysis"' by p. jain,; chem. sci., 2020, 11, doi: 10.1039/d0sc02914a", *Chemical Science* **11**, 9024–9025 (2020).
- ³³Y. Dubi, I. W. Un, and Y. Sivan, "Thermal effects - an alternative mechanism for plasmon-assisted photocatalysis", *Chemical Science* **11**, 5017–5027 (2020).
- ³⁴L. Zhou, D. F. Swearer, C. Zhang, H. Robotjazi, H. Zhao, L. Henderson, L. Dong, P. Christopher, E. A. Carter, P. Nordlander, and N. J. Halas, "Quantifying hot carrier and thermal contributions in plasmonic photocatalysis", *Science* **362**, 69–72 (2018).
- ³⁵Y. Sivan, J. Baraban, I. W. Un, and Y. Dubi, "Comment on "quantifying hot carrier and thermal contributions in plasmonic photocatalysis"", *Science* **364** (2019).
- ³⁶L. Zhou, D. F. Swearer, H. Robotjazi, A. Alabastri, P. Christopher, E. A. Carter, P. Nordlander, and N. J. Halas, "Response to comment on "quantifying hot carrier and thermal contributions in plasmonic photocatalysis"", *Science* **364** (2019).

- ³⁷G. Baffou, I. Bordacchini, A. Baldi, and R. Quidant, “Simple experimental procedures to distinguish photothermal from hot-carrier processes in plasmonics”, *Light: Science & Applications* **9**, 108 (2020).
- ³⁸F. Habashi, *Alloys: preparation, properties, applications* (John Wiley & Sons, 2008), ISBN: 978-3-527-61192-8.
- ³⁹W. D. Callister and D. G. Rethwisch, *Materials science and engineering: an introduction*, Vol. 9 (Wiley New York, 2018), ISBN: 978-1-119-40549-8.
- ⁴⁰C. L. Bracey, P. R. Ellis, and G. J. Hutchings, “Application of copper–gold alloys in catalysis: current status and future perspectives”, *Chemical Society Reviews* **38**, 2231 (2009).
- ⁴¹A. K. Singh and Q. Xu, “Synergistic catalysis over bimetallic alloy nanoparticles”, *ChemCatChem* **5**, 652–676 (2013).
- ⁴²K. Sytwu, M. Vadai, and J. A. Dionne, “Bimetallic nanostructures: combining plasmonic and catalytic metals for photocatalysis”, *Advances in Physics: X* **4**, 1619480 (2019).
- ⁴³H. Okamoto, M. Schlesinger, and E. Mueller, *Alloy Phase Diagrams* (ASM International, 2016), ISBN: 978-1-62708-163-4.
- ⁴⁴U. Mizutani, *Hume-rothery rules for structurally complex alloy phases* (CRC Press, 2016), ISBN: 9781420090598.
- ⁴⁵A. Kawecki, T. Knych, E. Sieja-Smaga, A. Mamala, P. Kwaśniewski, G. Kiesiewicz, B. Smyrak, and A. Pacewicz, “Fabrication, properties and microstructures of high strength and high conductivity copper-silver wires”, *Archives of Metallurgy and Materials* **57**, 1261–1270 (2013).
- ⁴⁶S. Nag, T. Junge, and W. A. Curtin, “Atomistic-continuum coupling of random alloys”, *Modelling and Simulation in Materials Science and Engineering* **27**, 075004 (2019).
- ⁴⁷D. K. Ferry, *Semiconductors*, 2053-2563 (IOP Publishing, 2013), ISBN: 978-0-750-31044-4.
- ⁴⁸D. Salgado and R. Lillard, “Metal salt solutions as a simulant for the chemistry in crevices of nickel alloy 625”, *Journal of The Electrochemical Society* **164**, C801 (2017).

- ⁴⁹S. Ghosh, A. Grover, G. Dey, and M. Totlani, “Nanocrystalline Ni–Cu alloy plating by pulse electrolysis”, *Surface and Coatings Technology* **126**, 48–63 (2000).
- ⁵⁰K. Upadhyay, “Thermodynamics and kinetics of simultaneous reduction of nickel oxide by iron and carbon to produce Ni-Fe alloys”, *Journal of materials engineering* **13**, 29–37 (1991).
- ⁵¹P.-Y. Silvert, V Vijayakrishnan, P Vibert, R Herrera-Urbina, and K. Elhsissen, “Synthesis and characterization of nanoscale Ag-Pd alloy particles”, *Nanostructured materials* **7**, 611–618 (1996).
- ⁵²M. Bala, S. Gupta, T. S. Tripathi, S. K. Tripathi, K Asokan, D. K. Avasthi, et al., “Phase evolution and electrical properties of Co–Sb alloys fabricated from Co/Sb bilayers by thermal annealing and ion beam mixing”, *Physical Chemistry Chemical Physics* **17**, 24427–24437 (2015).
- ⁵³F. A. A. Nugroho, B. Iandolo, J. B. Wagner, and C. Langhammer, “Bottom-Up Nanofabrication of Supported Noble Metal Alloy Nanoparticle Arrays for Plasmonics”, *ACS Nano* **10**, 2871–2879 (2016).
- ⁵⁴F. C. Campbell, *Elements of Metallurgy and Engineering Alloys* (ASM International, Materials Park, United States, 2008), ISBN: 9781615030583.
- ⁵⁵M. Zhao, W. G. Sloof, and A. J. Böttger, “Modelling of surface segregation for palladium alloys in vacuum and gas environments”, *International Journal of Hydrogen Energy* **43**, 2212–2223 (2018).
- ⁵⁶B. C. Han, A. V. der Ven, G. Ceder, and B.-J. Hwang, “Surface segregation and ordering of alloy surfaces in the presence of adsorbates”, *Physical Review B* **72**, 205409 (2005).
- ⁵⁷D. Raabe, “23 - recovery and recrystallization: phenomena, physics, models, simulation”, in *Physical metallurgy (fifth edition)*, edited by D. E. Laughlin and K. Hono, Fifth Edition (Elsevier, Oxford, 2014), pp. 2291 –2397, ISBN: 978-0-444-53770-6.
- ⁵⁸H. L. Skriver and N. M. Rosengaard, “Surface energy and work function of elemental metals”, *Physical Review B* **46**, 7157–7168 (1992).

- ⁵⁹P. Ekborg-Tanner and P. Erhart, “Hydrogen-driven surface segregation in Pd alloys from atomic-scale simulations”, *The Journal of Physical Chemistry C* **125**, 17248–17260 (2021).
- ⁶⁰S. Zafeiratos, S. Piccinin, and D. Teschner, “Alloys in catalysis: Phase separation and surface segregation phenomena in response to the reactive environment”, *Catalysis Science and Technology* **2**, 1787–1801 (2012).
- ⁶¹K. J. Andersson, F. Calle-Vallejo, J. Rossmeisl, and I. Chorkendorff, “Adsorption-driven surface segregation of the less reactive alloy component”, *Journal of the American Chemical Society* **131**, 2404–2407 (2009).
- ⁶²W. H. Wollaston, “XVII. on a new metal, found in crude platina”, *Philosophical Transactions of the Royal Society of London* **94**, 419–430 (1804).
- ⁶³T. Graham, “On the relation of hydrogen to palladium”, *Proceedings of the Royal Society of London* **17**, 212–220 (1869).
- ⁶⁴L. Zhang, Q. Chang, H. Chen, and M. Shao, “Recent advances in palladium-based electrocatalysts for fuel cell reactions and hydrogen evolution reaction”, *Nano Energy* **29**, 198–219 (2016).
- ⁶⁵M. Skoglundh, H. Johansson, L. Löwendahl, K. Jansson, L. Dahl, and B. Hirschauer, “Cobalt-promoted palladium as a three-way catalyst”, *Applied Catalysis B: Environmental* **7**, 299–319 (1996).
- ⁶⁶R. Rushforth, “Palladium in restorative dentistry”, *Platinum Metals Review* **48**, 30–31 (2004).
- ⁶⁷I. Darmadi, F. A. A. Nugroho, and C. Langhammer, “High-performance nanostructured palladium-based hydrogen sensors—current limitations and strategies for their mitigation”, *ACS Sensors* **5**, 3306–3327 (2020).
- ⁶⁸R. J. Behm, V. Penka, M. G. Cattania, K. Christmann, and G. Ertl, “Evidence for “subsurface” hydrogen on Pd(110): An intermediate between chemisorbed and dissolved species”, *The Journal of Chemical Physics* **78**, 7486–7490 (1982).
- ⁶⁹K. Christmann, “Interaction of hydrogen with solid surfaces”, *Surface Science Reports* **9**, 1–163 (1988).
- ⁷⁰G. Pacchioni and J. Koutecký, “Theoretical investigation of the interaction between the hydrogen atom and pd clusters”, *Surface Science* **154**, 126–138 (1985).

- ⁷¹A. Sieverts, “Absorption of gases by metals”, *Zeitschrift für Metallkunde* **21**, 37–46 (1929).
- ⁷²J. W. Simons and T. B. Flanagan, “Absorption isotherms of hydrogen in the α -phase of the hydrogen-palladium system”, *Journal of Physical Chemistry* **69**, 3773–3781 (1965).
- ⁷³A. Maeland and T. Flanagan, “The hydrogen-palladium system”, *Platinum Metals Review* **10**, 20–24 (1966).
- ⁷⁴R. Schwarz and A. Khachaturyan, “Thermodynamics of open two-phase systems with coherent interfaces: application to metal–hydrogen systems”, *Acta Materialia* **54**, 313–323 (2006).
- ⁷⁵R. B. Schwarz, A. K. Khachaturyan, A. Caro, M. I. Baskes, and E. Martinez, “Coherent phase decomposition in the Pd–H system”, *Journal of Materials Science* **55**, 4864–4882 (2020).
- ⁷⁶E. Wicke, H. Brodowsky, and H. Züchner, “Hydrogen in palladium and palladium alloys”, in *Hydrogen in metals ii: application-oriented properties*, edited by G. Alefeld and J. Völkl (Springer Berlin Heidelberg, Berlin, Heidelberg, 1978), pp. 73–155, ISBN: 978-3-540-35801-5.
- ⁷⁷S. H. Goods and S. E. Guthrie, “Mechanical properties of palladium and palladium hydride”, *Scripta Metallurgica et Materiala* **26**, 561–565 (1992).
- ⁷⁸B. Baranowski, S. Majchrzak, and T. B. Flanagan, “The volume increase of fcc metals and alloys due to interstitial hydrogen over a wide range of hydrogen contents”, *Journal of Physics F: Metal Physics* **1**, 258–261 (1971).
- ⁷⁹S. Dekura, H. Kobayashi, R. Ikeda, M. Maesato, H. Yoshino, M. Ohba, T. Ishimoto, S. Kawaguchi, Y. Kubota, S. Yoshioka, S. Matsumura, T. Sugiyama, and H. Kitagawa, “The electronic state of hydrogen in the α phase of the hydrogen-storage material PdH(D) x : does a chemical bond between palladium and hydrogen exist?”, *Angewandte Chemie* **130**, 9971–9975 (2018).
- ⁸⁰S. Dekura, H. Kobayashi, K. Kusada, and H. Kitagawa, “Hydrogen in palladium and storage properties of related nanomaterials: size, shape, alloying, and metal-organic framework coating effects”, *ChemPhysChem* **20**, 1158–1176 (2019).

- ⁸¹A. Bar-Cohen, P. Wang, and E. Rahim, “Thermal management of high heat flux nanoelectronic chips”, *Microgravity Science and Technology* **19**, 48–52 (2007).
- ⁸²B. C. Stipe, T. C. Strand, C. C. Poon, H. Balamane, T. D. Boone, J. A. Katine, J.-L. Li, V. Rawat, H. Nemoto, A. Hirotsune, O. Hellwig, R. Ruiz, E. Dobisz, D. S. Kercher, N. Robertson, T. R. Albrecht, and B. D. Terris, “Magnetic recording at 1.5 pb m⁻² using an integrated plasmonic antenna”, *Nature Photonics* **4**, 484–488 (2010).
- ⁸³S. Mubeen, J. Lee, W.-r. Lee, N. Singh, G. D. Stucky, and M. Moskovits, “On the plasmonic photovoltaic”, *ACS Nano* **8**, 6066–6073 (2014).
- ⁸⁴P. K. Jain, I. H. El-Sayed, and M. A. El-Sayed, “Au nanoparticles target cancer”, *Nano Today* **2**, 18–29 (2007).
- ⁸⁵Y. Gu, Q. Li, J. Xiao, K. Wu, and G. P. Wang, “Plasmonic metamaterials for ultrasensitive refractive index sensing at near infrared”, *Journal of Applied Physics* **109**, 023104 (2011).
- ⁸⁶G. Baffou, F. Cichos, and R. Quidant, “Applications and challenges of thermoplasmonics”, *Nature Materials* **19**, 946–958 (2020).
- ⁸⁷G. L. Liu, J. Kim, Y. Lu, and L. P. Lee, “Optofluidic control using photothermal nanoparticles”, *Nature Materials* **5**, 27–32 (2005).
- ⁸⁸M. A. van Dijk, A. L. Tchebotareva, M. Orrit, M. Lippitz, S. Berciaud, D. Lasne, L. Cognet, and B. Lounis, “Absorption and scattering microscopy of single metal nanoparticles”, *Phys. Chem. Chem. Phys.* **8**, 3486–3495 (2006).
- ⁸⁹M. Stefan A, *World scientific handbook of metamaterials and plasmonics (in 4 volumes)*. World Scientific Series in Nanoscience and Nanotechnology vol. 16 (World Scientific, 2018), ISBN: 9789813227613.
- ⁹⁰G. Baffou, M. P. Kreuzer, F. Kulzer, and R. Quidant, “Temperature mapping near plasmonic nanostructures using fluorescence polarization anisotropy”, *Optics Express* **17**, 3291 (2009).
- ⁹¹C. D. S. Brites, P. P. Lima, N. J. O. Silva, A. Millán, V. S. Amaral, F. Palacio, and L. D. Carlos, “Thermometry at the nanoscale”, *Nanoscale* **4**, 4799 (2012).
- ⁹²M. Quintanilla and L. M. Liz-Marzán, “Guiding rules for selecting a nanothermometer”, *Nano Today* **19**, 126–145 (2018).

- ⁹³G. Baffou, “Anti-stokes thermometry in nanoplasmonics”, *ACS Nano* **15**, 5785–5792 (2021).
- ⁹⁴M. Damićanin, “Chapter 3 - luminescence: the basics, methods, and instrumentation”, in *Luminescence thermometry*, edited by M. Damićanin, Woodhead Publishing Series in Electronic and Optical Materials (Woodhead Publishing, 2018), pp. 33–61, ISBN: 978-0-08-102029-6.
- ⁹⁵X. Xie and D. G. Cahill, “Thermometry of plasmonic nanostructures by anti-Stokes electronic Raman scattering”, *Applied Physics Letters* **109**, 183104 (2016).
- ⁹⁶M. Barella, I. L. Violi, J. Gargiulo, L. P. Martinez, F. Goschin, V. Guglielmotti, D. Pallarola, S. Schlücker, M. Pilo-Pais, G. P. Acuna, S. A. Maier, E. Cortés, and F. D. Stefani, “In situ photothermal response of single gold nanoparticles through hyperspectral imaging anti-stokes thermometry”, *ACS Nano* **15**, 2458–2467 (2021).
- ⁹⁷C. Langhammer, I. Zorić, B. Kasemo, and B. M. Clemens, “Hydrogen storage in Pd nanodisks characterized with a novel nanoplasmonic sensing scheme”, *Nano Letters* **7**, 3122–3127 (2007).
- ⁹⁸M. Fedoruk, M. Meixner, S. Carretero-Palacios, T. Lohmüller, and J. Feldmann, “Nanolithography by plasmonic heating and optical manipulation of gold nanoparticles”, *ACS Nano* **7**, 7648–7653 (2013).
- ⁹⁹E. Cortés, L. V. Besteiro, A. Alabastri, A. Baldi, G. Tagliabue, A. Demetriadou, and P. Narang, “Challenges in plasmonic catalysis”, *ACS Nano* **14**, 16202–16219 (2020).
- ¹⁰⁰P. Mandal and S. Sharma, “Progress in plasmonic solar cell efficiency improvement: a status review”, *Renewable and Sustainable Energy Reviews* **65**, 537–552 (2016).
- ¹⁰¹C. Wadell, S. Syrenova, and C. Langhammer, “Plasmonic hydrogen sensing with nanostructured metal hydrides”, *ACS Nano* **8**, 11925–11940 (2014).
- ¹⁰²S. A. Maier, *Plasmonics: fundamentals and applications* (Springer Science & Business Media, 2007), ISBN: 978-0-387-37825-1.
- ¹⁰³K. Kolwas and A. Derkachova, “Impact of the interband transitions in gold and silver on the dynamics of propagating and localized surface plasmons”, *Nanomaterials* **10**, 1–27 (2020).

- ¹⁰⁴P. B. Johnson and R. W. Christy, “Optical constants of the noble metals”, *Phys. Rev. B* **6**, 4370–4379 (1972).
- ¹⁰⁵U. Kreibig and M. Vollmer, *Optical properties of metal clusters*, Vol. 25 (Springer Science & Business Media, 2013), ISBN: 978-3-662-09109-8.
- ¹⁰⁶T. Rangel, D. Kecik, P. Trevisanutto, G.-M. Rignanese, H. Van Swygenhoven, and V. Olevano, “Band structure of gold from many-body perturbation theory”, *Physical Review B* **86**, 125125 (2012).
- ¹⁰⁷C. F. Bohren and D. R. Huffman, *Absorption and scattering of light by small particles* (John Wiley & Sons, 2008), ISBN: 9780471293408.
- ¹⁰⁸R. C. Rumpf, *Lecture notes: electromagnetic analysis using finite-difference time-domain*, University of Texas at El Paso, 2019.
- ¹⁰⁹Kane Yee, “Numerical solution of initial boundary value problems involving maxwell’s equations in isotropic media”, *IEEE Transactions on Antennas and Propagation* **14**, 302–307 (1966).
- ¹¹⁰W. Yu, *Advanced FDTD methods: parallelization, acceleration, and engineering applications* (Artech House, 2011), ISBN: 9781608071760.
- ¹¹¹E. D. Palik, *Handbook of optical constants of solids*, Vol. 3 (Academic press, 1998), ISBN: 978-0-12-544422-4.
- ¹¹²J. M. Rahm, C. Tiburski, T. P. Rossi, F. A. A. Nugroho, S. Nilsson, C. Langhammer, and P. Erhart, “A library of late transition metal alloy dielectric functions for nanophotonic applications”, *Advanced Functional Materials* **30**, 2002122 (2020).
- ¹¹³S. Enoch, R. Quidant, and G. Badenes, “Optical sensing based on plasmon coupling in nanoparticle arrays”, *Optics express* **12**, 3422–3427 (2004).
- ¹¹⁴T. J. Antosiewicz, S. P. Apell, M. Zäch, I. Zorić, and C. Langhammer, “Oscillatory optical response of an amorphous two-dimensional array of gold nanoparticles”, *Physical review letters* **109**, 247401 (2012).
- ¹¹⁵I. H. Malitson, “Interspecimen comparison of the refractive index of fused silica”, *Josa* **55**, 1205–1209 (1965).
- ¹¹⁶R. L. Olmon, B. Slovick, T. W. Johnson, D. Shelton, S.-H. Oh, G. D. Boreman, and M. B. Raschke, “Optical dielectric function of gold”, *Phys. Rev. B* **86**, 235147 (2012).

- ¹¹⁷C. Persson, A. F. da Silva, R. Ahuja, and B. Johansson, “First-principle calculations of the dielectric function of zinc-blende and wurtzite InN”, *Journal of Physics: Condensed Matter* **13**, 8945 (2001).
- ¹¹⁸I. Zoric, M. Zach, B. Kasemo, and C. Langhammer, “Gold, platinum, and aluminum nanodisk plasmons: material independence, subradiance, and damping mechanisms”, *ACS nano* **5**, 2535–2546 (2011).
- ¹¹⁹S. Babar and J. H. Weaver, “Optical constants of Cu, Ag, and Au revisited”, *Appl. Opt.* **54**, 477–481 (2015).
- ¹²⁰A. Ciesielski, L. Skowronski, M. Trzcinski, E. Górecka, P. Trautman, and T. Szoplik, “Evidence of germanium segregation in gold thin films”, *Surface Science* **674**, 73–78 (2018).
- ¹²¹H.-J. Hagemann, W. Gudat, and C. Kunz, “Optical constants from the far infrared to the x-ray region: Mg, Al, Cu, Ag, Au, Bi, C, and Al₂O₃”, *J. Opt. Soc. Am.* **65**, 742–744 (1975).
- ¹²²F. Lemarchand, L. Gao, and M. Lequime, “Comparison of different dispersion models for single layer optical thin film index determination”, *Thin Solid Films* **520**, 501–509 (2011).
- ¹²³K. M. McPeak, S. V. Jayanti, S. J. Kress, S. Meyer, S. Iotti, A. Rossinelli, and D. J. Norris, “Plasmonic films can easily be better: Rules and recipes”, *ACS Photonics* **2**, 326–333 (2015).
- ¹²⁴D. L. Windt, W. C. Cash, M. Scott, P. Arendt, B. Newnam, R. F. Fisher, and A. B. Swartzlander, “Optical constants for thin films of Ti, Zr, Nb, Mo, Ru, Rh, Pd, Ag, Hf, Ta, W, Re, Ir, Os, Pt, and Au from 24 Å to 1216 Å”, *Appl. Opt.* **27**, 246–278 (1988).
- ¹²⁵D. I. Yakubovsky, A. V. Arsenin, Y. V. Stebunov, D. Y. Fedyanin, and V. S. Volkov, “Optical constants and structural properties of thin gold films”, *Optics Express* **25**, 25574 (2017).
- ¹²⁶T. Gong, P. Lyu, K. J. Palm, S. Memarzadeh, J. N. Munday, and M. S. Leite, “Metallic alloys: emergent opportunities with metallic alloys: from material design to optical devices”, *Advanced Optical Materials* **8**, 2070091 (2020).

- ¹²⁷S. K. F. Stofela, O. Kizilkaya, B. T. Diroll, T. R. Leite, M. M. Taheri, D. E. Willis, J. B. Baxter, W. A. Shelton, P. T. Sprunger, and K. M. McPeak, “A noble-transition alloy excels at hot-carrier generation in the near infrared”, *Advanced Materials* **32**, 1906478 (2020).
- ¹²⁸M Gaudry, J Lermé, E Cottancin, M Pellarin, J.-L. Vialle, M Broyer, B Prével, M Treilleux, and P Mélinon, “Optical properties of (Au x Ag 1- x) n clusters embedded in alumina: evolution with size and stoichiometry”, *Physical Review B* **64**, 085407 (2001).
- ¹²⁹A. Zunger, S.-H. Wei, L. Ferreira, and J. E. Bernard, “Special quasirandom structures”, *Physical Review Letters* **65**, 353 (1990).
- ¹³⁰C. Carrillo-Carrión, R. Martínez, E. Polo, M. Tomás-Gamasa, P. Destito, M. Ceballos, B. Pelaz, F. López, J. L. Mascareñas, and P. del Pino, “Plasmonic-assisted thermocyclizations in living cells using metal-organic framework based nanoreactors”, *ACS Nano* **15**, 16924–16933 (2021).
- ¹³¹O. Neumann, A. S. Urban, J. Day, S. Lal, P. Nordlander, and N. J. Halas, “Solar vapor generation enabled by nanoparticles”, *ACS Nano* **7**, 42–49 (2012).
- ¹³²L. Tian, S. Tadepalli, M. Fei, J. J. Morrissey, E. D. Kharasch, and S. Singamaneni, “Off-resonant gold superstructures as ultrabright minimally invasive surface-enhanced raman scattering (SERS) probes”, *Chemistry of Materials* **27**, 5678–5684 (2015).
- ¹³³K. M. Mayer and J. H. Hafner, “Localized surface plasmon resonance sensors”, *Chemical Reviews* **111**, 3828–3857 (2011).
- ¹³⁴K. J. Palm, J. B. Murray, T. C. Narayan, and J. N. Munday, “Dynamic optical properties of metal hydrides”, *ACS Photonics* **5**, 4677–4686 (2018).
- ¹³⁵M. D. Malinsky, K. L. Kelly, G. C. Schatz, and R. P. Van Duyne, “Chain length dependence and sensing capabilities of the localized surface plasmon resonance of silver nanoparticles chemically modified with alkanethiol self-assembled monolayers”, *Journal of the American Chemical Society* **123**, 1471–1482 (2001).
- ¹³⁶C. Wadell, F. A. A. Nugroho, E. Lidström, B. Iandolo, J. B. Wagner, and C. Langhammer, “Hysteresis-Free Nanoplasmonic Pd–Au Alloy Hydrogen Sensors”, *Nano Letters* **15**, 3563–3570 (2015).

- ¹³⁷M. Nuopponen and H. Tenhu, “Gold nanoparticles protected with pH and temperature-sensitive diblock copolymers”, *Langmuir* **23**, 5352–5357 (2007).
- ¹³⁸K. M. Mayer, S. Lee, H. Liao, B. C. Rostro, A. Fuentes, P. T. Scully, C. L. Nehl, and J. H. Hafner, “A label-free immunoassay based upon localized surface plasmon resonance of gold nanorods”, *ACS Nano* **2**, 687–692 (2008).
- ¹³⁹S. Suganuma and N. Katada, “Innovation of catalytic technology for upgrading of crude oil in petroleum refinery”, *Fuel Processing Technology* **208**, 106518 (2020).
- ¹⁴⁰M. J. Climent, A. Corma, and S. Iborra, “Converting carbohydrates to bulk chemicals and fine chemicals over heterogeneous catalysts”, *Green Chemistry* **13**, 520 (2011).
- ¹⁴¹M. J. Climent, A. Corma, and S. Iborra, “Heterogeneous catalysts for the one-pot synthesis of chemicals and fine chemicals”, *Chemical Reviews* **111**, 1072–1133 (2010).
- ¹⁴²T. Kurniawan, N. Nuryoto, and M. A. Firdaus, “Zeolite for agriculture intensification and catalyst in agroindustry”, *World Chemical Engineering Journal* **3**, 13–23 (2019).
- ¹⁴³G. Rothenberg, *Catalysis: concepts and green applications* (John Wiley & Sons, 2017), ISBN: 978-3-527-34305-8.
- ¹⁴⁴J. K. Nørskov, J. Rossmeisl, A. Logadottir, L. Lindqvist, J. R. Kitchin, T. Bligaard, and H. Jónsson, “Origin of the overpotential for oxygen reduction at a fuel-cell cathode”, *Journal of Physical Chemistry B* **108**, 17886–17892 (2004).
- ¹⁴⁵V. Ponec, “Alloy catalysts: the concepts”, *Applied Catalysis A: General* **222**, Celebration Issue, 31–45 (2001).
- ¹⁴⁶T. Zhang, A. G. Walsh, J. Yu, and P. Zhang, “Single-atom alloy catalysts: structural analysis, electronic properties and catalytic activities”, *Chemical Society Reviews* **50**, 569–588 (2021).
- ¹⁴⁷D. Wu, X. Shen, Y. Pan, L. Yao, and Z. Peng, “Platinum alloy catalysts for oxygen reduction reaction: advances, challenges and perspectives”, *ChemNanoMat* **6**, 32–41 (2019).

- ¹⁴⁸Y. F. Han, J. H. Wang, D. Kumar, Z. Yan, and D. W. Goodman, “A kinetic study of vinyl acetate synthesis over Pd-based catalysts: Kinetics of vinyl acetate synthesis over Pd-Au/SiO₂ and Pd/SiO₂ catalysts”, *Journal of Catalysis* **232**, 467–475 (2005).
- ¹⁴⁹F. Garin, “Environmental catalysis”, *Catalysis Today* **89**, 255–268 (2004).
- ¹⁵⁰F. Besenbacher, I. Chorkendorff, B. S. Clausen, B. Hammer, A. M. Molenbroek, J. K. Nørskov, and I. Stensgaard, “Design of a surface alloy catalyst for steam reforming”, *Science* **279**, 1913–1915 (1998).
- ¹⁵¹A. Naldoni, F. Riboni, U. Guler, A. Boltasseva, V. M. Shalaev, and A. V. Kildishev, “Solar-powered plasmon-enhanced heterogeneous catalysis”, *Nanophotonics* **5**, 112–133 (2016).
- ¹⁵²M. L. Brongersma, N. J. Halas, and P. Nordlander, “Plasmon-induced hot carrier science and technology”, *Nature Nanotechnology* **10**, 25–34 (2015).
- ¹⁵³Z. Liu, W. Hou, P. Pavaskar, M. Aykol, and S. B. Cronin, “Plasmon resonant enhancement of photocatalytic water splitting under visible illumination”, *Nano Letters* **11**, 1111–1116 (2011).
- ¹⁵⁴T. P. Rossi, M. Kuisma, M. J. Puska, R. M. Nieminen, and P. Erhart, “Kohn–sham decomposition in real-time time-dependent density-functional theory: an efficient tool for analyzing plasmonic excitations”, *Journal of Chemical Theory and Computation* **13**, 4779–4790 (2017).
- ¹⁵⁵A. Manjavacas, J. G. Liu, V. Kulkarni, and P. Nordlander, “Plasmon-induced hot carriers in metallic nanoparticles”, *ACS Nano* **8**, 7630–7638 (2014).
- ¹⁵⁶T. P. Rossi, P. Erhart, and M. Kuisma, “Hot-carrier generation in plasmonic nanoparticles: the importance of atomic structure”, *ACS Nano* **14**, 9963–9971 (2020).
- ¹⁵⁷G. Baffou and R. Quidant, “Nanoplasmonics for chemistry”, *Chemical Society Reviews* **43**, 3898 (2014).
- ¹⁵⁸K. Li, N. J. Hogan, M. J. Kale, N. J. Halas, P. Nordlander, and P. Christopher, “Balancing near-field enhancement, absorption, and scattering for effective antenna-reactor plasmonic photocatalysis”, *Nano Letters* **17**, 3710–3717 (2017).

- ¹⁵⁹J. Aizpurua, F. Baletto, J. Baumberg, P. Christopher, B. De Nijs, P. Deshpande, Y. D. Fernandez, L. Fabris, S. Freakley, S. Gawinkowski, et al., “Theory of hot electrons: general discussion”, *Faraday discussions* **214**, 245–281 (2019).
- ¹⁶⁰US Department of Health and Human Services - Centers for Disease Control and Prevention National - Institute for Occupational Safety and Health, *Niosh pocket guide to chemical hazards*, 2007.
- ¹⁶¹World Health Organization, *Monitoring ambient air quality for health impact assessment* (Copenhagen: WHO Regional Office for Europe, 1999), ISBN: 9789289013512.
- ¹⁶²National Center for Environmental Health, *Carbon monoxide poisoning*, <https://www.cdc.gov/co/faqs.htm>, (accessed: 16.03.2022).
- ¹⁶³Drägerwerk AG & Co. KGaA, *Leitfaden zur filterauswahl*, <https://www.draeger.com/products/content/ab-filter-selection-guide-fl-9046528-de-de.pdf>, (accessed: 16.03.2022).
- ¹⁶⁴N. Soliman, “Factors affecting CO oxidation reaction over nanosized materials: a review”, *Journal of Materials Research and Technology* **8**, 2395–2407 (2019).
- ¹⁶⁵A. C. Garcia, V. A. Paganin, and E. A. Ticianelli, “CO tolerance of PdPt/C and PdPtRu/C anodes for pemfc”, *Electrochimica Acta* **53**, 4309–4315 (2008).
- ¹⁶⁶J. T. Kummer, “Use of noble metals in automobile exhaust catalysts”, *Journal of Physical Chemistry* **90**, 4747–4752 (1986).
- ¹⁶⁷T.-J. Huang and D.-H. Tsai, “CO oxidation behavior of copper and copper oxides”, *Catalysis Letters* **87**, 173–178 (2003).
- ¹⁶⁸A. Biabani-Ravandi and M. Rezaei, “Low temperature CO oxidation over Fe–Co mixed oxide nanocatalysts”, *Chemical Engineering Journal* **184**, 141–146 (2012).
- ¹⁶⁹M. Haruta, T. Kobayashi, H. Sano, and N. Yamada, “Novel gold catalysts for the oxidation of carbon monoxide at a temperature far below 0C”, *Chemistry Letters* **16**, 405–408 (1987).
- ¹⁷⁰I. Langmuir, “The mechanism of the catalytic action of platinum in the reactions $2\text{CO} + \text{O}_2 = 2\text{CO}_2$ and $2\text{H}_2 + \text{O}_2 = 2\text{H}_2\text{O}$ ”, *Transactions of the Faraday Society* **17**, 621–654 (1922).

- ¹⁷¹P. J. Berlowitz, C. H. Peden, and D. W. Goodman, “Kinetics of CO oxidation on single-crystal Pd, Pt, and Ir.”, *Journal of physical chemistry* **92**, 5213–5221 (1988).
- ¹⁷²A. D. Allian, K. Takanabe, K. L. Fajdala, X. Hao, T. J. Truex, J. Cai, C. Buda, M. Neurock, and E. Iglesia, “Chemisorption of CO and mechanism of CO oxidation on supported platinum nanoclusters”, *J. Am. Chem. Soc* **133**, 4498–4517 (2011).
- ¹⁷³R. F. Baddour, M. Modell, and U. K. Heusser, “Simultaneous kinetic and infrared spectral studies of carbon monoxide oxidation on palladium under steady-state conditions”, *The Journal of Physical Chemistry* **72**, 3621–3629 (1968).
- ¹⁷⁴A. M. Venezia, V. La Parola, G. Deganello, B. Pawelec, and J. L. Fierro, “Synergetic effect of gold in Au/Pd catalysts during hydrodesulfurization reactions of model compounds”, *Journal of Catalysis* **215**, 317–325 (2003).
- ¹⁷⁵J. K. Edwards, B. E. Solsona, P. Landon, A. F. Carley, A. Herzing, C. J. Kiely, and G. J. Hutchings, “Direct synthesis of hydrogen peroxide from H₂ and O₂ using TiO₂-supported Au-Pd catalysts”, *Journal of Catalysis* **236**, 69–79 (2005).
- ¹⁷⁶A. Beck, A. Horváth, Z. Schay, G. Stefler, Z. Koppány, I. Sajó, O. Geszti, and L. Guzzi, “Sol derived gold-palladium bimetallic nanoparticles on TiO₂: Structure and catalytic activity in CO oxidation”, *Topics in Catalysis* **44**, 115–121 (2007).
- ¹⁷⁷D. F. Emerich and C. G. Thanos, “Nanotechnology and medicine”, *Expert Opinion on Biological Therapy* **3**, 655–663 (2003).
- ¹⁷⁸L. Rashidi and K. Khosravi-Darani, “The applications of nanotechnology in food industry”, *Critical Reviews in Food Science and Nutrition* **51**, 723–730 (2011).
- ¹⁷⁹X. Qu, P. J. Alvarez, and Q. Li, “Applications of nanotechnology in water and wastewater treatment”, *Water Research* **47**, Nanotechnology for Water and Wastewater Treatment, 3931–3946 (2013).
- ¹⁸⁰J. L. West and N. J. Halas, “Applications of nanotechnology to biotechnology: commentary”, *Current Opinion in Biotechnology* **11**, 215–217 (2000).
- ¹⁸¹U. Banin, N. Waiskopf, L. Hammarström, G. Boschloo, M. Freitag, E. M. J. Johansson, J. Sá, H. Tian, M. B. Johnston, L. M. Herz, R. L. Milot, M. G. Kanatzidis, W. Ke, I. Spanopoulos, K. L. Kohlstedt, G. C. Schatz, N. Lewis, T. Meyer, A. J. Nozik, M. C. Beard, F. Armstrong, C. F. Megarity, C. A. Schmuttenmaer, V. S. Batista,

- and G. W. Brudvig, “Nanotechnology for catalysis and solar energy conversion”, *Nanotechnology* **32**, 042003 (2021).
- ¹⁸²H. Fredriksson, Y. Alaverdyan, A. Dmitriev, C. Langhammer, D. S. Sutherland, M. Zäch, and B. Kasemo, “Hole–mask colloidal lithography”, *Advanced Materials* **19**, 4297–4302 (2007).
- ¹⁸³Z. Cui, *Nanofabrication: Principles, Capabilities and Limits: Second Edition* (2017), pp. 1–432, ISBN: 9783319393612.
- ¹⁸⁴S. Syrenova, C. Wadell, and C. Langhammer, “Shrinking-hole colloidal lithography: self-aligned nanofabrication of complex plasmonic nanoantennas”, *Nano letters* **14**, 2655–2663 (2014).
- ¹⁸⁵F. A. A. Nugroho, I. Darmadi, V. P. Zhdanov, and C. Langhammer, “Universal scaling and design rules of hydrogen-induced optical properties in Pd and Pd-alloy nanoparticles”, *ACS Nano* **12**, 9903–9912 (2018).
- ¹⁸⁶D. Albinsson, A. Boje, S. Nilsson, C. Tiburski, A. Hellman, H. Ström, and C. Langhammer, “Copper catalysis at operando conditions—bridging the gap between single nanoparticle probing and catalyst-bed-averaging”, *Nature Communications* **11**, 4832 (2020).
- ¹⁸⁷M. Pal, J. Garcia Serrano, P. Santiago, and U. Pal, “Size-controlled synthesis of spherical TiO₂ nanoparticles: morphology, crystallization, and phase transition”, *The Journal of Physical Chemistry C* **111**, 96–102 (2007).
- ¹⁸⁸Newport Corporation, *Liquid filters for light sources*, <https://www.newport.com/f/liquid-filters>, (accessed: 16.03.2022).
- ¹⁸⁹J. F. Moulder, W. F. Stickle, P. E. Sobol, and K. D. Bomben, *Handbook of X-ray photoelectron spectroscopy: a reference book of standard spectra for identification and interpretation of XPS data* (Physical Electronics, 1995), ISBN: 978-0964812413.
- ¹⁹⁰K. Siegbahn, *ESCA: atomic, molecular and solid state structure studies by means of electron spectroscopy* (Almqvist & Wiksell, 1967).
- ¹⁹¹S. Tanuma, C. J. Powell, and D. R. Penn, “Calculations of electron inelastic mean free paths (IMFPs). IV. evaluation of calculated IMFPs and of the predictive IMFP formula TPP-2 for electron energies between 50 and 2000 eV”, *Surface and Interface Analysis* **20**, 77–89 (1993).

- ¹⁹²G. Greczynski and L. Hultman, “X-ray photoelectron spectroscopy: towards reliable binding energy referencing”, *Progress in Materials Science* **107**, 100591 (2020).
- ¹⁹³A. F. Lee, C. M. Parlett, and K. Wislon, *Contemporary catalysis - science, technology, and applications* (Royal Society of Chemistry, 2017), ISBN: 978-1-84973-990-0.
- ¹⁹⁴S. Hofmann, *Auger-and X-ray photoelectron spectroscopy in materials science: a user-oriented guide*, Vol. 49 (Springer Science & Business Media, 2012), ISBN: 978-3-642-27381-0.
- ¹⁹⁵T. L. Barr and S. Seal, “Nature of the use of adventitious carbon as a binding energy standard”, *Journal of Vacuum Science & Technology A: Vacuum, Surfaces, and Films* **13**, 1239–1246 (1995).
- ¹⁹⁶S. Tougaard and C. Jansson, “Comparison of validity and consistency of methods for quantitative XPS peak analysis”, *Surface and interface analysis* **20**, 1013–1046 (1993).
- ¹⁹⁷Carl Zeiss Microscopy GmbH, *ZEISS GeminiSEM*, <https://www.zeiss.com/microscopy/int/products/scanning-electron-microscopes/geminisem.html>, (accessed: 16.03.2022).
- ¹⁹⁸K. Oura, V. Lifshits, A. Saranin, A. Zotov, and M. Katayama, *Surface science: an introduction* (Springer Science & Business Media, 2013), ISBN: 978-3-662-05179-5.
- ¹⁹⁹JEOL, *Periodic table for EDS analysis*, <https://www.jeolusa.com/RESOURCES/JEOL-Posters>, (accessed: 16.03.2022).
- ²⁰⁰J. I. Goldstein, D. E. Newbury, J. R. Michael, N. W. Ritchie, J. H. J. Scott, and D. C. Joy, *Scanning electron microscopy and X-ray microanalysis* (Springer New York, 2018), ISBN: 9781493966769.
- ²⁰¹A. W. Grant, Q.-H. Hu, and B. Kasemo, “Transmission electron microscopy windows for nanofabricated structures”, *Nanotechnology* **15**, 1175–1181 (2004).
- ²⁰²D. E. Newbury and N. W. M. Ritchie, “Performing elemental microanalysis with high accuracy and high precision by scanning electron microscopy/silicon drift detector energy-dispersive X-ray spectrometry (SEM/SDD-EDS)”, *Journal of Materials Science* **50**, 493–518 (2015).

- ²⁰³R. Chimentao, F Medina, J. Fierro, J Llorca, J. Sueiras, Y Cesteros, and P Salagre, “Propene epoxidation by nitrous oxide over Au–Cu/TiO₂ alloy catalysts”, *Journal of Molecular Catalysis A: Chemical* **274**, 159–168 (2007).
- ²⁰⁴C. Della Pina, E. Falletta, and M. Rossi, “Highly selective oxidation of benzyl alcohol to benzaldehyde catalyzed by bimetallic gold–copper catalyst”, *Journal of Catalysis* **260**, 384–386 (2008).
- ²⁰⁵B. N. Nunes, O. F. Lopes, A. O. T. Patrocínio, and D. W. Bahnemann, “Recent advances in niobium-based materials for photocatalytic solar fuel production”, *Catalysts* **10**, 126 (2020).
- ²⁰⁶L. D. Sio, T. Placido, R. Comparelli, M. L. Curri, M. Striccoli, N. Tabiryan, and T. J. Bunning, “Next-generation thermo-plasmonic technologies and plasmonic nanoparticles in optoelectronics”, *Progress in Quantum Electronics* **41**, 23–70 (2015).
- ²⁰⁷X. Huang, P. K. Jain, I. H. El-Sayed, and M. A. El-Sayed, “Plasmonic photothermal therapy (PPTT) using gold nanoparticles”, *Lasers in medical science* **23**, 217 (2008).

